THERMO-MECHANICAL BEHAVIOR OF SEVERELY DEFORMED TITANIUM

A Dissertation

by

Seyedvahid Sajjadifar

Submitted to the

Graduate School of Sciences and Engineering

In Partial Fulfillment of the Requirements for

the Degree of

Doctor of Philosophy

in the

Department of Mechanical Engineering

Özyeğin University

June 2017

Thermo-Mechanical Behavior of Severely Deformed Titanium

Approved by:

Assoc. Prof. Dr. Güney Güven Yapıcı
Advisor
Department of Mechanical Engineering
Özyegin University

Prof. Dr. Mehmet Arik
Department of Mechanical Engineering
Özyegin University

Assist. Prof. Dr. Zeynep Başaran Bundur
Department of Civil Engineering
Özyegin University

Assist. Prof. Dr. Alpay Oral
Department of Mechanical Engineering
Yıldız Technical University

Assist. Prof. Dr. Hakan Yılmazer
Metallurgical and Materials Engineering
Yıldız Technical University

ABSTRACT

Thermo-Mechanical Behavior of Severely Deformed Titanium

Thermo-mechanical processing of metallic materials has attracted noticeable interest due to the fact that these processing methods can be used to improve the mechanical properties. In this investigation, ultrafine grained commercial purity titanium was fabricated utilizing equal channel angular extrusion as a severe plastic deformation technique. Compression tests were performed on severely deformed titanium at various temperatures of 600–900^{o}C and at strain rates of 0.001–0.1s^{-1}. It was observed that severe plastic deformation via equal channel angular extrusion can considerably enhance the flow strength of grade 2 titanium deformed at 600 and 700^{o}C. Post-compression microstructures showed that a fine-grained structure can be retained at a deformation temperature of 600^{o}C. The strain rate sensitivity during hot compression of severely deformed Ti was shown to be strongly temperature dependent, where strain rate sensitivity increased with the increase in deformation temperature. High temperature workability of severely deformed grade 2 titanium was analyzed based on the flow localization parameter. According to the flow localization parameter values, deformation at and below 700^{o}C is prone to flow localization. The flow response of the ultrafine grained microstructure is modeled using the Arrhenius type, dislocation density based and modified Johnson-Cook models. The validities of the models were demonstrated with the reasonable agreement in comparison to the experimental stress-strain responses.

In order to investigate the influence of purity level on hot characteristics and dynamic softening mechanisms of severely deformed titanium, compression tests were

also conducted on severely deformed grade 4 titanium at similar temperatures and strain rates. It was seen that the effects of deformation rate and temperature are significant on obtained flow stress curves of both grades. Higher compressive strength exhibited by grade 2 titanium at relatively lower deformation temperatures was attributed to the grain boundary characteristics in relation with its lower processing temperature. However, severely deformed grade 4 titanium demonstrated higher compressive strength at relatively higher deformation temperatures (above 800^{o}C) due to suppressed grain growth via oxygen segregation limiting grain boundary motion. Constitutive equations were established to model the flow behavior, and the validity of the predictions was demonstrated with decent agreement accompanied by average error levels less than 5% for all the deformation conditions.

Severely deformed grade 4 titanium was less stable at the temperature range of 600-800^{o}C. Therefore, warm deformation behavior and microstructure evolution of severely deformed grade 4 titanium were studied at temperatures of 300-600^{o}C and at strain rates of 0.001-0.1s^{-1} in order to reveal the pertinent softening mechanisms such as dynamic recovery and dynamic recrystallization. Results suggest that severe plastic deformation is capable of increasing the strength of grade 4 up to 500^{o}C. Above this temperature the severely deformed microstructure was seen to demonstrate complete recovery. The strain rate sensitivity within the warm tension of severely deformed titanium was shown to be strongly temperature dependent, where strain rate sensitivity increased with the increase in deformation temperature. With the rise of temperature, void coalescence and growth of dimples takes place which was attributed to the higher rate of diffusion and growth of recrystallized grains at higher deformation temperatures.

Studying monotonic behavior of severely deformed titanium is not the only aim of this research work. Another important aspect is the fatigue behavior. Therefore, cyclic deformation response of coarse-grained and ultrafine-grained grade 4 titanium was probed by low cycle fatigue experiments at elevated temperatures up to 600^{o}C and at strain amplitudes of 0.2-0.6%. It was found that cyclic stability strongly depends on grain size and volume fraction of high angle grain boundaries. Severely deformed titanium showed an improvement in fatigue performance at or below 400^{o}C. Electron backscatter diffraction assisted microstructural findings were seen to stand in reasonable agreement with cyclic mechanical results, where micrographs revealed the occurrence of recrystallization and grain growth at 600^{o}C. Cyclic characteristics of two processing routes, defined as route-8E and 8B_c, were also compared. Accordingly, cyclic deformation response of severely deformed titanium was not sensitive to changing routes in the examined range of temperatures and strain amplitudes.

Last but not least, the impact of severe plastic deformation on the tensile and damping properties of titanium grade 4 was also explored to complete this study more effectively. Grain refinement via severe plastic deformation enhanced the strength at room temperature while this effect diminished at a high temperature of 600^{o}C. Ultrafine-grained titanium showed an improvement in damping capacity over its coarse-grained counterpart. High damping capacity of the former was rationalized with the contributions of increased dislocation density and high angle grain boundary fraction.

As a summary of this research, thermo-mechanical behavior of severely deformed titanium investigated in detail by demonstrating the thermal stability under monotonic and cyclic loading. It was found that severely deformed grade 2 and grade 4 titanium are

monotonically stable up to the homologous temperature of 0.45 and 0.40, respectively. Severely deformed grade 4 titanium also showed cyclic stability up to the homologous temperature of 0.35. These findings form the base for the utilization of ultrafine-grained titanium in high temperature applications.

ÖZET

Aşırı Deforme Titanyumun Termo-Mekanik Davranışı

Metalik malzemelerin termomekanik işlenmesi, malzemelerin mekanik özelliklerinin geliştirilebilmesi açısından önemli ve dikkat çekici bir alandır. Bu çalışmada, aşırı plastik deformasyon tekniği olarak eş kanallı açısal ekstrüzyon kullanılarak ultra-ince taneli ve ticari saflıkta titanyum üretilmiştir. Aşırı plastik deforme edilmiş ticari saflıktaki titanyum alaşımı üzerinde 600 - 900^{o}C sıcaklık aralığında ve 0,001 ile 0,1 s^{-1} gerinme hızları arasında basma testleri gerçekleştirilmiştir. EKAE yoluyla APD'nin 600 ve 700°C'de deforme olmuş 2. derece saflıkta titanyumun akma dayanımını belirgin şekilde artırabildiği gözlenmiştir. Basma sonrası oluşan mikroyapılar, 600°C'lik deformasyon sıcaklığında ince taneli bir yapının muhafaza edilebileceğini göstermiştir. Aşırı deforme olmuş titanyumun sıcak basma işlemi sırasında gerinme hızı duyarlılığı deformasyon sıcaklığı artışıyla birlikte yükselmekte olup, bu durum sıcaklık bağının önemli olduğunu göstermektedir. Aşırı deforme olmuş 2. derece saflıktaki titanyumun yüksek sıcaklıktaki işlenebilirliği akma lokalizasyon parametresine dayalı olarak analiz edilmiştir. Akma lokalizasyon parametre değerlerine göre 700°C ve altındaki sıcaklıklarda deformasyon lokalize olma eğilimindedir. Ultra-ince taneli mikroyapının akma tepkisi, Arrhenius tipi, dislokasyon yoğunluğuna dayanan ve modifiye edilmiş Johnson-Cook modelleri kullanılarak modellenmiştir. Modelleri geçerliliği, deneysel gerilme-gerinme tepkileri ile karşılaştırılıp gösterilmiştir.

Aşırı deformasyona uğramış titanyumun saflık derecesinin sıcak karakteristikleri ve dinamik yumuşama mekanizmaları üzerindeki etkisini incelemek için, aşırı plastik

deformasyon sonrası basma testleri 4. Derece saflıkta titanium üzerinde yapılmıştır. Sıcaklık ve deformasyon hızının her iki saflığın alma eğrisini önemli şekilde etkilediği görülmüştür. Nispeten daha düşük deformasyon sıcaklıklarında ikinci saflıkta titanyum numunelerin sahip olduğu yüksek basma dayanımı, düşük işlem sıcaklıklarına bağlı tane sınır özellikleri ile ilişkilendirilmiştir. Bununla birlikte, aşırı deforme olmuş dördüncü kalite titanyumun yüksek deformasyon sıcaklıklarında (800^{o}C'nin üzerinde) yüksek basma dayanımı göstermesi, oksijen ayrımı sebebiyle tane sınırı hareketini sınırlaması sonucu bastırılmış tane büyümesinden kaynaklanır. Akma davranışının modellenmesi için bünye denklemleri oluşturulmuştur. Ayrıca tahminlerin geçerliliği ortalama hata düzeyleri %5'in altında çıkmasıyla gösterilmiştir.

Aşırı deformasyona uğramış 4. Derece saflıkta titanyum numunelerin kararlılıkları 600-900^{o}C sıcaklık aralığında daha azdır. Bu nedenle, aşırı plastic deformasyon sonrası çekme gerilmesine maruz bırakılan 4. Kalite titanyumun ılık deformasyon davranışı ve mikroyapı gelişimi dinamik toparlanma ve dinamik yeniden kristalleştirmeyi gözlemlemek için 300-600^{o}C sıcaklıklarda ve 0.001-0.1 s^{-1} gerinme hızlarında çalışılmıştır. Sonuçlar aşırı plastic deformasyonun 500^{o}C sıcaklık değerine kadar titanyumun dayanımını arttırdığı yönündedir. Bu sıcaklık değerinin üzerinde aşırı deforme olmuş mikroyapının kapsamlı şekilde toparlandığı gözlenmiştir. Aşırı deforme olmuş titanyumun ılık gerilme sırasındaki gerinme hızı duyarlılığının, deformasyon sıcaklığındaki artışla birlikte arttığı görülerek sıcaklıkla güçlü bir ilişkisi olduğu belirlenmiştir. Sıcaklığın yükselmesiyle, yüksek deformasyon sıcaklıklarındaki daha yüksek difüzyon hızına ve yeniden kristalleşmiş tanelerin büyümesine dayandırılan boşluk birleşmesi ve çukurların büyümesi gerçekleşir.

Aşırı deforme olan titanyumun tek yönlü yükleme davranışı bu çalışmanın tek amacı değildir. Bu nedenle, iri ve ufak taneli 4. Saflıkta titanyumun çevrimsel deformasyon tepkisi 600^{o}C gibi yüksek sıcaklıklarda ve %0.2-0.6 gerinme genliğinde yapılan düşük çevrimli yorulma testleri ile incelenmiştir. Bu incelemenin sonucunda döngüsel kararlılığın tane boyutuna ve yüksek açılı tane sınırının hacimsel oranına bağlı olduğu bulunmuştur. Aşırı deforme titanyumun yorulma performansı, 400^{o}C ve altındaki sıcaklık değerlerinde ilerleme göstermiştir. 600^{o}C'de yeniden kristalleşme ve tane gelişiminin varlığının ortaya çıktığı elektron geri saçınımı kırınımı destekli mikroyapı bulguları döngüsel ve mekanik sonuçlarla uyum göstermektedir. 8E ve 8Bc olarak tanımlanan iki eş kanallı açısal ekstrüzyon rotasının döngüsel karakterleri karşılaştırılmıştır. Buna göre, aşırı deforme titanyumun tekrarlı deformasyona tepkisi sıcaklık ve gerinme genlik aralığı için ekstrüzyon rotalarına duyarlı değildir.

Son olarak, çalışmanın verimli bir şekilde tamamlanması adına aşırı plastik deformasyonun 4. Derece saflıkta titanyumun çekme ve sönümleme özellikleri üzerindeki etkisi incelenmiştir. Aşırı plastik deformasyon yoluyla tane inceltme işleminin oda sıcaklığında numunenin dayanımını arttırırken, 600^{o}C gibi yüksek sıcaklıklarda bu etkinin kaybolduğu görülmüştür. Ultra -ince taneli titanyumun sönümleme kapasitesinde iri taneli muadiline göre iyileşme görülmüştür. Yüksek sönümleme kapasitesi, artan dislokasyon yoğunluğunun ve büyük açılı tane sınırı oranının sönümleme katkısıyla açıklanabilir.

Bu araştırmanın en önemli bulgusu, monotonik ve döngüsel yük altında termal kararlılığının elde edilmesidir. Bu araştırmada özeti olarak, aşırı deforme titanyumun termo-mekanik davranışı tek yönlü çevrimsel yükleme altında ısıl kararlılığın gösterimi ile detaylı olarak incelenmiştir. Aşırı deformasyona uğramış 2. ve 4. Saflık derecesindeki

titanyumun tek yönlü yük altında sırasıyla 0.45 ve 0.40 benzeşik sıcaklığa kadar kararlı olduğu gözlenmiştir. Aşırı deformasyon sonrası 4. Saflık derecesinde titanyum aynı zamanda 0.35 benzeşik sıcaklığa kadar döngüsel kararlılık göstermiştir. Bu bulgular, ultra-ince taneli titanyumun yüksek sıcaklıktaki uygulamalarda kullanımı için temel oluşturmaktadır.

DEDICATION

This dissertation is dedicated to my parents.

ACKNOWLEDGEMENT

First and foremost, I want to appreciate my advisor, Dr. Guney Guven Yapici for his precious guidance and invaluable advice throughout my research project. Without his guidance and support, I would not be able to end up successful in this field of study.

I am very thankful to my PhD committee members, Dr. Mehmet Arik and Dr. Zeynep Başaran Bundur for their advice and attention to my study. I am deeply grateful to researchers and personnel of mechanical department of Ozyegin University. I would like to thank Mr. Ulaş Yıldırım for his help towards preparation of samples. I am thankful of my supportive office mates, Görkem M. Şimşek, Ali Vahid Yeganeh, Salar Salahi, Ali Hosseinzadeh, Onur Bilgin and Kambiz Shojaei. I also wish to thank my flatmates, Mahzad Azima and Ali Amiri for being great friends.

I would like to thank Dr. Hans Maier and Dr. Thomas Niendorf for being a wonderful collaborator and for their kind hospitality.

In addition to all the foregoing, I highly appreciate my beloved family. Especial thanks to my parents, Jaleh and Saeid who dedicated their lives to support me. My sisters, Vida and Shima are deeply thanked for their support and kindness. I am thankful of my sweet grandmother who taught me the most important lessons. Finally, I wish to thank my kind uncles, Dr. Riza Ommaty, Mr. Ali Ommaty, Mr. Ibrahim Ommaty and Mr. Mojtaba Ommaty for their continuous encouragement. A special thanks goes to Dr. Riza Ommaty who always helped me to overcome difficulties in the completion of my graduate studies.

I wish to acknowledge the support from the Marie Curie Career Integration Grant (Grant no. 304150) within the EU-FP7 programme for conducting this research study.

TABLE OF CONTENTS

LIST OF TABLES

LIST OF FIGURES

1. Motivation

For many years, researchers have made solid efforts in order to increase strength of materials by the use of various processing techniques. Among the processing methods, severe plastic deformation (SPD) was seen to enhance strength of metallic materials with minimum adverse effects on ductility. The SPD could bring a large number of scientific contributions beyond the state of the art in the materials strengthening investigations. Especially, this technique was found to be useful for commercial purity (CP) titanium since its strength was required to be improved [1–3]. A large number of industrial sectors are benefiting CP titanium and its alloys as they have properties such as remarkable specific strength and excellent biocompatibility. From the design perspective, strength and toughness of the materials can be named as the most important factors to be considered. A material or a structure should stand both applied monotonic and cyclic stresses and bear environmental destructive forces. Therefore, the number of applications which benefit CP titanium can be increased by improving strength of this material [2,4,5]. Due to its aforementioned importance, mechanical properties of severely deformed CP titanium at room temperature were frequently studied by researchers [1–3]. It is worth noting that by the application of SPD, the specific strength of CP titanium could also surpass some steel and beta titanium alloys. It was seen that a significant enhancement in the strength levels of two grades of CP titanium was achieved via equal-channel angular extrusion (ECAE) processing because of the grain refinement and the work hardening without alloying. Moreover, the biocompatibility of UFG titanium leads researchers to replace some alloys with toxic alloying elements, such as Al and V with it [6]. UFG titanium was implanted in rabbits and the removal torque was compared with that of CG CP titanium

Grade 2 and Ti6Al4V alloy Grade 5. It was found that the osseointegration of the UFG Ti was slightly superior of that of CP Ti Grade 2 [6]. The UFG titanium also shows a higher capacity of human osteoblast-like U2OS cells to colonize and, therefore, better osseointegration [7]

Improvement of fatigue strength was seen for UFG titanium in comparison with the conventional CG titanium. Therefore, investigations of hot deformation behavior along with elevated temperature fatigue tests of UFG titanium would remarkably make an impact in this field of study and smooth the research road to meet industrial requirements. A part from experimental achievements, scientists started to simulate ECAE process of CP titanium by the use of finite element method in order to study this field more effectively [8]. However, lack of discussions on elevated temperature behavior of severely deformed titanium motivated us to perform the present investigation.

Another missing point which inspired us to conduct the present study is hot deformation characteristics of severely deformed materials. The necessity of estimating required forces to be applied during warm and hot rolling or forging of metals has driven investigations on flow stress characterization and modeling under high temperature conditions. From metal forming perspective, due to lower yield strength of materials at high temperature regime, deformation needs lower processing forces to shape the work-piece. Findings of elevated temperature characteristics of UFG titanium can have a specific impact on this field of study. Study of mechanical behavior along with microstructural evolution at elevated temperatures can play a significant role in the adjustment of warm and hot working process parameters leading to improved workability. It is well-known that dynamic recovery (DRV) and dynamic recrystallization

(DRX) are powerful microstructural tools for controlling the structure and properties of metals under the deformation at elevated temperature [9,10]. When it comes to CP titanium, some studies concentrated on the hot deformation behavior of coarse grained (CG) structure titanium [11–14] while no one focuses on high temperature deformation of UFG titanium.

As well as mentioned motivations, lack of investigations on modeling and simulation of mechanical characteristics and flow stress curves of UFG titanium stimulated us to peruse this study since this methodology is applicable for predicting flow stress curves for deformation conditions outside the experimental window. Specifically, some typical modeling efforts were utilized to predict CG titanium behavior in the high temperature regime [15,16]. These approaches are mostly based on Arrhenius and Fields–Backofen equations. Therefore, modeling of commercial pure Ti after ECAE with UFG microstructure at elevated temperature would be a unique investigation. Various constitutive equations as in, Avrami, Arrhenius and Johnson-Cook can be applied to analytically model mechanical properties of severely deformed CP titanium at examined temperatures.

Moreover, the absence of cyclic characterizations of UFG titanium persuades us to carry out dynamic experiments. Especially, the stability of UFG structure should be studied at the high temperature fatigue regime. To the best knowledge of the authors, details of SPD processing influences on low cycle fatigue tests have not been comprehensively considered for severely deformed titanium at different temperatures. Therefore, these strong motivations which can extend the state of the art in this field led us to perform this research.

In addition to the investigation of monotonic and cyclic behavior of severely deformed CP Ti, damping capacity is a key property for materials used in light structures where undesirable vibrations exist. Due to the fact that the dislocation density and the existence of grain boundary sliding are important factors influencing the damping capacity, SPD could have a remarkable influence on the damping behavior. Up to now, a few studies considered the effect of grain refinement on damping properties of Mg and Al alloys [17,18]. However, the influence of grain refinement on damping properties of CP Ti has not been studied yet. Therefore, the current investigation aims to contribute insights on the damping characteristics of UFG Ti.

2. Background and Literature Review

2.1. Ultrafine-grained Materials Fabrication Methods

Various techniques such as rapid solidification (RS), mechanical alloying, severe plastic deformation (SPD), etc. have been introduced to manufacture UFG Ti [19]. Generally, these fabrication methods are being divided into 5 different groups as severe plastic deformation [20,21], electrodeposition [22,23], consolidation via severe plastic deformation [24,25], inert gas condensation of particulates and consolidation[26,27] and milling compaction [28–30].

Electrodeposition is a well-known method for fabricating decorative parts [22,23]. Electrodeposited metals contain high density of defects leading to increase in strength and strain rate hardening. However, ductility and elongation of parts manufactured via electrodepostion are noticeably low. Inert gas condensation and compaction was also utilized to produce nanocrystalline materials [26,27]. Existence of impurities such as hydrogen and oxygen in the parts synthesized via this method adversely affects their mechanical properties. Besides, ball milling was used to synthesize nanostructured materials in 1990s [28–30]. Lack of control on particle morphology and contamination of processed materials were main obstacles of this processing method.

Among all aforementioned manufacturing approaches, SPD was achieved to be the most promising one for obtaining UFG microstructure and improving strength of Ti [2,31]. One of the best ways for improving strength with moderate ductility is grain refinement via SPD. SPD is categorized among the top-down methods for processing of nanostructured materials. SPD causes grain refinement by fragmentation of initial grains [2,31]. Equal channel angular extrusion/pressing (ECAE/P), high-pressure torsion (HPT),

accumulative roll bonding (ARB), cyclic extrusion compression (CEC) and surface mechanical attrition treatment (SMAT) are outstanding SPD methods [32].

Among all aforementioned SPD methods, ECAE is perhaps, one of the most promising procedures for engineering applications due to its capability of maintaining the dimensions of the initial billet after multiple processing passes [1,12,33]. This method is able to provide industrial sectors with large enough samples and parts.

2.2. Fundamentals of Equal Channel Angular Extrusion

The main reason of mentioning principles of ECAE is that this processing method is one of the thermo-mechanical methods which are applied in the present research work. There are some researches concentrating on principles of ECAE processing method [34–38]. The schematic of ECAE processing is demonstrated in Fig. 2.1. the X, Y and Z planes stand for the transverse plane, the flow plane and the longitudinal plane, respectively [39]. The billet is pressed through the channels utilizing a plunger [39]. Then, the sample is being deformed by simple shear.

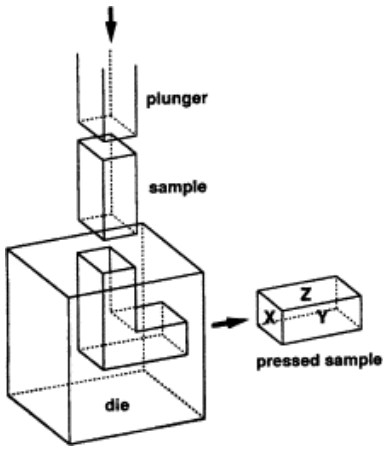

Figure 2.1 Schematic of ECAE process, the X, Y and Z planes stand for the transverse plane, the flow plane and the longitudinal plane, respectively [39].

The angle between two channels, the punch pressure and the yield stress usually denote by 2Φ, P and σ_0, respectively. Strain can be obtained as follows [38,40]:

$$\frac{P}{\sigma_0} = \frac{2}{\sqrt{3}}\cot \emptyset = \varepsilon \quad (1)$$

Since the intersection angle is 90°, a true plastic strain of 1.16 can be achieved. Besides, the equivalent percent area reduction (AR) can be obtained following the methodology outlined in [38,40]:

$$AR = (1 - RR^{-1}) \times 100\% \quad (2)$$

Where, RR is the reduction ratio. Therefore, the equivalent area reduction of 69% can be obtained. Total strain for N passes can be simply calculated as:

$$\varepsilon_t = N \times \varepsilon \quad (3)$$

Various routes have been used to study effect of altering the billet orientation at each pass [1]. Figure 2.2 represents the common routes of ECAE process.

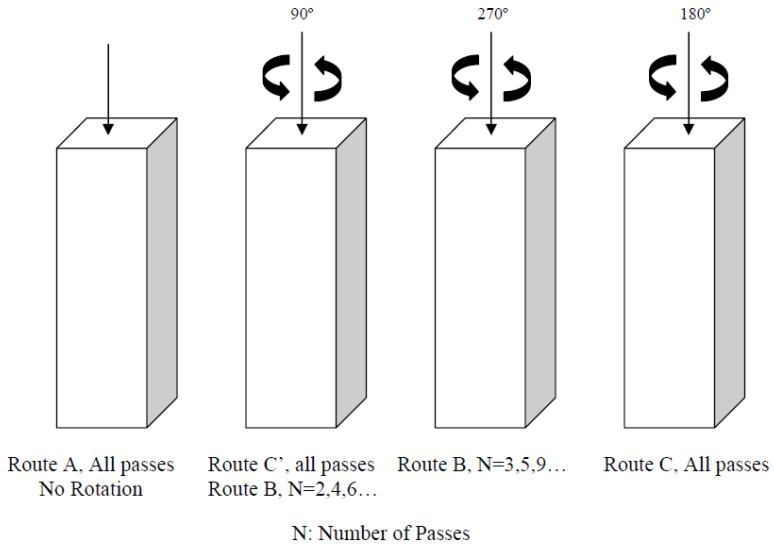

Figure 2.2 Schematic of ECAE routes [40]

It follows from the Fig. 2.2 that there is no rotation for route A. In route B, the billet is rotated +90° after each odd pass and - 90° after each even pass. In route C, the billet is spun 180° around its axis after every pass. Route E consists of an alternating rotation of the billet by +180° and +90° around its long axis, between successive passes.

In route B_C, the billet is rotated $+90^o$ around its long axis, between each successive pass [40].

2.3. Principles of Rolling Process

Rolling process is being used as one of the SPD processes in order to enhance strength of examined materials. Therefore, some fundamentals of this process are described in this section. Roll forming is one of the oldest processes of sheet manufacturing methods. The first rolling process for iron sheet occurred in 1670s [41]. Then, Christopher Polhem made some effort to deform iron bars via rolling mills [42]. Currently, rolling process is being utilized by industrial sectors to manufacture sheet metals more effectively. In conventional rolling process, slab or sheet metals are squeezed between two rolls while rotating in opposite directions [43]. Rolling mill stand is represented in Fig 2.3.

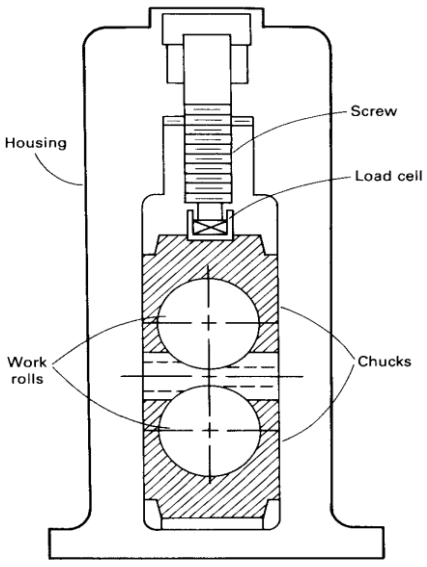

Figure 2.3 Conventional rolling mill stand [43]

Fig. 2.4 shows the schematics of flat rolling process. Therefore, the roll force, true strain and power in flat rolling process can be calculated as seen below [44]:

$$F = LwY_{avg} \quad (4)$$

$$L = \sqrt{R(h_0 - h_f)} \quad (5)$$

$$\varepsilon_t = ln\frac{h_f}{h_0} \quad (6)$$

$$Power = \frac{2\pi FLN}{60000} \quad (7)$$

Where L, w, Y_{avg} and R are roll-strip contact length, width of the strip, average true stress of the strip and roll radius. h_0 and h_f are initial and final thickness of work-piece, respectively.

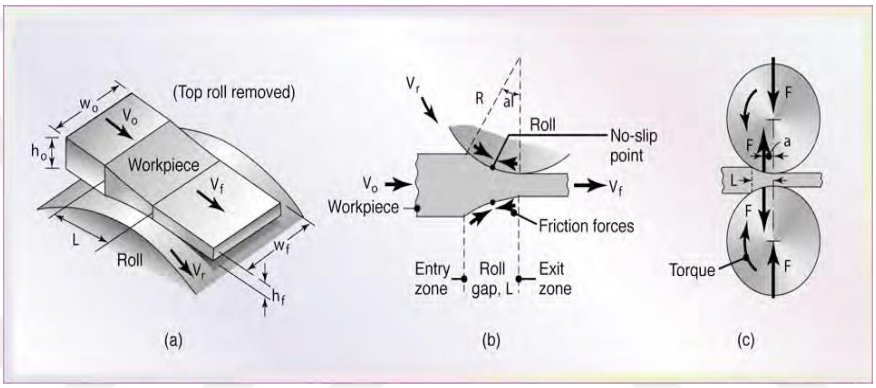

Figure 2.4 Schematics of flat rolling process [44]

2.4. Precipitation Hardening

Formation of precipitates can increase strength of materials due to the fact that they interact with dislocations and suppress their motions [45]. Artificial precipitation hardening generally consists of solubilization, quenching and aging treatments. In solubilization, alloy is heated up to monophase region and it is kept for a long time to dissolve pre-existent precipitates. Then, it will be quenched to avoid formation of precipitates during cooling. The quenching treatment results in a supersaturated solid. Lastly, the supersaturated solid will be held at a gradually high temperature (below monophase region) to introduce fine precipitates [45]. According to the size of precipitates, two types of dislocation-precipitate interaction have been explained. When

precipitates are finer than a critical size, dislocations are able to cut through them. However, dislocations circumnavigate around precipitates when their size is bigger than the critical one [46]. These theories are described in the Fig. 2.5.

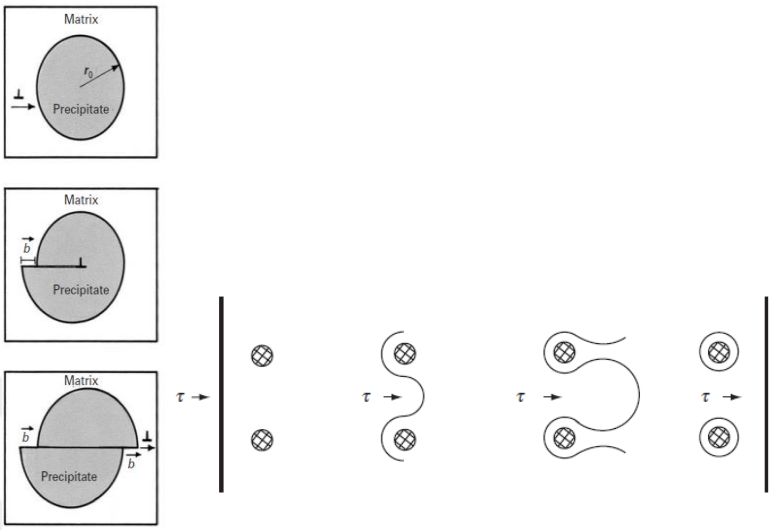

(a)

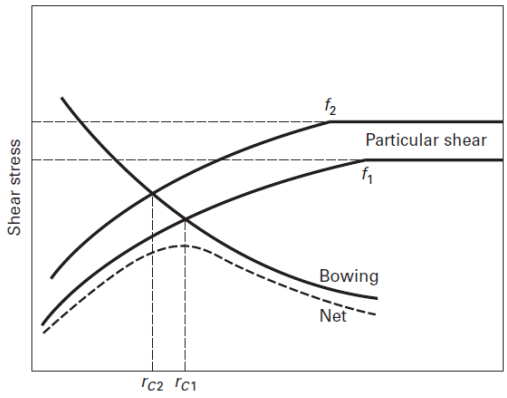

(b)

Figure 2.5 (a) dislocation shearing and bowing mechanisms (b) dislocations cutting and bowing mechanisms where f is volume fraction of precipitates (f2>f1) [45]

Rise in yield stress can be obtained following outlined [45,46]:

For deforming particles:

$$\Delta\tau = CG\varepsilon^{2/3}\sqrt{\frac{fr}{b}} \quad (8)$$

For non-deforming particles:

$$\Delta\tau = \frac{Gb}{(L-2r)} \quad (9)$$

2.5. Commercial Purity Titanium and Titanium Alloys

2.5.1. Crystallography of Titanium

At ambient temperature, pure Ti crystal structure is hexagonal close packed (hcp), known as alpha Ti. At elevated temperature, crystal structure of Ti changes into a body-centered cubic (bcc) form [47]. Schematics of atomic unit cells of alpha and beta Ti are displayed in Fig. 2.6. Ti properties such as ductility and diffusion rate are different in various crystal structures. It is also well-documented that Ti with hcp crystal structure shows anisotropy of mechanical properties [47].

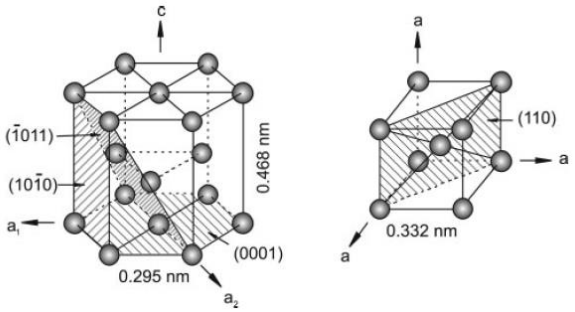

Figure 2.6 Crystal structure of Ti allotropes [47]

The beta transus temperature of CP Ti was observed to be about 882±2^{o}C [47]. Properties of Ti remarkably change above the corresponding allotropic transformation temperature due to the fact that crystal structure of Ti varies at elevated temperature. Generally, beta Ti is more ductile than that of alpha allotrope.

2.5.2. Characteristics of Coarse Grained Titanium Alloys

As mentioned earlier, CP Ti and its alloys are being increasingly utilized in various industries such as aerospace, transportation and marine applications. This is because of their especial characteristics and properties. In this section, some of these significant properties have been stated.

Alloying elements of Ti can be categorized as alpha stabilizers, beta stabilizers or neutral. Neutral alloying elements hardly affect beta transus temperature while beta stabilizing elements are able to decrease beta transus temperature considerably. On the other hand, alpha stabilizers can widen alpha phase field to higher temperature [47]. The influence of alloying elements on the phase transformation diagrams of Ti alloys is displayed in Fig. 2.7.

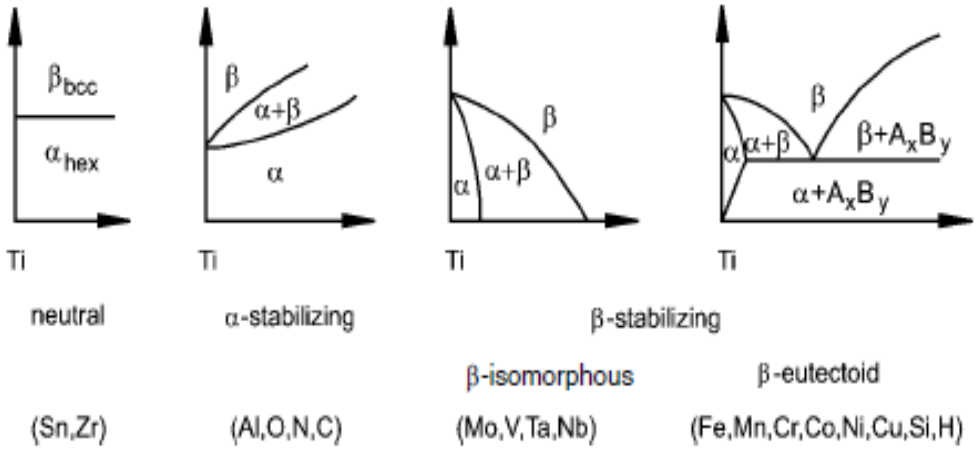

Figure 2.7 Effect of different alloying elements on phase transformation diagrams of Ti alloys [47]

One of the most significant titanium phase diagrams is the system Ti-Al as shown in Fig. 2.8. Several intermetallic phases such as α_2-Ti_3Al, ϒ-TiAl, $TiAl_2$ and $TiAl_3$ can be seen in Ti-Al phase diagram. Nowadays, α_2-Ti_3Al and ϒ-TiAl intermetallic components are

widely being used in elevated temperature applications since they are more stable at higher temperatures [47].

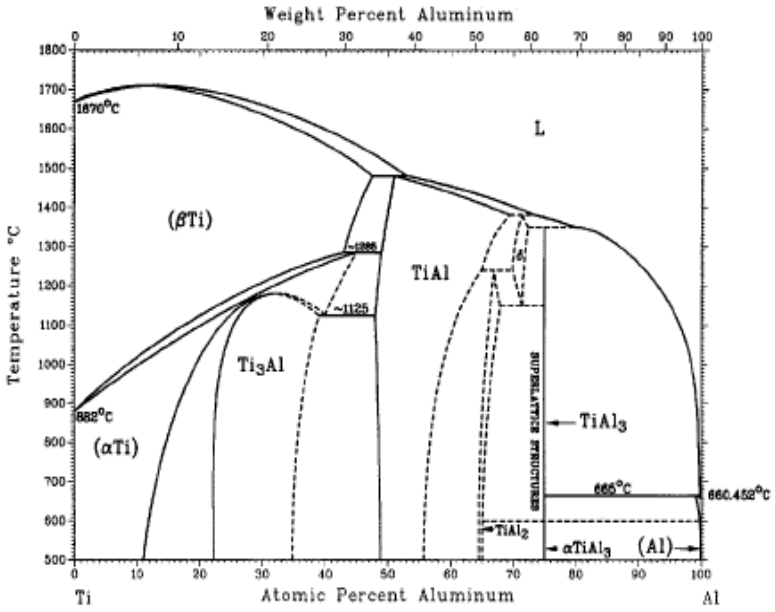

Figure 2.8 Ti-Al phase diagram [47]

One of the beta phase stabilizer for Ti alloys is vanadium element. This element is capable of reducing beta transformation temperature under equilibrium condition [47]. Fig. 2.9 demonstrates Ti-6Al-V ternary phase diagram and the corresponding microstructures at 650-1050^{o}C. Obviously, beta phase volume fraction drops with reduction in temperature. It is also worth noting that beta transformation into martensite enhances at higher cooling rates.

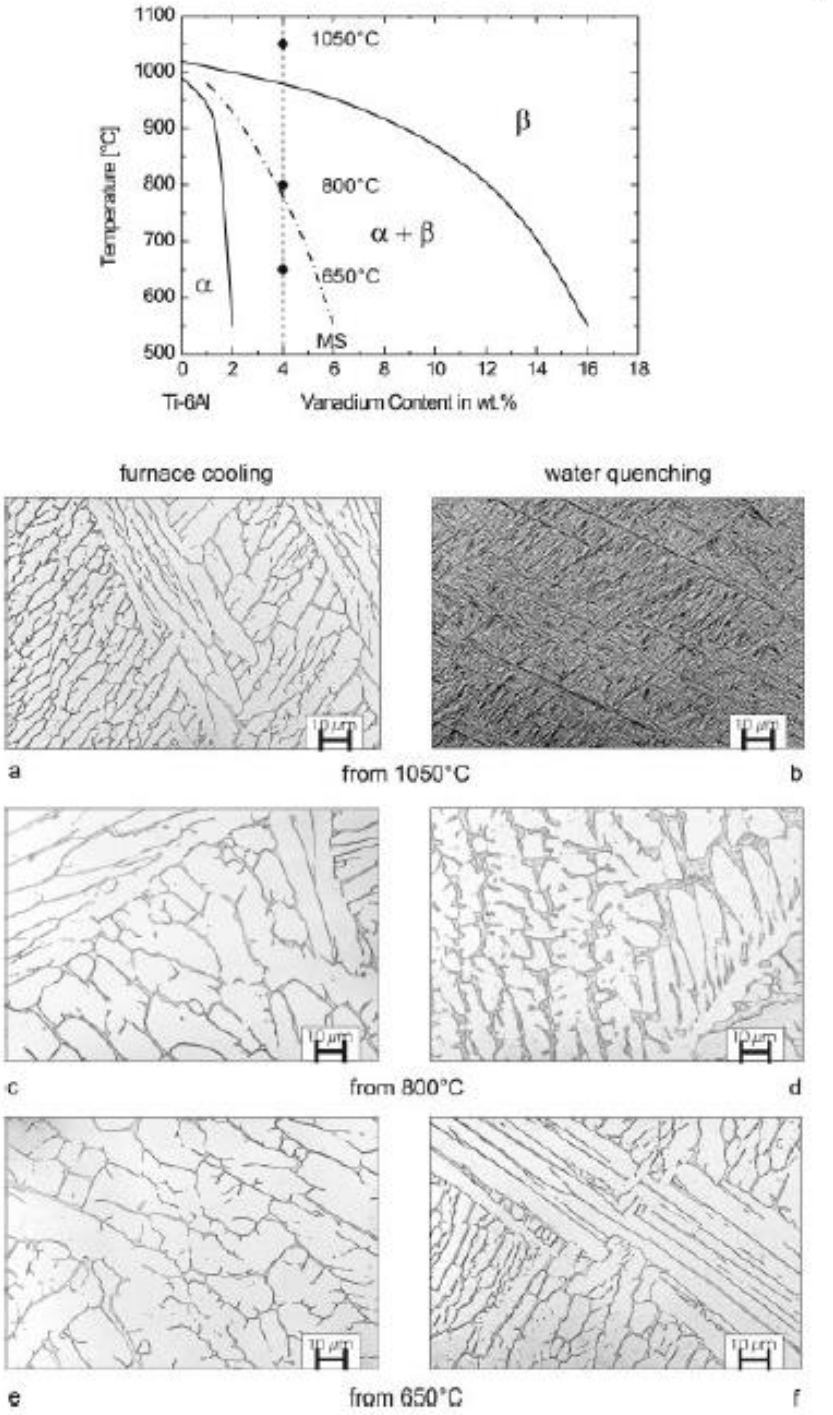

Figure 2.9 Ti-6Al-4V ternary phase diagram and corresponding microstructures at various conditions [47]

High specific strength of Ti motivated researchers to study this material more effectively. CP Ti density is about 4.51 g/cm^3. Ti is lighter than many industrial metals as in Fe, Cu and Ni although it is classified as the heaviest light metal [47]. As shown in Fig. 2.10, strength of Ti alloys can compete with steel alloys [47,48]. Due to their superior strength to weight ratio, they are remarkably preferential in the aerospace applications.

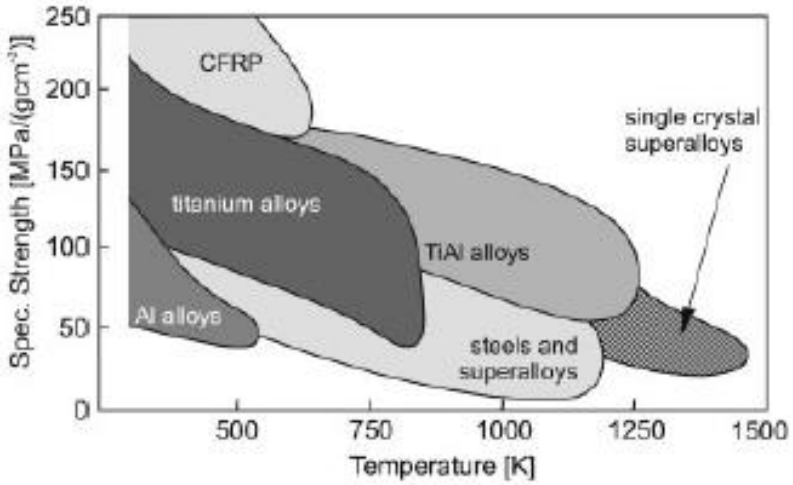

Figure 2.10 Specific Strength versus temperature for structural materials [47]

Another important property of Ti and its alloys is their resistance to corrosion. Outstanding corrosion resistance of Ti makes it a great candidate where biocompatibility is needed. It could be attributed to the formation of a protective oxide film [49]. However, oxidation kinetics of Ti alloys is being considerably affected by temperature and atmosphere. At high temperature, corrosion resistance of Ti alloys is degraded [47]. Fig. 2.11 shows the oxidation kinetics of Ti-45Al-8Nb at different temperatures and atmospheres [50]. It can be seen that corrosion resistance of this alloy decreased with rise in temperature.

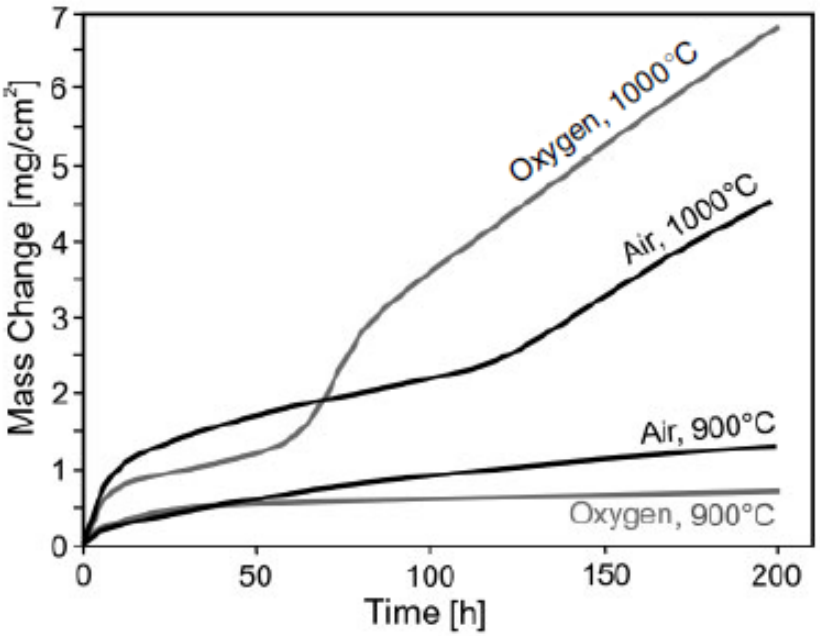

Figure 2.11 Oxidation behavior of Ti-45Al-8Nb at different temperatures and atmospheres [50]

Exceptional biocompatibility of CP Ti and its alloys resulted in usage of them in osseointegration of dental implants as shown in the Fig. 2.12. Ti was found to have the minimum toxic effects among other metallic materials [51]. This biocompatibility is because of high corrosion resistance of Ti in the human body.

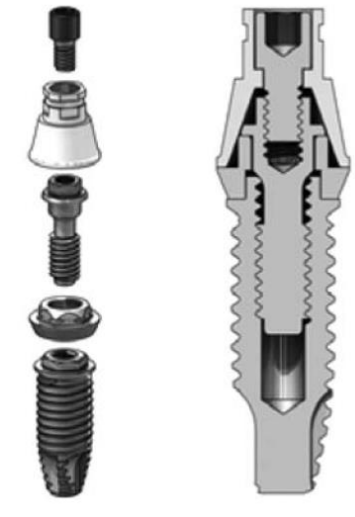

Figure 2.12 A dental implant made of Ti [51]

One of the important mechanical properties of an industrial material is its fatigue resistance. There are some studies which focus on the cyclic behavior of coarse grained Ti and Ti alloys [52–56]. The effects of hold time and stress on fatigue strength and fatigue life of CP Ti have been studied [53]. It was found that with rise in hold time dwell fatigue strain alters from ratcheting strain controlled to creep strain controlled. In another study, cyclic deformation response of Ti-6Al-4V alloy is investigated [56]. Low cycle fatigue of this alloy was precisely predicted by a critical strain approach. As it can be seen in the Fig. 2.13, cyclic behavior of Ti-6Al-4V alloy is dependent on orientation of basal plane. Besides, effect of heat treatment and cooling rate of Ti-35Nb on corrosion fatigue behavior was considered [55]. High cooling rates caused higher fatigue resistance which was imputed to formation of martensitic beta phase. The influence of Boron additions on the elevated-temperature fatigue behavior of Ti-6Al-4V alloy was also studied [54]. Boron addition led to the higher fatigue resistance which was due to the refinement of the as-cast grain size.

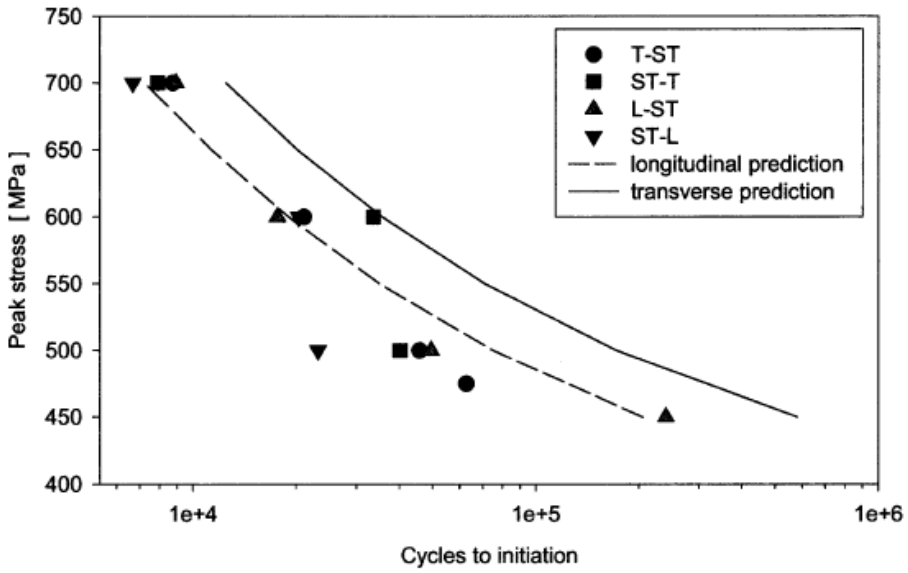

Figure 2.13 Experimental and predicted S-N curves of Ti-6Al-4V alloy with respect to orientation [56]

2.6. Grain Boundary Strengthening and Hall-Petch Relation

One of the strengthening methods is grain refinement. Grain boundaries are strong obstacles against dislocation motion [57]. Generally, different grains have various crystallography orientations that change from a grain to the next one. With increase in orientation difference between the grains, order in the boundaries reduced and then grain boundary angle rose. It is well-documented that high-angle grain boundaries are strong barriers to dislocation motion [57]. Basically, Hall-Petch relation is used to calculate effect of grain refinement on strength of metallic materials [58,59]. The relationship proposed by Hall and Petch can be seen as follows:

$$\sigma_0 = \sigma_i + kD^{-1/2} \quad (10)$$

Where, σ_0 and σ_i are the friction stress and the yield stress, respectively. K is the locking parameter and D is the grain diameter. According to Hall-Petch equation, reduction in grain size results in higher yield stress.

2.7. Monotonic Behavior of UFG Materials at Ambient Temperature

At ambient temperature, monotonic behavior of severely deformed materials were studied comprehensively [1–3,60–65]. It was found that SPD is capable of enhancing yield stress, tensile strength and microhardness of titanium [1–3,64,65]. Fig. 2.14 shows flow stress curves of as-received, ECAE processed and ECAE processed plus rolled CP grade 2 Ti at room temperature [3]. SPD resulted in two-fold increase in tensile strength of titanium. It is also worth noting that post rolling process led to improvement of UFG Ti ductility.

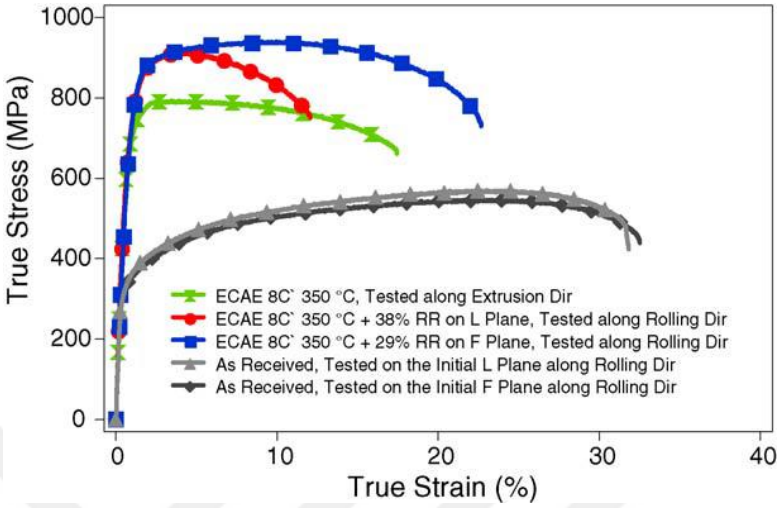

Figure 2.14 Flow stress curves of the as-received, ECAE processed and ECAE processed plus rolled CP grade 2 Ti at room temperature [3]

It was stated that grain boundaries inhibit dislocation motions through the microstructure causing strength enhancement of CP Ti [66]. TEM micrograph of CP Ti after 4 passes of ECAE is shown in Fig. 2.15. Formation of elongated and fine equiaxed grains is evident.

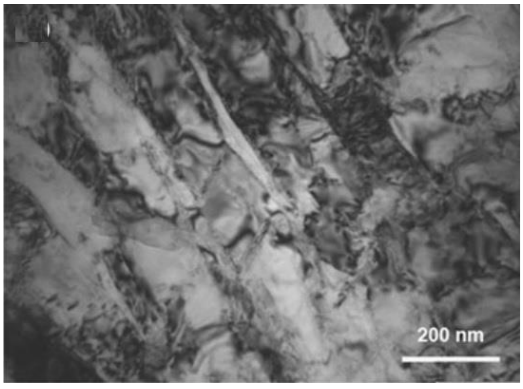

Figure 2.15 TEM micrograph of CP Ti after 4 passes of ECAE [67]

2.8. Cyclic Behavior of UFG Materials at Ambient Temperature

Cyclic response of UFG materials at ambient temperature was the topic of several research works [68–78]. Among the works mentioned, cyclic response of UFG Ti was also investigated [73–77]. This UFG material showed an extraordinary fatigue behavior and resistance. It was observed that ultrafine grained microstructures are highly susceptible to the localized grain growth by cyclic plastic deformation [73,79]. Therefore, cyclic behavior of UFG structures under low cycle fatigue (LCF) in which plastic deformation occurred in each cycle needs to be fully investigated. Fig. 2.16a displays cyclic deformation responses of CG and UFG Ti at ambient temperature. UFG Ti specimens showed a stable cyclic deformation response, higher stress ranges and longer fatigue lives. This was imputed to the resistance of high angle grain boundaries to rearrangement when dislocations interact with them under cyclic deformations [73]. On the other hand, Ti samples with bimodal microstructure could not surpass fatigue performance of UFG T (Fig. 2.16b). Due to localized grain growth by cyclic plastic deformation occurrence in the heat treated samples, bimodal structure showed an inferior fatigue performance [73].

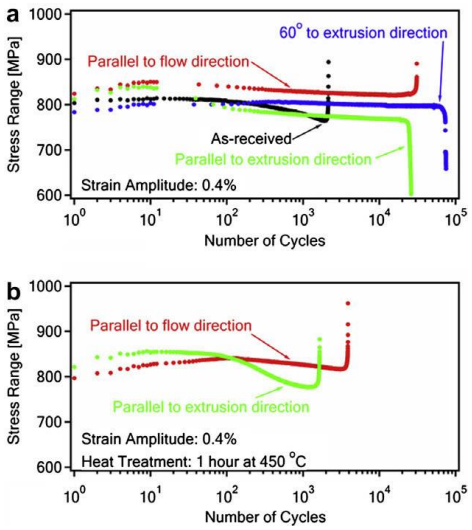

Figure 2.16 Fatigue response of (a) CG and UFG titanium (b) titanium with a bimodal microstructure [73]

Another reason for inferior fatigue performance of titanium with bimodal microstructure was seen to be locally damage accumulation. Smaller grains acted as a stress riser causing stress concentration and then damage accumulation [73]. EBSD map of the bimodal titanium can be seen in the Fig. 2.17.

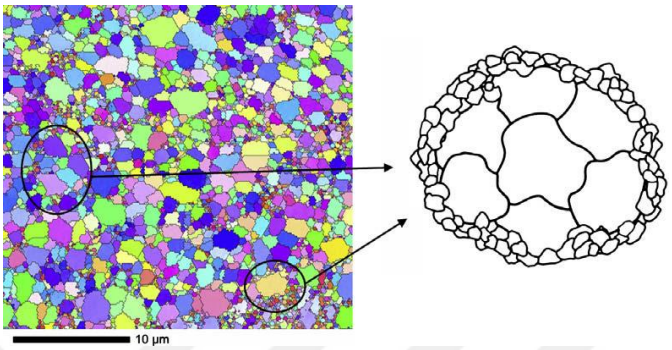

Figure 2.17 EBSD map of Ti with bimodal microstructure [73]

The influence of notches on fatigue strength and fatigue life time of UFG Ti was also studied elsewhere [74]. Fig. 2.18 demonstrates stress amplitude versus number of cycles to failure for both CG and UFG Ti. It can be seen that the fatigue performance of titanium is considerably enhanced after SPD processing. The fatigue performance improvement of notched UFG Ti samples was related to the significant enhancement of strength [74].

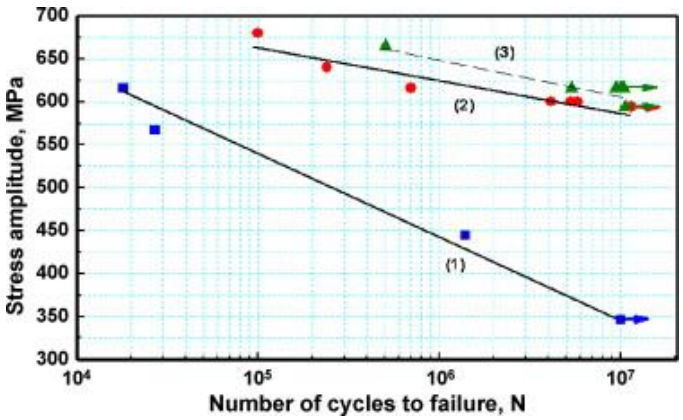

Figure 2.18 Stress amplitude versus number of cycles for smooth samples of coarse-grained Ti (curve 1), UFG Ti after ECAE and thermal and mechanical treatment (TMT) (curve 2), after ECAP + TMT and additional annealing at 350°C, 6 h (curve 3) [74]

At ambient temperature, higher stress amplitude values were also reported for UFG Cu (Fig. 2.19) [78]. During cyclic loading, the microstructure of this UFG material remained unchanged verifying cyclic stability at examined strain amplitudes.

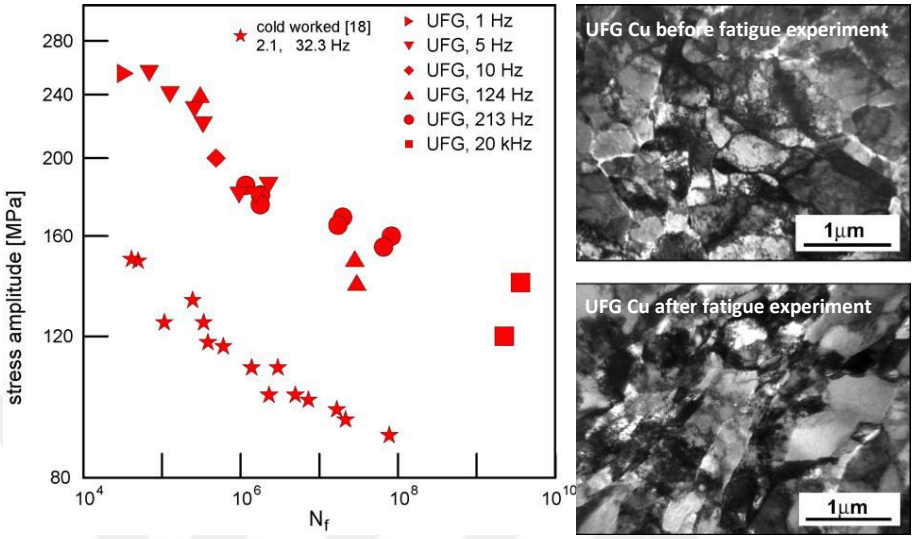

(a) (b)

Figure 2.19 (a) S–N data for ultrafine-grained Cu and cold worked Cu (b) microstructure of UFG Cu before and after fatigue experiment [78]

2.9. Softening Mechanisms at Elevated Temperature Deformation

In this section, softening mechanisms which are active during warm and hot deformation of materials are discussed. This section is written since elevated temperature deformation of CP Ti has been investigated and thermo-mechanical parameters have been studied comprehensively.

2.9.1. Dynamic Recovery

Researchers started working on hot deformation characteristics of different alloys and materials in 1960s [80–85]. In 1970s, it has been realized that two various softening mechanisms are existent in hot deformation of metallic materials [86–89]. Materials whose dislocations are able to cross-slip and climb can easily rearrange into polygonal

subgrain structures and tend to display a high degree of dynamic recovery (DRV), while materials with low stacking fault energy (SFE) show a much lower level of dynamic recovery [90]. The schematic flow curve of materials during DRV is shown in the Fig. 2.20 [91]. The work hardening (WH) rate overcomes the softening rate induced by DRV in the beginning, and thus the stress considerably increases during initial deformation then increases at a decreased rate, followed by next stage.

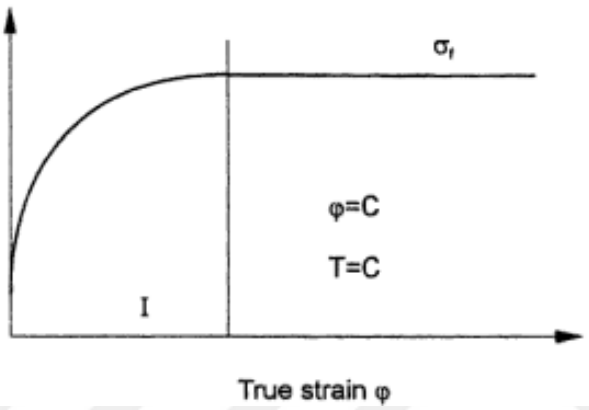

Figure 2.20 Schematic flow curve by DRV [91]

2.9.2. Dynamic Recrystallization

In materials with low SFE, dynamic recrystallization (DRX) took place due to inadequate DRV and climb of dislocations [90]. Dislocation density rises until it reaches a critical condition, at which point new grains nucleate and grow during further straining. The schematic flow curve of materials during DRX is displayed in the Fig. 2.21 [91]. After initial work hardening, flow curve demonstrates an abrupt reduction in yield stress and then reaches a plateau.

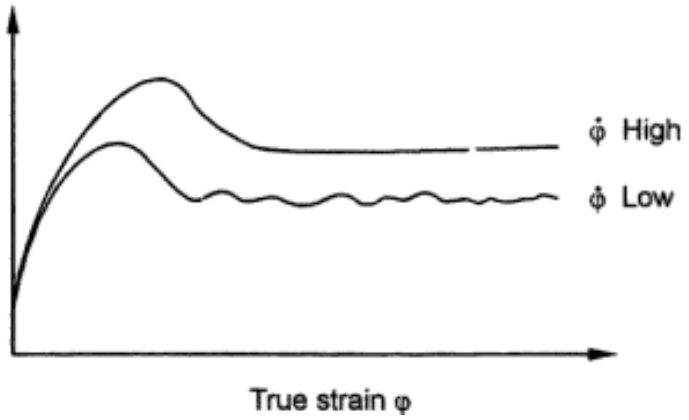

Figure 2.21 Schematic flow curve by DRX [91]

Two main types of DRX which have been defined previously are discontinuous dynamic recrystallization (DDRX) and continuous dynamic recrystallization (CDRX) [92,93]. In CDRX, The mechanism is composed of the formation of subgrains with low-angle boundaries in grain interiors. The boundary misorientation rises slightly during deformation leading to new grain formation at high strain levels [94,95]. DDRX is related to recrystallization of new grains at existing grain boundaries which basically consists of the grain boundary bulging and strain-induced grain boundary migration (SIBM) [96]. These mechanisms are specifically explained in the following chapters.

2.10. Monotonic Behavior of Coarse-Grained Titanium and its Alloys at Elevated Temperature

Due to the importance of high temperature behavior of materials, several researches have focused on the warm and hot characterization of coarse grained CP Ti [11,15,16,97]. Zeng et al. studied behavior of CP Ti up to the deformation temperature of 700^{o}C and at various strain rates [11]. Stress-strain curves obtained in the aforementioned research work are shown in the Fig. 2.22. The dependency of flow stress

to the temperature and the rate of deformation is obvious. Basically, deforming CP Ti at higher temperature or lower rate led to drop in flow stress level.

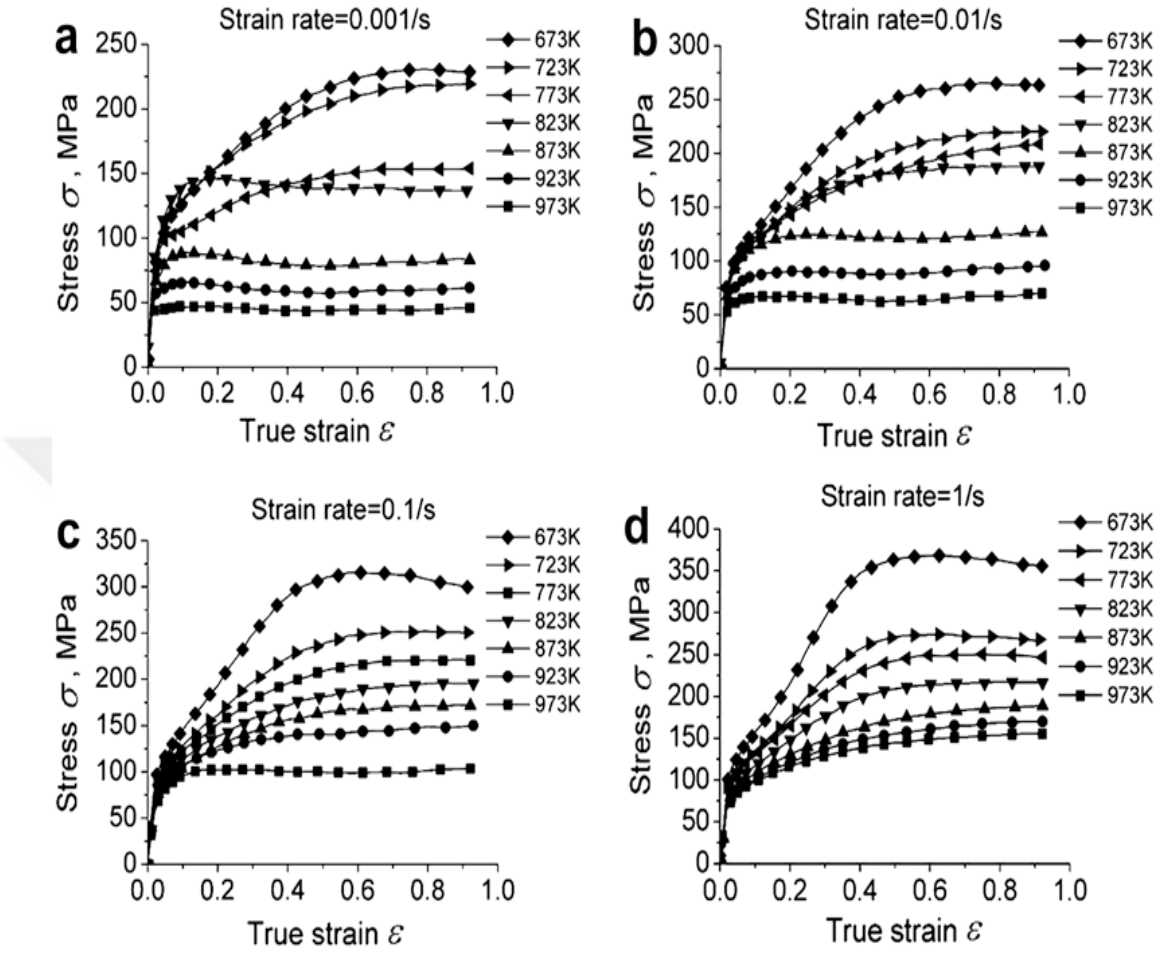

Figure 2.22 Stress-strain curves of coarse-grained CP Ti at different deformation conditions [11]

Work hardening rate of CG titanium was also investigated as depicted in Fig. 2.23. Curves were shown in three groups; (a) three-stage work hardening (b) two-stage work hardening and (c) flow softening [11]. It was seen that higher deformation temperature and lower strain rate resulted in flow softening which could be attributed to the activation of softening mechanisms at elevated temperatures.

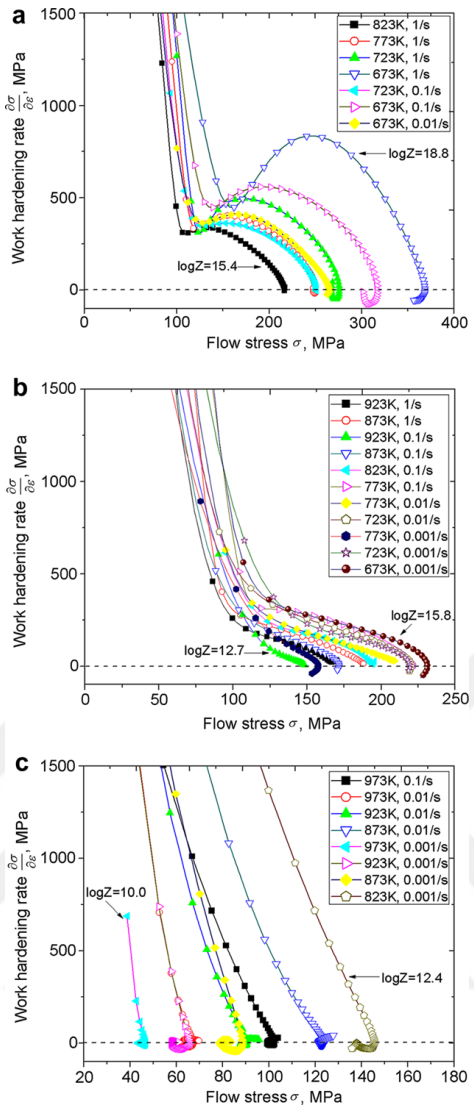

Figure 2.23 Work hardening rate of CG titanium versus flow stress (a) three-stage work hardening (b) two-stage work hardening and (c) flow softening [11]

Figure 2.24 demonstrates optical microstructure and EBSD map of the sample deformed at 700°C with strain rate of $0.01s^{-1}$ [11]. These micrographs also confirm that serration of grain boundaries and DRX occurred at this deformation condition.

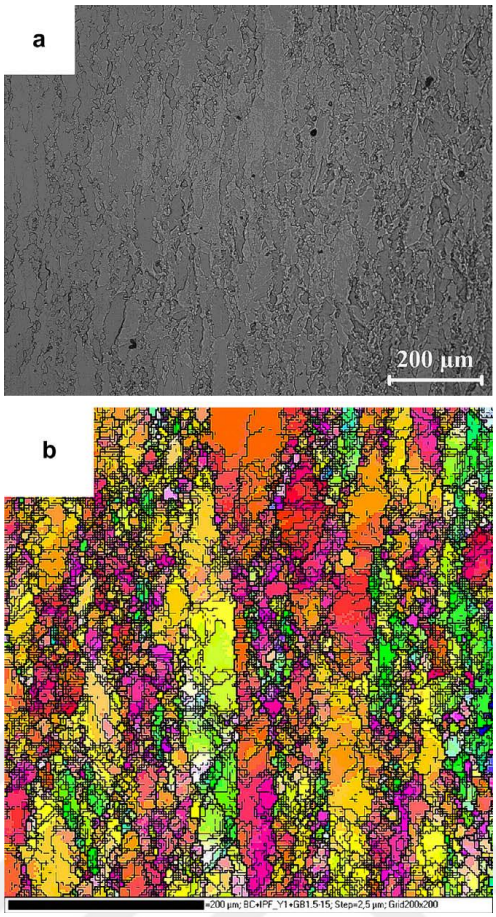

Figure 2.24 Microstructure of CG titanium deformed at 700^{o}C with strain rate of 0.01s^{-1} (a) optical microstructure (b) EBSD map [11]

As mentioned before, modeling response of coarse grain titanium at elevated temperature was also studied. Arrhenius-type equation was utilized in order to predict flow stress behavior of this material [15]. Modeling methodology is comprehensively explained in the chapter 5. Fig. 2.25 shows both predicted results and experimental data. Modeling results are in agreement with the experimental data. Therefore, modeling of stress-strain curves based on Arrhenius-type equation was observed to be satisfactory. The error values were also less than 8.5% for all samples except the specimen deformed 700^{o}C with strain rate of 0.001s^{-1}.

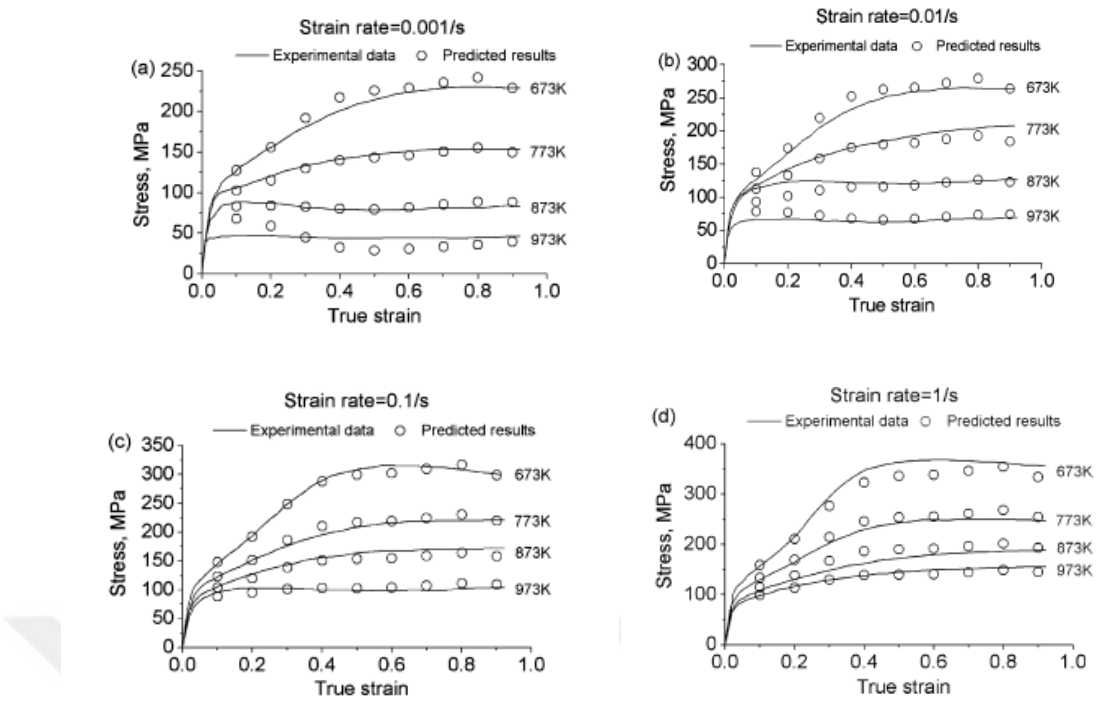

Figure 2.25 Predicted and experimental stress-strain curves of CG titanium for samples deformed at (a) 0.001s^{-1} (b) 0.01s^{-1} (c) 0.1s^{-1} and (d) 1s^{-1} [15]

Fields–Backofen equation was also used to model high temperature behavior of CG Ti at temperatures ranging from 350^{o}C to 500^{o}C and strain rates from 0.00083s^{-1} to 0.05s^{-1} [16]. Fields–Backofen equation can be seen as follows [16]:

$$\sigma = K \times \varepsilon^{n} \times \dot{\varepsilon}^{m} \quad (11)$$

Where σ is the flow stress, ε is the strain, $\dot{\varepsilon}$ is the strain rate, K is the strength coefficient, n is the work hardening exponent and m is the strain rate sensitivity exponent. Taking the logarithm of eqns. (11), gives:

$$log\sigma = logK + nlog\varepsilon + mlog\dot{\varepsilon} \quad (12)$$

Different parameters can be obtained from the slope and intercept of the lines plotted according to Eqn. (12). Therefore, flow stress can be predicted for each strain value. Fig. 2.26 demonstrates a comparison between predicted and experiments values. It

was stated that modeling of elevated temperature behavior of CG titanium is fairly satisfactory [16].

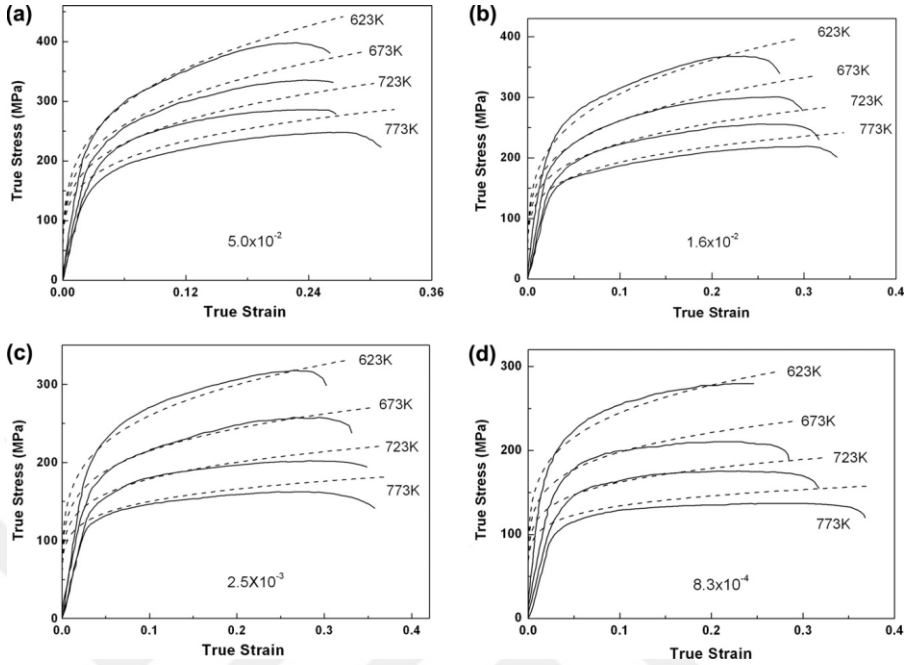

Figure 2.26 Comparisons between predicted and experiment values at (a) $0.05s^{-1}$ (b) $0.016s^{-1}$ (c) $0.0025s^{-1}$ and (d) $0.00083s^{-1}$[16]

As well as coarse-grained CP Ti, high temperature behavior of Ti alloys was also probed in the past years [98,99]. Ko et al. investigated high temperature behavior of UFG Ti-6Al-4V alloy at temperatures of 600^{o}C to 700^{o}C and different strain rates [98]. Superplasticity of UFG Ti-6Al-4V alloy was seen for the samples deformed at 600^{o}C to 700^{o}C (Fig. 2.27). However, deforming severely deformed Ti-6Al-4V alloy at higher temperature led to decrease of its strength.

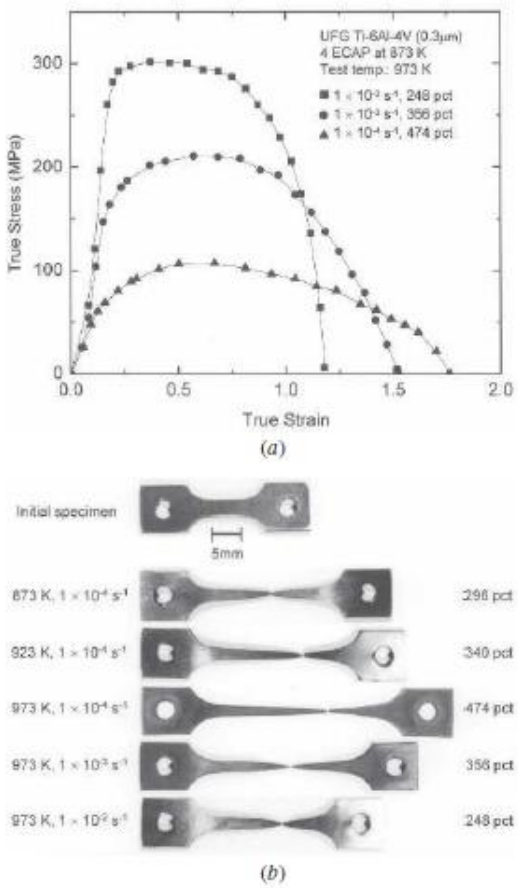

Figure 2.27 (a) True stress-strain curves of UFG Ti-6Al-4V (b) specimens tested at various conditions [98]

In a separate study, hot deformation characteristics of a coarse-grained Ti-15V-3Cr-3Sn-3Al (Ti-15-3) alloy was studied [99]. Microstructure investigations revealed that DRX took place at high deformation temperature as shown in Fig. 2.28. For the samples deformed at 850^{o}C with strain rate of 0.001s^{-1}, formation of newly recrystallized grains happened when the amount of strain increased.

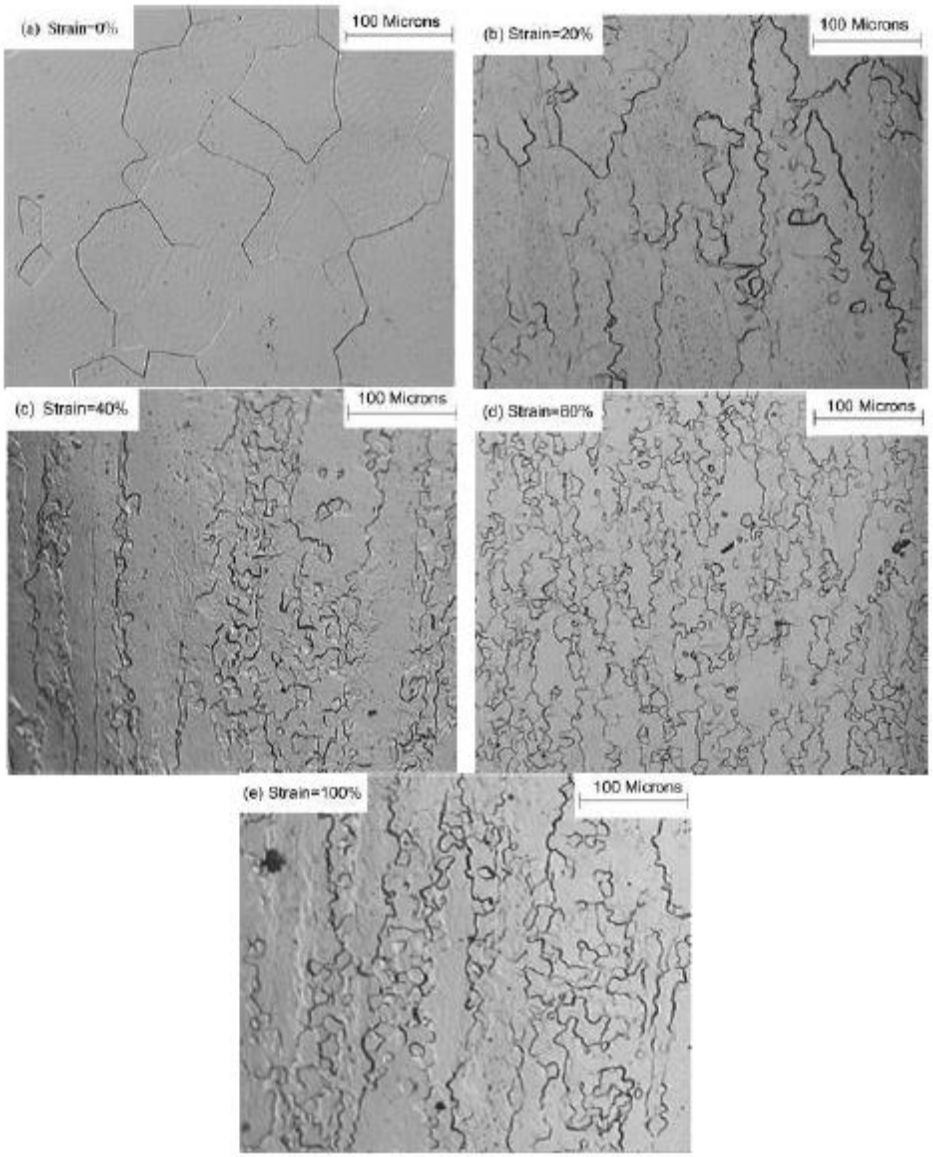

Figure 2.28 Optical micrographs of Ti-15V-3Cr-3Sn-3Al alloy at different strain values and at 850^{o}C with strain rate of 0.001s^{-1} [99]

2.11. Monotonic Behavior of UFG Materials at Elevated Temperatures

Several research works focused on monotonic behavior and stability of UFG materials at elevated temperatures [100–103]. It was observed that SPD processing can increase flow stress levels in UFG materials during hot deformation up to a specific

deformation temperature. Deforming UFG materials above that specific temperature led to recrystallization of UFG structure. Fig. 2.29 displays true stress-strain curves for severely deformed AlMg6 alloy at different deformation conditions. It was found that SPD could improve strength of AlMg6 alloy up to 520^{o}C [102].

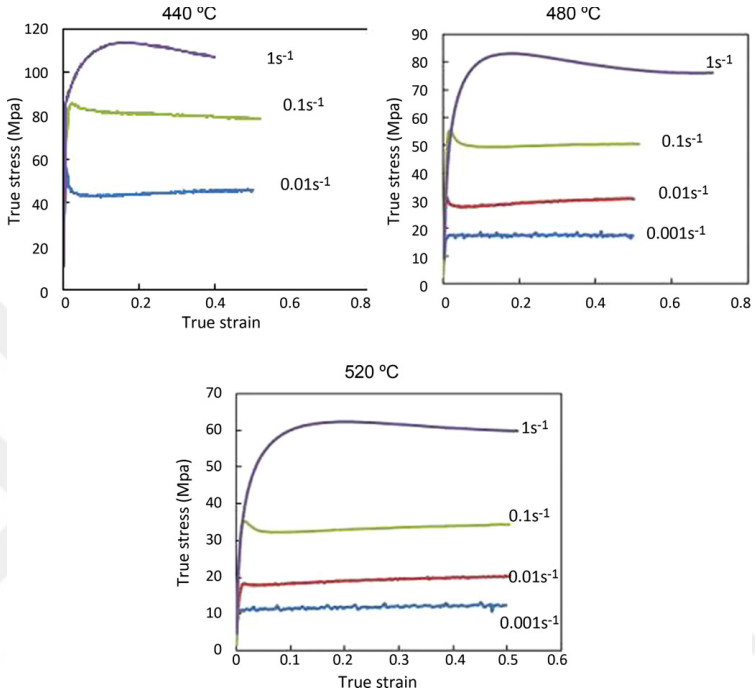

Figure 2.29 True stress-strain curves of severely deformed AlMg6 alloy at various deformation conditions [102]

2.12. Cyclic Behavior of UFG Materials at Elevated Temperatures

Recently, cyclic properties of some UFG materials at elevated temperatures have been also investigated in order to obtain thermal stability of UFG structure under cyclic deformation [54,104–107]. Cyclic deformation response and the corresponding EBSD maps of UFG interstitial-free (IF) steel at various temperatures are shown in Fig. 2.30 and Fig. 2.31, respectively. Cyclic stability of UFG IF steel was reported to be up to 200^{o}C. At temperatures exceeding 200^{o}C, localized grain growth resulted in inferior cyclic

deformation response in UFG IF steel. The critical homologous temperature (T_h) was calculated as 0.26 for UFG IF steel [105].

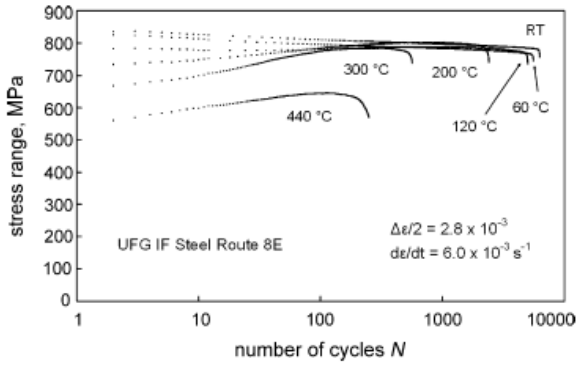

Figure 2.30 Cyclic deformation response of UFG IF steel at different temperatures [105]

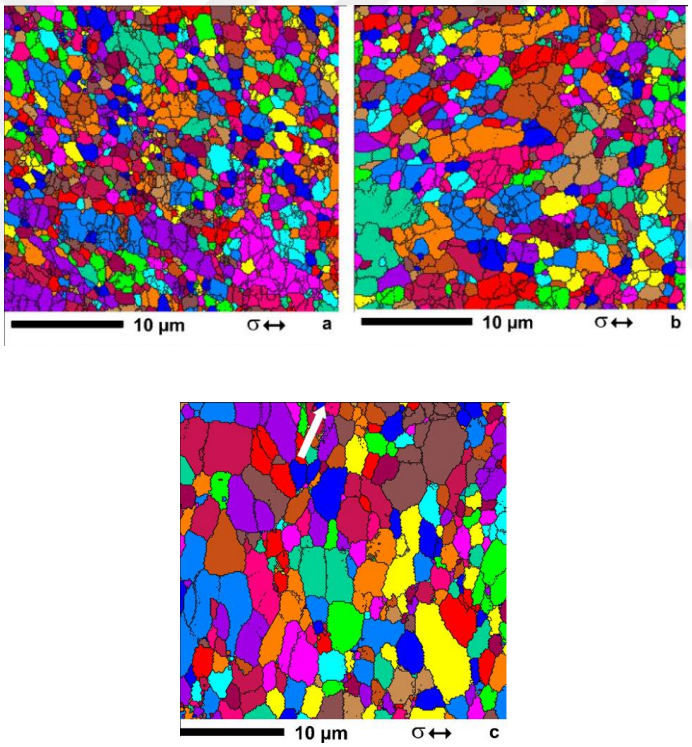

Figure 2.31 EBSD grain maps of the UFG IF steel after cyclic loading with a strain amplitude of 2.8×10^{-3} at (a) room temperature, (b) 200°C, and (c) 440°C [105]

Cyclic deformation response of Al-Mg alloys at elevated temperature was also probed [106]. Fig. 2.32 shows the cyclic deformation response and the corresponding EBSD maps of AlMg2 alloys at various temperatures. At and above 150°C, cyclic stability

of Mg-Al alloys is degraded which was attributed to the occurrence of softening mechanisms [106].

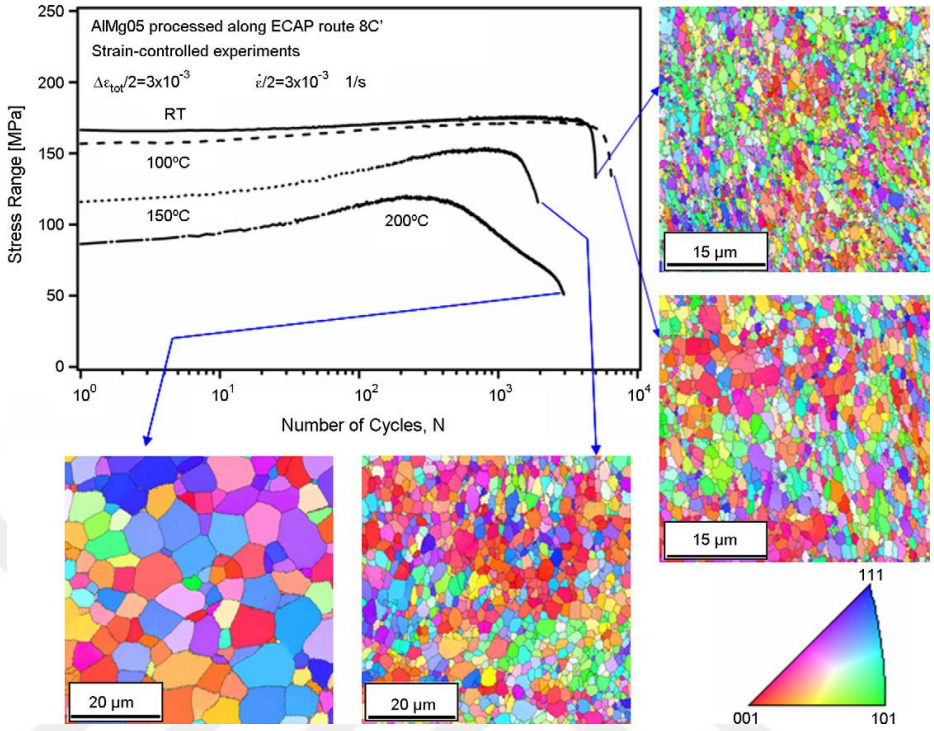

Figure 2.32 The cyclic deformation response and the corresponding EBSD maps of AlMg2 [106]

High temperature fatigue behavior of boron-modified Ti–6Al–4V alloy was also investigated [54]. The effect boron content on cyclic response of Ti–6Al–4V alloy is shown in Fig. 2.33. It was stated that boron additions noticeably resulted in the drop of as-cast grain size and hence improved the fatigue performance of Ti–6Al–4V alloy [54].

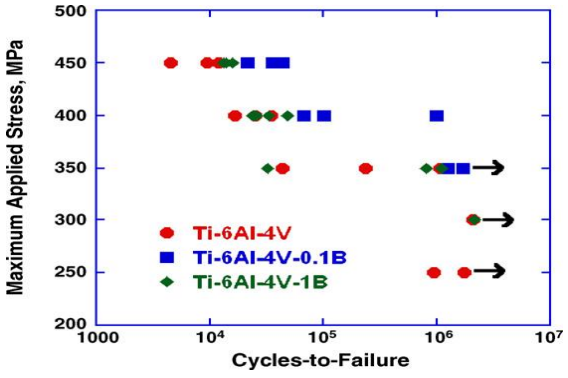

Figure 2.33 Maximum stress versus number of cycles to failure [54]

3. Experimental Procedure

3.1. Chemical Composition of Investigated Materials

CP grade 2 and grade 4 Ti were received in bar form with the composition listed in Table 3.1.

Table 3.1 Chemical composition of materials used in this study

Materials (wt.%)	C	Fe	H	N	O	Al	V	Cr	Mo	Zr	Ti
CP Grade 2 Ti	0.008	0.041	0.002	0.006	0.15	-	-	-	-	-	Balance
CP Grade 4 Ti	0.012	0.206	0.0028	0.009	0.30	-	-	-	-	-	Balance

3.2. Equal Channel Angular Extrusion

The bars were coated with a graphite base lubricant before extrusion and were heated in a furnace to the deformation temperature where they were held for 1h before extrusion. The minimum deformation temperature that allowed for processing without shear localization and macroscopic cracking for a 90^{o} ECAE die was determined to be 300^{o}C for grade 2 Ti. The extrusion of grade 4 Ti was more challenging due to its higher impurity content resulting in lower ductility. Therefore, successful extrusions of grade 4 were possible only at 450^{o}C. Extrusion took place at a rate of 1.27 mm/s. Eight ECAE passes were performed following route E and B_C accumulating a total strain of 9.24 in the as-processed material. Route E and B_c were selected as the ECAE processing route resulting in the largest fully worked region in a given billet with high volume fraction of high-angle grain boundaries [37]. Route E consists of an alternating rotation of the billet by $+180^{o}$ and $+90^{o}$ around its long axis, while in route B_C, the billet was rotated $+90^{o}$ around its long axis, between each successive pass. Following each extrusion pass, the

billets were water quenched to maintain the microstructure achieved during ECAE. Lowest possible processing temperatures were crucial in preventing possible recrystallization and partly achieved using the sliding walls concept [108]. Schematic diagram of ECAE route E showing the directions can be seen in Fig. 3.1.

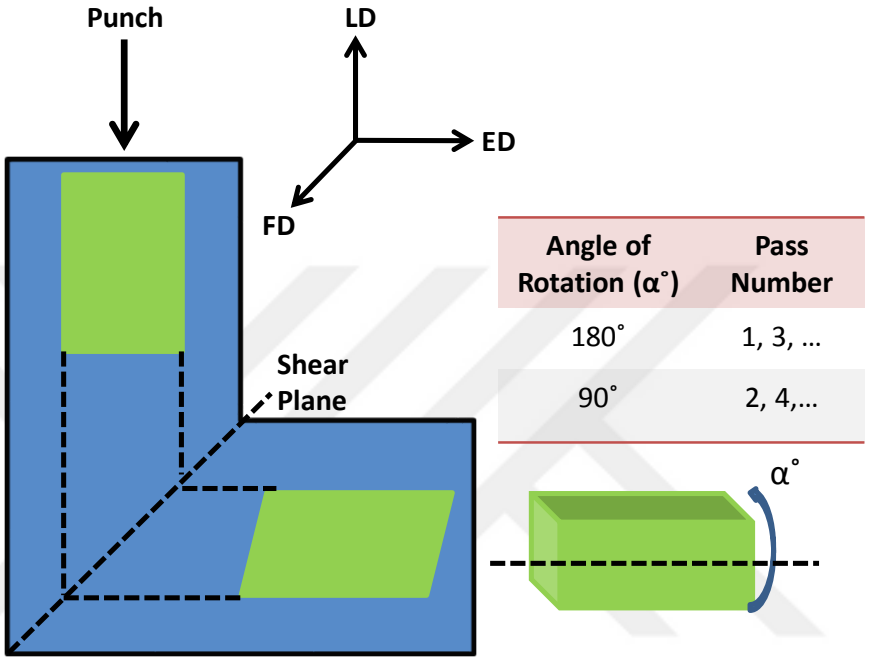

Figure 3.1 Schematic diagram of route E processing for ECAE

3.3. High Temperature Tension and Compression Tests

In exploring the hot deformation behavior of ECAE processed pure Ti, hot compression experiments were performed. The compression specimens were electro-discharge machined in rectangular block shape, 4mm×4mm×8mm, with compression axis parallel to the extrusion direction. All samples were ground and polished to remove major scratches and eliminate the influence of residual layer from electro-discharge machining (EDM). The compression tests were conducted under isothermal conditions at three different strain rates of 0.001, 0.01 and $0.1s^{-1}$ and at temperatures of 600, 700, 800 and $900^{o}C$. All specimens were heated up to the deformation temperature and then the

samples were deformed in a single loading step. The reduction in height at the end of the compression tests was 60% (true strain: 0.9) to avoid barreling and to capture the effect of both dynamic recovery and recrystallization on deformation behavior. In addition, lubrication with graphite was used during hot compression tests to decrease friction effects and minimize barreling [109]. The mechanical experiments were conducted inside a temperature-controlled furnace mounted on an Instron mechanical testing frame with uniformly heated samples having constant temperatures throughout the tests (Fig. 3.2). In this research work, tension tests were also conducted. The test specimens were electro-discharge machined with tension axis parallel to the extrusion direction and the gauge length of 15mm. All specimens were ground and polished to remove major scratches and eliminate the influence of residual layer of machining. The tension tests were performed under isothermal conditions at three various strain rates of 0.001, 0.01 and $0.1s^{-1}$ and at temperature ranging from 25-600^{o}C. For elevated temperature tests, all specimens were heated up to the deformation temperature and then the samples were deformed in a single loading step. The specimen temperature was monitored during the tests using K type thermocouples.

Figure 3.2 Hot tension/compression test set up (INSTRON 8872)

3.4. Micro-Hardness Measurements

Micro-vickers hardness tests were carried out by a Future Tech micro-hardness tester (FM-300e) on the samples with 1kg force and 10s indentation duration at ambient temperature. Each hardness value was calculated from an average of 5 indentations.

3.5. Fatigue Experiments

Low cycle fatigue (LCF) experiments were conducted on flat dog-bone shaped samples with a gage section of 20mm×5mm×1.5mm, which were electro-discharge machined with axis parallel to the extrusion direction. All samples were ground and polished to remove major scratches and eliminate the influence of residual layer from electro-discharge machining (EDM). Cyclic tests were carried out under isothermal conditions at three different strain amplitudes of 0.2, 0.4 and 0.6% and at temperatures of 25, 400 and 600^{o}C. An MTS 793 servo-hydraulic test frame controlled with an MPT software was used to performed fatigue experiments. All LCF tests were conducted under constant strain rate of 0.006s^{-1} which was chosen according to the previous studies for a better comparison [73,105]. Fatigue experiments were carried out under a fully reversed constant total strain amplitude (R = -1). A delicate high-temperature extensometer with ceramic rods was used to measure strain amplitudes during cyclic tests.

3.6. Metallography Examinations and Microstructure

Optical microscopy (OM) was used to monitor the changes in the microstructure. The specimens were prepared using standard polishing techniques and then etched with Kroll's reagent (3 ml HF + 6 ml HNO_3 in 100 ml distilled water). The linear intercept method was used to estimate the grain size. A CAMSCAN MV 2300 scanning electron microscopy (SEM) with an accelerating voltage of 20 kV and Oxford Instrument electron

backscatter diffraction (EBSD) were also utilized to study the microstructure and fracture surfaces of specimens at different conditions. The Kikuchi bands are identified utilizing a computer software to obtain the crystal orientation. EBSD results were analyzed by OIM software.

3.7. Analysis of Damping Properties

Damping properties were examined by a TA Q800 dynamical mechanical analyzer (DMA). The DMA specimens with dimensions of 35mm×3mm×0.7mm were electro-discharge machined. Dual cantilever mode in which two ends of the specimen were fixed was utilized to measure damping capacity. The dynamic modulus and elastic internal friction were obtained as a function of time and temperature. Measurements were made at a constant frequency of 1Hz and at strain amplitudes of 0.01 and 0.05%.

4. Workability Characteristics and Mechanical Behavior of Severely Deformed Commercial Purity Grade 2 Ti at High Temperatures

4.1. Microstructural Evolution

The initial microstructure of as-received Ti is shown in Fig. 4.1a. It can be easily observed that the structure consists of coarse grains with an average grain size of 43 µm. The microstructure of the as-received Ti subjected to eight passes of ECAE is demonstrated in Fig. 4.1b. ECAE processing leads to a significant refinement in the microstructure and transforms the coarse grained as-received microstructure to one with ultrafine grains after eight passes. In addition, micrographs depicting the microstructural evolution before and after hot compression testing are also demonstrated. The microstructure of UFG Ti followed by 3 min annealing at 600^{o}C and 900^{o}C can be seen in Fig. 4.1c and d, respectively. Annealing period is selected based on the time it takes to achieve uniform heating of the samples at the desired compression test temperature. After the 600^{o}C heat treatment, the microstructure consists of both slightly coarsened grains and regions with ultrafine grains. In contrast, the 900^{o}C heat treatment resulted in severe coarsening of the structure with an average grain size of 25µm. The existence of several recrystallized equiaxed grains can be observed in Fig. 4.1d. Considering the development of microstructure during hot compression, the micrographs after deformation at 600^{o}C and 900^{o}C can be seen in Fig. 4.1e and f, respectively. The sample subjected to compression at 600^{o}C exhibits a fine and homogeneous microstructure with slightly larger grains in comparison with those of the pre-compression sample. After

compression at 900^{o}C, the microstructure contained a mixture of fine and coarse grains. The evolution of such a microstructure could be attributed to the deformation of the recrystallized grains that formed during the pre-test heat treatment and the formation dynamically recrystallized during the compression test.

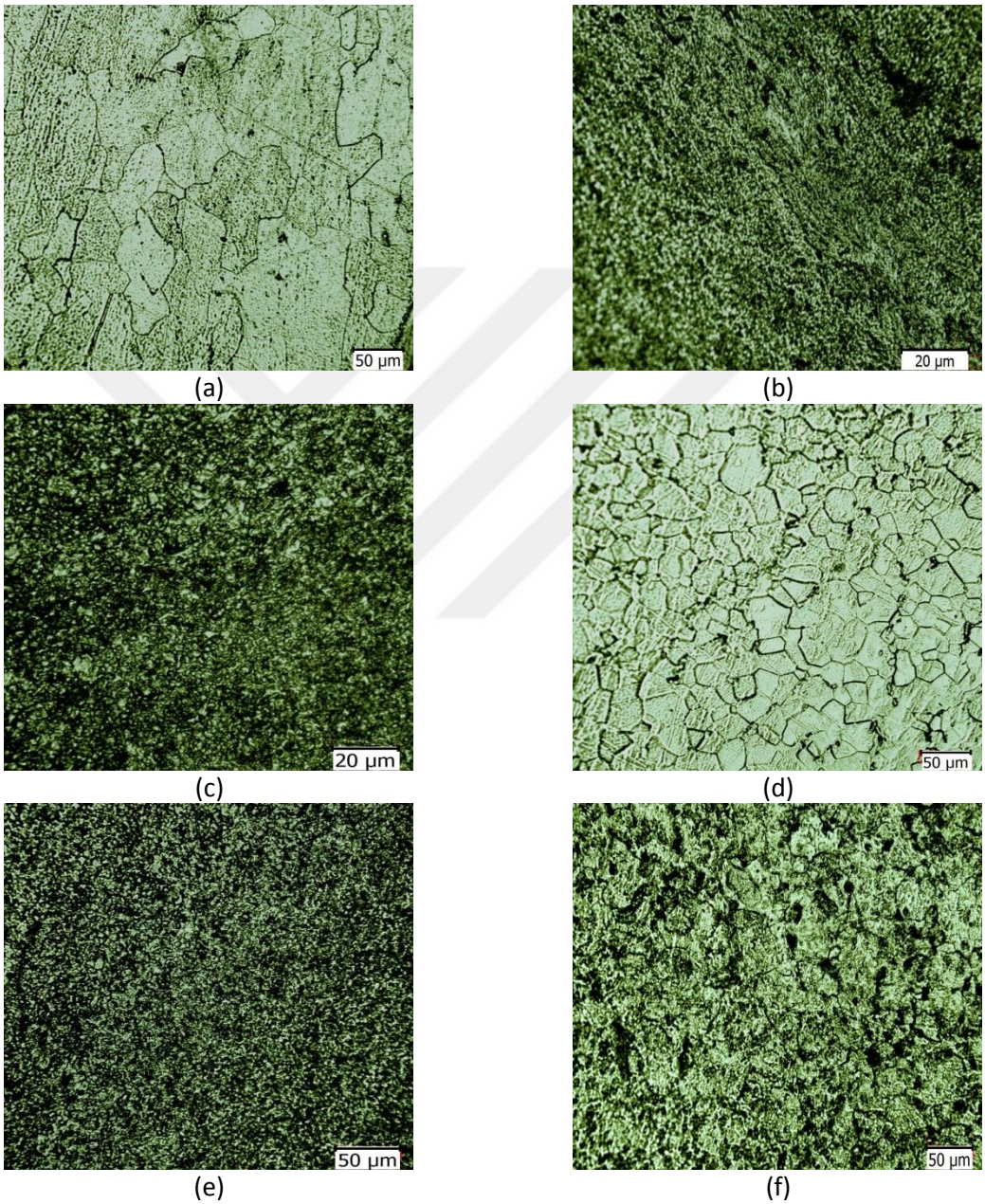

Figure 4.1 The microstructure of pure Ti a) in as-received condition, b) after 8 passes of ECAE processing, c) after 8 passes of ECAE processing followed by 3 minutes of annealing at 600^{o}C, d) after 8 passes of ECAE followed by 3 minutes of annealing at 900^{o}C, e) after 8 passes of ECAE processing followed by compression at 600^{o}C with a strain rate of 0.1s^{-1}, f) after 8 passes of ECAE processing followed by compression at 900^{o}C with a strain rate of 0.1s^{-1}.

4.2. Mechanical Properties of Grade 2 Ti at Elevated Temperature

Fig. 4.2 shows the true stress–true strain curves for the compression tests of severely deformed pure Ti at various temperatures for the strain rates of 0.001, 0.01 and $0.1s^{-1}$. It can be observed that the flow stress of pure Ti subjected to ECAE is sensitive to both temperature and strain rate. In the previous work on the high temperature flow behavior of pure Ti with 40 µm grain size, compressive responses were depicted up to $700^{o}C$ [15]. In comparison with the present results, it can be seen that ECAE could increase the high temperature strength of pure Ti up to as high as $700^{o}C$. The rise of flow stress levels in UFG materials during hot deformation was also reported for an aluminum 6063 alloy at a temperature range of 300–$450^{o}C$ [101].

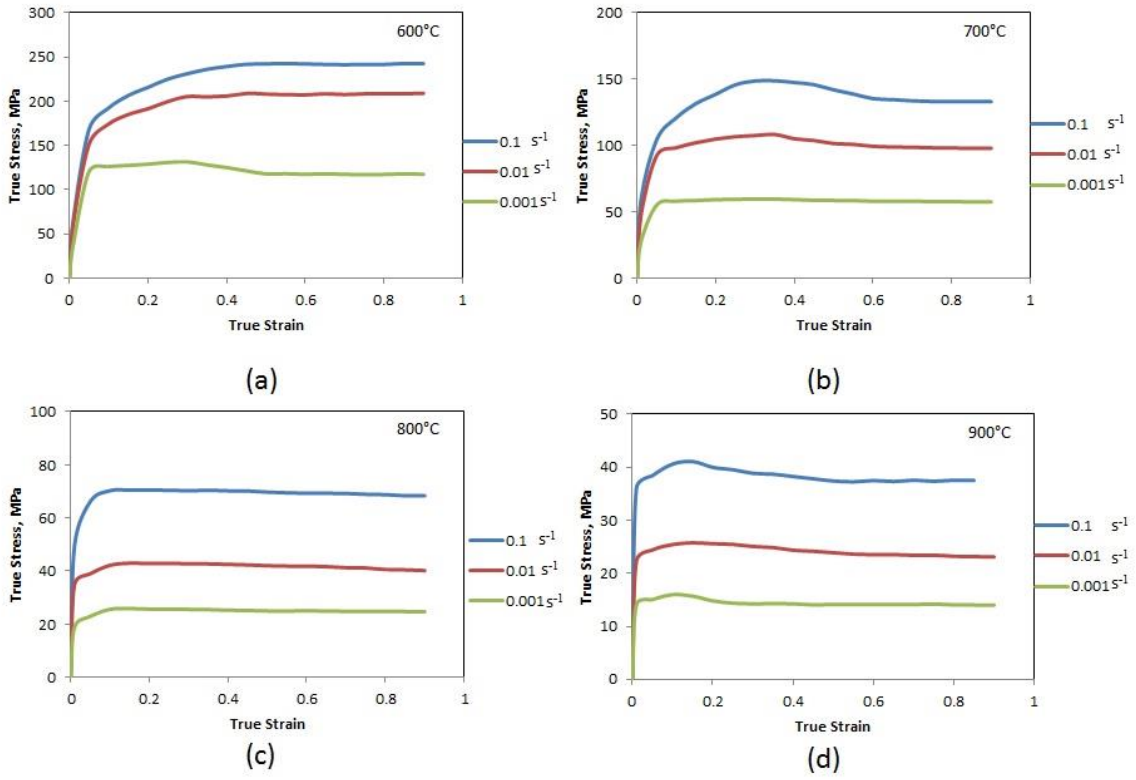

Figure 4.2 True stress–true strain response of severely deformed Ti with different strain rates at (a) $600^{o}C$, (b) $700^{o}C$, (c) $800^{o}C$, and (d) $900^{o}C$

The microstructural and tensile observations can also be traced by the trend in hardness properties before and after hot deformation. It can be seen in Table 4.1 that the hardness of CP titanium demonstrates a dramatic rise after severe deformation via ECAE processing. This two-fold increase cannot be sustained during annealing at elevated temperatures. Still after 3 minutes exposure to 900^{o}C, more than 30% increase in hardness can be achieved. Micro-hardness values for deformed samples also showed a tendency to drop with increasing deformation temperature, which could be attributed to higher fraction of dynamically recrystallized grains [110]. The 600^{o}C deformed sample retained 50% of the hardness increase achieved in the UFG microstructure.

Table 4.1 Hardness of severely deformed CP titanium, before and after hot compression

Condition	**Average Micro-hardness (HV)**
As-Received	167 ± 2
ECAE processed	326 ± 4
ECAE processed followed by 3 minutes of annealing at 600°C	285 ± 3
ECAE processed followed by 3 minutes of annealing at 700°C	251 ± 3
ECAE processed followed by 3 minutes of annealing at 800°C	233 ± 2
ECAE processed followed by 3 minutes of annealing at 900°C	219 ± 3
ECAE processed followed by compression at 600°C and 0.001s^{-1}	250 ± 2
ECAE processed followed by compression at 700°C and 0.001s^{-1}	243 ± 2
ECAE processed followed by compression at 800°C and 0.001s^{-1}	226 ± 3
ECAE processed followed by compression at 900°C and 0.001s^{-1}	206 ± 3

At all deformation temperatures, the flow stress levels slightly increase to a peak and then decrease gradually to a steady state level. Regardless of the strain level (low, peak or high), the flow stress levels show similar dependence to deformation temperature and strain rate. Fig. 4.3 exhibits this behavior for the case of peak strain, i.e. strain corresponding to peak flow stress. Such flow behavior is a typical characteristic of hot working that is accompanied by dynamic recrystallization softening. The work hardening at 600^{o}C is higher than those obtained at temperatures above it. In contrast, the flow stress levels exhibit slight transitional drops indicating thermal softening for deformation temperatures above 600^{o}C. The observed stress levels decrease with increasing temperature and decreasing strain rate because lower strain rates and higher temperatures provide longer time for energy accumulation and higher dislocation mobility around boundary regions. This evidently results in the nucleation and growth of dynamically recrystallized grains and dislocation annihilation.

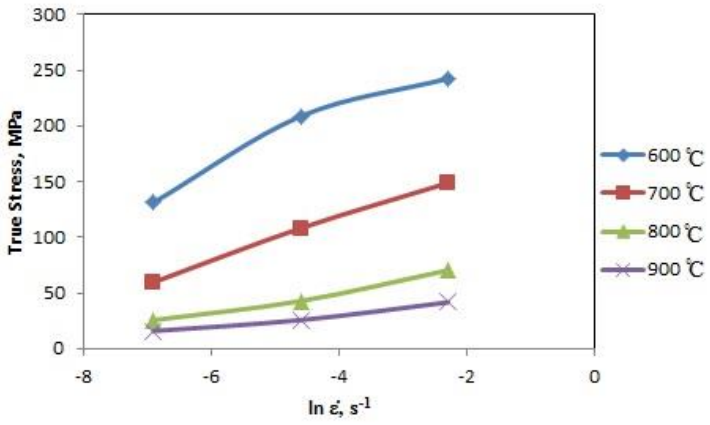

Figure 4.3 The variation of peak stress as a function of strain rate

Fig. 4.4 summarizes the values of peak strain as a function of deformation temperature and strain rate. It is worth noting that the effects of temperature and strain rate are significant on the peak strain level during hot deformation. For most materials both in pure and alloy form, the peak strain decreases with higher temperatures or lower

strain rates [111,112]. A similar behavior was observed for the case of Ti after SPD. As can be seen in Fig. 4.4, the peak strain value at any given temperature increases with increasing strain rate, though the effect is mostly pronounced at the lowest testing temperature of 600^{o}C. Since DRX typically initiates at a critical strain before the peak stress [113], it is accelerated by the rise in temperature and the drop in strain rate. Although, Ti and its alloys are generally considered as high stacking fault energy SFE materials that are expected to be softened mainly by DRV and DRX processes have also been found to take place depending on the deformation parameters [114–116]. In the present study, especially at temperatures above 600^{o}C and/or strain rates below 0.01s^{-1}, occurrence of DRX related phenomena is favored. With increasing deformation temperatures, the sensitivity of peak strain to strain rate diminishes. Still, both applied strain rate and deformation temperature are important parameters that dictate the amount of critical strain required for the onset of DRX in ECAE processed pure Ti.

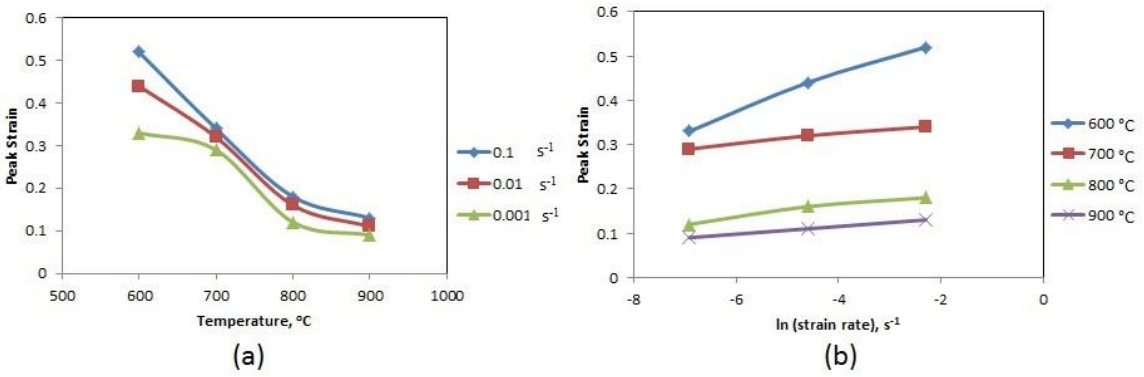

Figure 4.4 Peak strain versus (a) deformation temperature (b) strain rate

A power law relationship between steady state stress and DRX grain size has been reported for various types of dynamically recrystallized materials [117,118].

$$\sigma_{SS} = K' D_{DRX}^{-N} \quad (1)$$

Where K' and N are the material constants, σ_{SS} and D_{DRX} are steady state flow stress and dynamically recrystallized grain size, respectively. It is worth noting that,

increasing steady state stress leads to a reduction of DRX grain size at high strains [119]. Therefore, it can be expected that the size of dynamically recrystallized grains decreases at 600^{o}C due to higher steady state stress at lower deformation temperature.

In order to understand the effect of ECAE on CP titanium flow curves at elevated temperatures, severely deformed CP titanium and annealed CP titanium experimental results were compared in Table 4.2. The results show that ECAE procedure is capable of increasing the high temperature strength of CP titanium. The average flow strength increase was 49% and 33% at temperatures of 600^{o}C and 700^{o}C, respectively. It is well known that severely deformed materials are prone to severe recovery and recrystallization due to the high dislocation density and fraction of sub-grain and grain boundaries. Therefore, it is probable that softening mechanisms such as DRV and DRX are highly operative above 600^{o}C, disturbing the thermal stability of the severely deformed microstructure. It is worth noting that the rise of flow strength in severely deformed titanium can also be attributed to effects of texture since mechanical properties of HCP materials are sensitive to texture evolution [3,120]. The rise of flow stress levels in UFG materials during hot deformation was also reported at a temperature range of 300^{o}C to 450^{o}C for Al6063 alloy [121]. The increase in strength of UFG Al was attributed to the effect of the dislocation substructure and the high density of grain boundaries. Another study showed that higher strength levels were observed up to 500^{o}C for UFG Ti–6Al–4V alloy in comparison with its coarse structure; the effect of UFG microstructure diminished above 500^{o}C [122].

Table 4.2 Experimental flow stress levels of severely deformed CP titanium

Compression test condition temperature / strain rate (˚C / s^{-1})	The steady flow stress of UFG CP titanium (MPa), Present Study	The steady flow stress of annealed CP titanium (MPa) [15]	The percentage of hot strength improvement (%)
600˚C / 0.1s^{-1}	241	170	42
600˚C / 0.01s^{-1}	207	130	59
600˚C / 0.001s^{-1}	117	80	46
700˚C / 0.1s^{-1}	132	100	32
700˚C / 0.01s^{-1}	98	70	40
700˚C / 0.001s^{-1}	57	45	27

From a structural perspective, the severely deformed microstructure in CP titanium brings an improved strength of up to 49% over its coarse grained counterpart in the quasi-static regime and at a high temperature of 600^{o}C. From a metal forming perspective in the high temperature regime, deformation over 700^{o}C could be preferred since the flow stress levels remained below 100MPa at tested strain rates.

4.3. Workability Characteristics of Grade 2 Ti at Elevated Temperature

Strain rate sensitivity is a significant property, which can affect workability of materials and deserves investigation for severely deformed pure Ti. Strain rate sensitivity, m, is related to the effect of strain rate on dislocation generation and propagation and as such is an index of workability. The following well-known relation was employed to calculate the strain rate sensitivity, m, for hot deformation.

$$m = \frac{\partial \ln(\sigma)}{\partial \ln(\dot{\varepsilon})}\Big|_{\varepsilon} \qquad (2)$$

The values of m can be obtained from the slope of the lines plotted according to Eqn. (2) at a constant strain. The variation of the strain rate sensitivity as a function of

strain is plotted in Fig. 4.5 exhibiting strong dependence to deformation temperature. This phenomenon can be attributed to the increased activity of diffusion related mechanisms and dynamic recrystallization at higher temperatures that produces higher strain rate sensitivity [123]. It is worth noting that strain rate sensitivity shows a considerable increase above 700^{o}C. The strain rate sensitivity values obtained at 800^{o}C are slightly greater than those obtained at 900^{o}C for the whole strain interval. It is expected that m values increase with the rise of deformation temperature due to thermally activated mechanisms. However, constancy of m can be attributed to the onset of DRX processes which may occur over a range of strain rates and temperatures [9,124]. In the present case, dominance of DRX around 800 to 900°C might explain the similar strain rate values at both temperatures. Considering the strain dependence of rate sensitivity, the m values at 600^{o}C and 700^{o}C remarkably increase and peak at a strain of 0.5 and 0.35, respectively. Then, the m values decrease with increasing strain and plateau at a constant value. Similar behavior is observed at a less pronounced degree for 800^{o}C, where the strain rate sensitivity peaks at a strain level of 0.25 and then drops gradually and remains almost constant for the rest of the strain range. At the highest deformation temperature, m is fairly constant and can be considered to be independent of true strain. It can be concluded that for severely deformed Ti, higher strain rate sensitivity levels are observed with increasing deformation temperature as expected. However, m is not a strong function of strain at or above 800^{o}C.

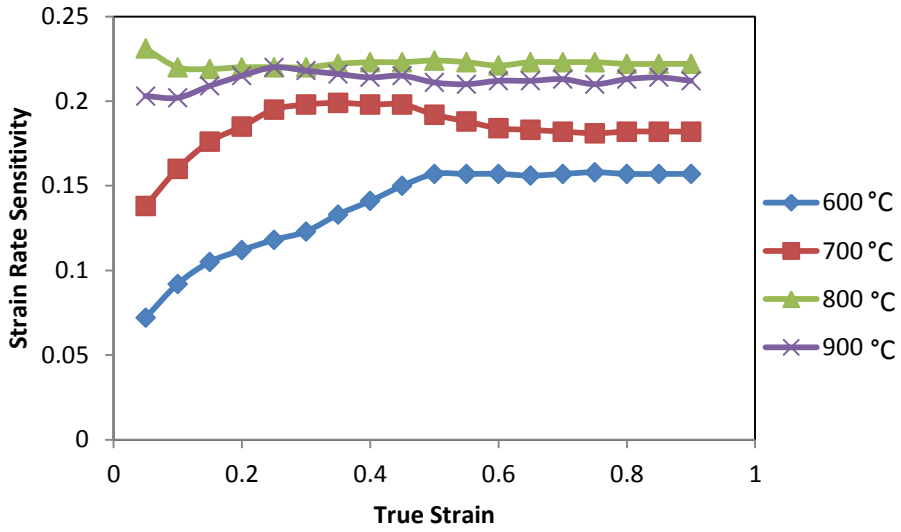

Figure 4.5 Strain dependence of strain rate sensitivity at various temperatures

The other crucial factor affecting the elevated temperature deformation behavior is the strain hardening rate, γ, which is defined as:

$$\gamma = \frac{1}{\sigma}\left(\frac{d\sigma}{d\varepsilon}\right)\Big|_{\dot{\varepsilon}} \qquad (3)$$

where, σ is the flow stress, $\dot{\varepsilon}$ is the strain rate and ε is the true strain. The variation of strain hardening rate values with strain at different temperatures and strain rates is presented in Fig. 4.6. The strain hardening rates during hot deformation, as defined in Eq. (3), exhibit sharp decrease at low strain levels (below 0.2) while it stays almost constant at higher strains. Moreover, again at low strains levels, higher deformation temperatures result in lower strain hardening rates, indicating the dominance of dislocation rearrangement and recovery mechanisms. Since more recrystallization is expected at higher temperatures and lower strain rates, increased softening and thereby reduced flow stress levels after peak stress could be attributed to a higher volume fraction of recrystallized grains in the microstructure [109]. Irrespective of the deformation temperature and strain rate, constant γ was observed at above true strain levels of 0.2.

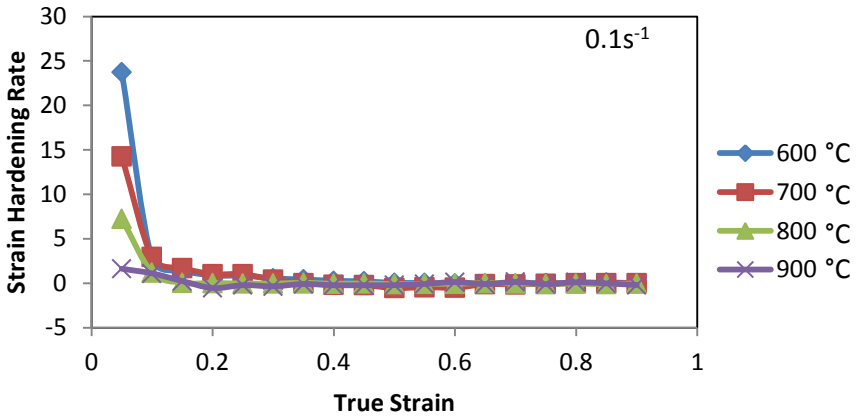

(a)

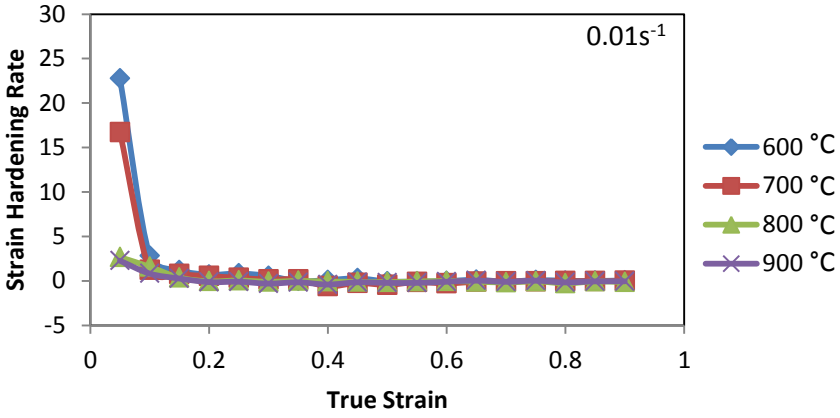

(b)

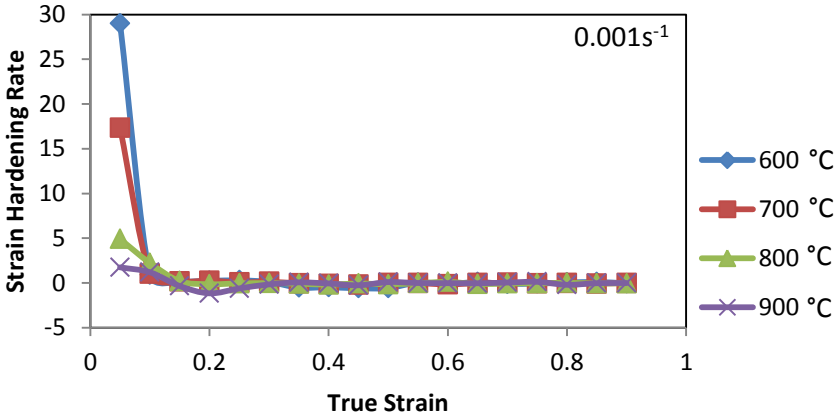

(c)

Figure 4.6 Variation of strain hardening rate values with strain at different temperatures at strain rate of (a) $0.1s^{-1}$ (b) $0.01s^{-1}$ (c) $0.001s^{-1}$

In order to estimate workability of metals and alloys under hot deformation conditions, flow localization parameter (FLP) has been proposed [125,126]. This factor can be represented as follows:

$$FLP = \frac{\gamma}{m} \quad (4)$$

Using eqn. (4), the average flow localization parameters for the whole strain range at different temperatures and strain rates, are calculated and summarized in Table 4.3.

According to Table 4.3, FLP values increase with decreasing deformation temperature and increasing strain rate. It was stated that the materials with FLP≥5 are prone to flow localization [125,126]. Therefore, it is expected that UFG Ti is not expected to have favorable workability at temperatures below 800^{o}C due to flow localization. The values of FLP were highest and exceed 21 at 600^{o}C for all strain rates. The high magnitude of flow localization can be attributed to the lack of dynamic recrystallization, which might eventually result in failure [127]. In contrast, the values of FLP in all strain rates remain less than 2 at 800 and 900^{o}C. The effect of strain rate on the FLP is less straightforward. Despite this, highest FLP values are observed for the highest deformation rates for all temperatures. It is clear that the ductile behavior during hot working of severely deformed pure titanium is closely associated with deformation temperature and to a smaller extent with deformation rate. With reduced tendency to flow localization, deformation over 700^{o}C could be preferred for metal forming purposes in severely deformed Ti.

Table 4.3 Flow-localization parameter under different temperatures and strain rates

Strain Rate	600°C	700°C	800°C	900°C
$0.1s^{-1}$	22.45	7.35	1.91	0.29
$0.01s^{-1}$	21.02	7.15	0.80	0.35
$0.001s^{-1}$	22.13	7.29	1.56	0.13

4.4. Determination of the Activation Energy (Q)

Constitutive equations proposed by Zener and Hollomon have been used to model the deformation behavior of the present material at high temperatures. In hot working processes, several constitutive equations have been applied [101,128–130], where Z can be determined from:

$$Z = \dot{\varepsilon} \exp\left(\frac{Q}{RT}\right) = AF(\sigma) \quad (5)$$

Therefore:

$$\dot{\varepsilon} = AF(\sigma)\exp(\frac{-Q}{RT}) \quad (6)$$

where, $\dot{\varepsilon}$ is the strain rate, Q is the apparent activation energy for hot deformation, R is the universal gas constant, T is the absolute temperature, A, and n are material constants. $F(\sigma)$ is a function of flow stress which can be described as follows:

$F(\sigma) = A_1\sigma^n$ For low stress, (7)

$F(\sigma) = A_2\exp(\beta\sigma)$ For high stress, (8)

$F(\sigma) = A_3[\sinh(\alpha\sigma)]^n$ For all stress levels, (9)

α is a material constant. Substituting function of flow stress ($F(\sigma)$) into Eqn. (6) gives:

$\dot{\varepsilon} = B\exp(\beta\sigma)\exp(\frac{-Q}{RT})$ For high stress, (10)

$\dot{\varepsilon} = C(\sigma^n)\exp(\frac{-Q}{RT})$ For low stress, (11)

Here B and C are the material constants, taking the logarithm of eqns. (10) and (11), gives:

$(\frac{\partial \ln(\dot{\varepsilon})}{\partial \ln(\sigma_p)})_T = n$ (12)

$(\frac{\partial \ln(\dot{\varepsilon})}{\partial \sigma_p})_T = \beta$ (13)

Also α and β, which are related to each other through:

$\alpha = \frac{\beta}{n}$ (14)

The values of n and β can be obtained from the slope of the lines plotted according to Eqn. (12) and (13), respectively. As the slopes of lines are similar, the value of n and β can be calculated for different deformation temperatures using linear fitting method. Fig. 4.7a shows $\ln(\dot{\varepsilon})$ versus $\ln(\sigma)$ at different temperatures and Fig. 4.7b represents $\ln(\dot{\varepsilon})$ versus stress at different temperatures. Accordingly, the mean values of n and β can be obtained as 5.9 MPa^{-1} and 0.046 MPa^{-1}.

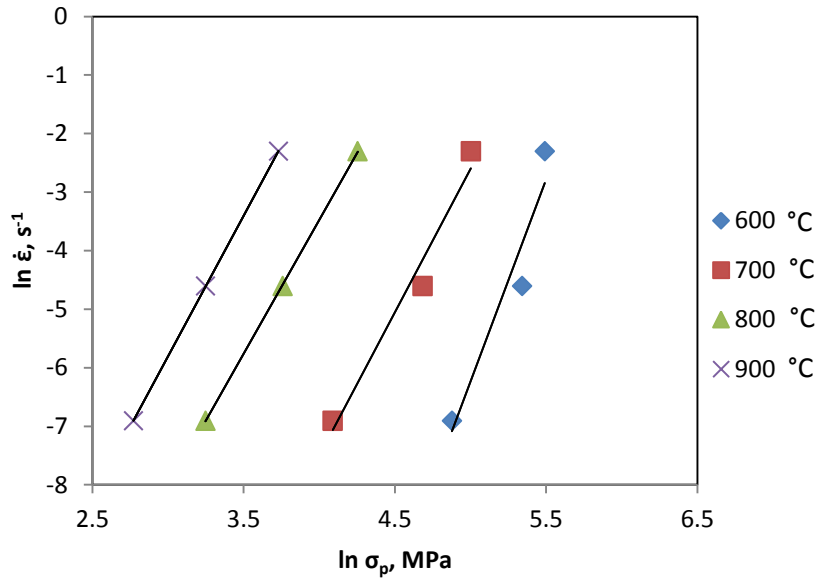

(a)

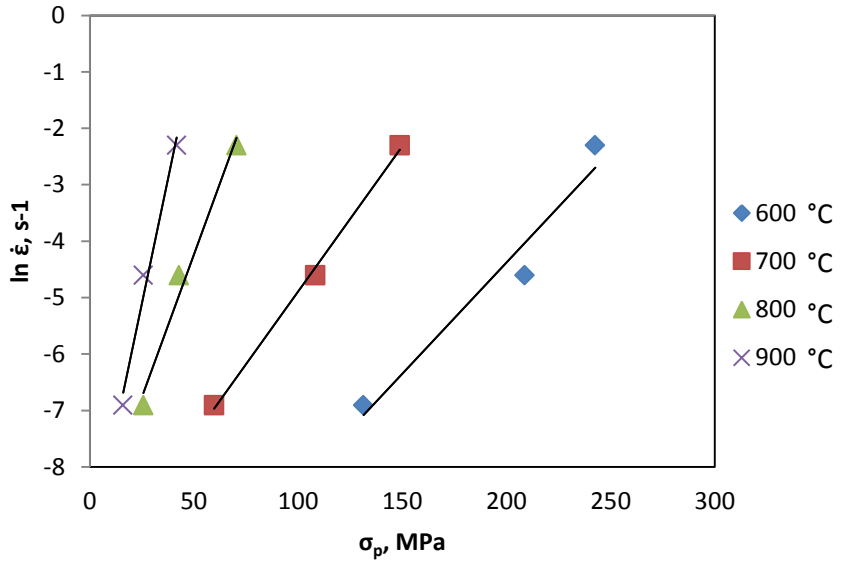

(b)

Figure 4.7 Relation between (a) strain rate and $\ln\sigma_p$, (b) strain rate and peak compressive stress values

Therefore, α can be computed from n and β as: $\alpha = \frac{\beta}{n} = 0.008\ MPa^{-1}$. For the given strain rate conditions, Q can be defined as [131]:

$$Q = nRS \qquad (15)$$

where S is:

$$S = \left(\frac{d\{\ln[\sinh(\alpha\sigma_p)]\}}{d(\frac{1}{T})}\right)_{\dot{\varepsilon}} \quad (16)$$

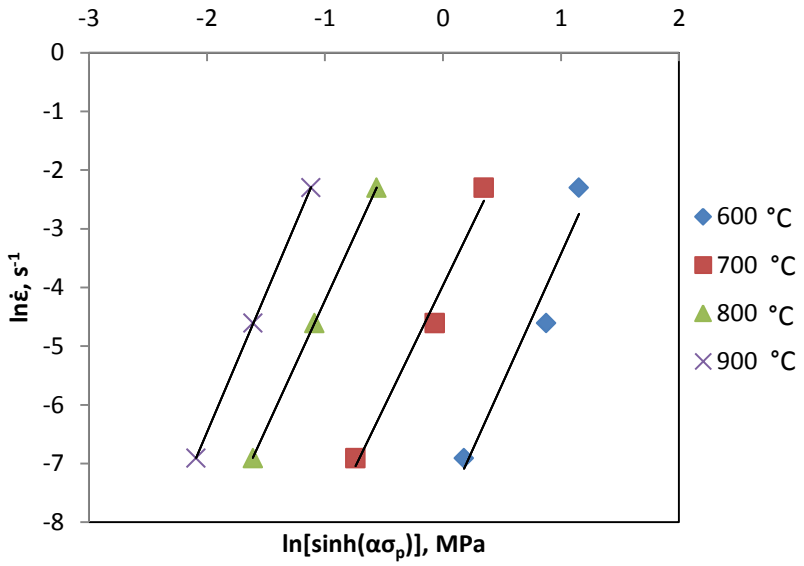

(a)

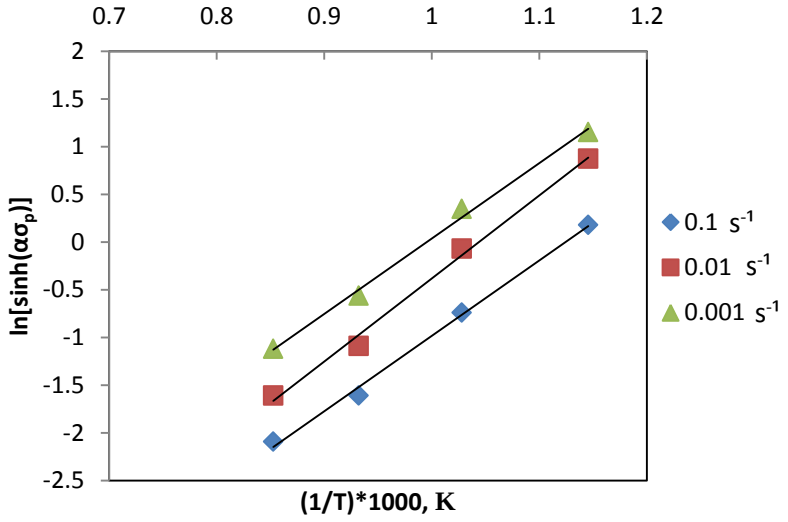

(b)

Figure 4.8 Relations between $\dot{\varepsilon}$, σ_p and T: (a) $\ln\dot{\varepsilon}$ versus $\ln[\sinh(\alpha\sigma_p)]$ plot and (b) $\ln[\sinh(\alpha\sigma_p)]$ versus 1/T plot

The value of Q can be derived from the line slope of $\ln\dot{\varepsilon}$ versus $\ln[\sinh(\alpha\sigma_p)]$ and $\ln[\sinh(\alpha\sigma_p)]$ versus 1/T plots. From the group of parallel lines in Fig. 4.8, the average value of activation energy Q can be calculated to be about 301 kJ/mol. As can be

observed in Table 4.4, the calculated activation energies in both this work and the published ones are much larger than the self-diffusion of alpha Ti [48]. In addition, the activation energy of severely deformed CP titanium is higher than that of coarse grained CP titanium [15]. ECAE processing increased the amount of activation energy for hot deformation. On the other hand, as compared to the Q value of Ti-10V-2Fe-3Al, Ti-15-3 and Ti 5-5-5-3, the severely deformed CP titanium in this work has a higher value [132–134].

Table 4.4 The comparison of activation energy (Q) values for various titanium based materials

Alloy	Q (kJ/mol)	References
Severely deformed CP titanium grade 2	**301**	**Present study**
CP titanium grade 2	**218-240**	**[15]**
Ti-10V-2Fe-3Al	**294**	[134]
Ti 5-5-5-3	**183**	[132]
Ti-15-3	**240**	[133]
Self-Diffusion in alpha titanium	**169**	[48]

Alloying elements and impurities can change the apparent activation energies, a phenomenon that is manifested by the increase in the temperature dependence of the flow stress [135]. It is worth noting that the alloying elements causing lower stacking fault energy are responsible for increasing the activation energy for diffusion by reducing the effective diffusion rate in the lattice [111]. In this investigation, it is found that the ECAE procedure can enhance the value of hot deformation activation energy. The increase of activation energy for hot deformation was also seen in other fine grained materials

[101,136]. For instance, Al6063 showed 64% increase in activation energy over its coarse grained counterpart [101].

The peak strain is an important parameter, since after peak strain, the work hardening behavior of flow stress is being replaced with work softening behavior indicating the onset of dynamic recrystallization. Fig. 4.9 shows the linear fit between the peak strain and the Zener-Holloman parameter. The peak strain can be determined below, indicating higher values with increasing the Z parameter.

$$\varepsilon_P = 0.002\, Z^{0.149} \quad (17)$$

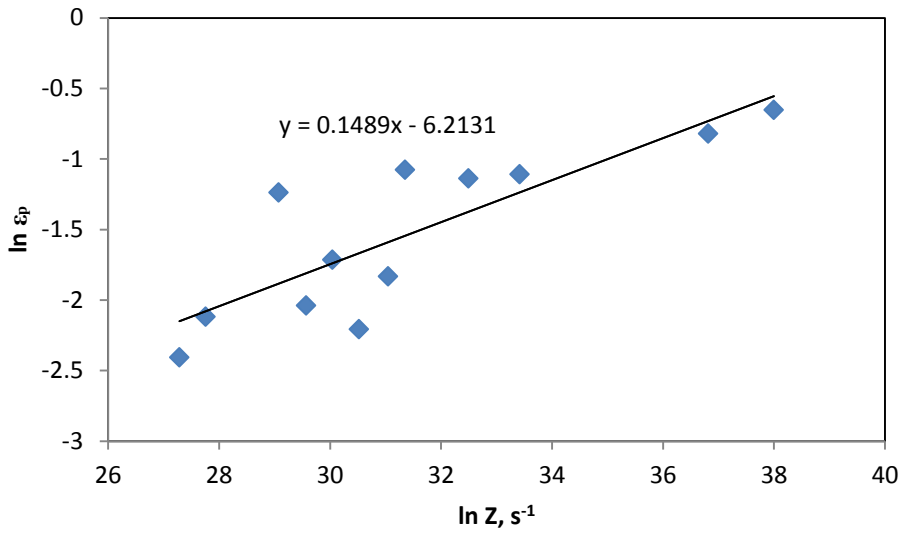

Figure 4.9 Relation between $\ln\varepsilon_P$ and Zener-Holloman parameter

It is well known that dynamic recrystallization actually initiates at a critical strain before the peak stress. It can be taken as $0.8\varepsilon_P$ [113].

$$\varepsilon_C = 0.0016\, Z^{0.149} \quad (18)$$

The critical strain values versus deformation strain rates at various temperatures are displayed in Fig. 4.10. The general tendency is that the critical strain values decrease with increase in deformation temperatures and decrease in strain rates, pointing to accelerated dynamic recrystallization behavior due to lower critical driving force.

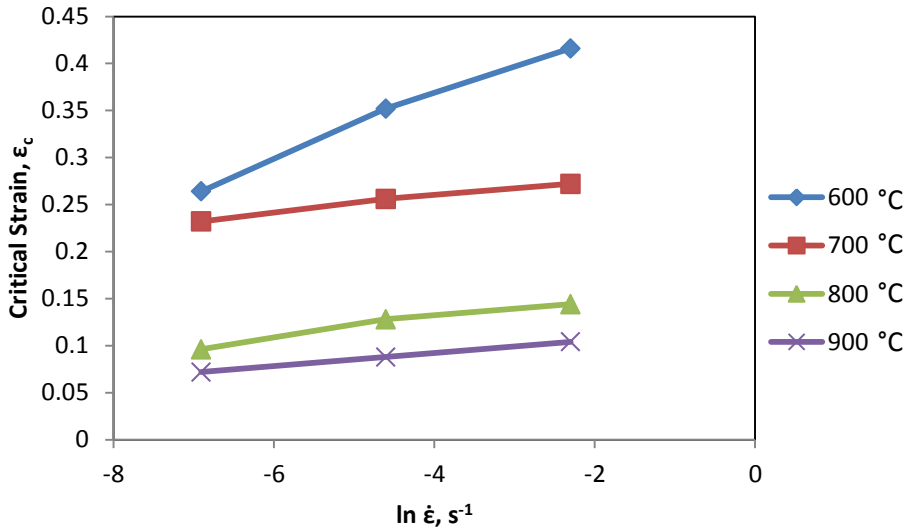

Figure 4.10 Dependence of the critical strain on the strain rate at different temperatures

5. Modeling and Prediction of Flow Stress Behavior of Severely Deformed Titanium at Elevated Temperatures

In the present research work, modeling behavior of severely deformed titanium which was obtained via ECAE process was investigated by different constitutive equations. The constitutive models are phenomenological. These modeling responses are comprehensively discussed in the present chapter.

5.1. Prediction of Flow Stress Behavior of Severely Deformed Titanium by Avrami Formulation

This section presents the fundamental relations used to describe the flow behavior in terms of work hardening (WH), DRV and DRX regions. It is well known that, due to the combined effect of work hardening and thermally activated softening mechanisms, most of the flow stress curves at elevated temperatures include four various stages especially at relatively low strain rates [137,138]: stage I (work hardening stage), stage II (transition stage), stage III (softening stage) and stage IV (steady stage). These stages can be observed in Fig. 5.1.

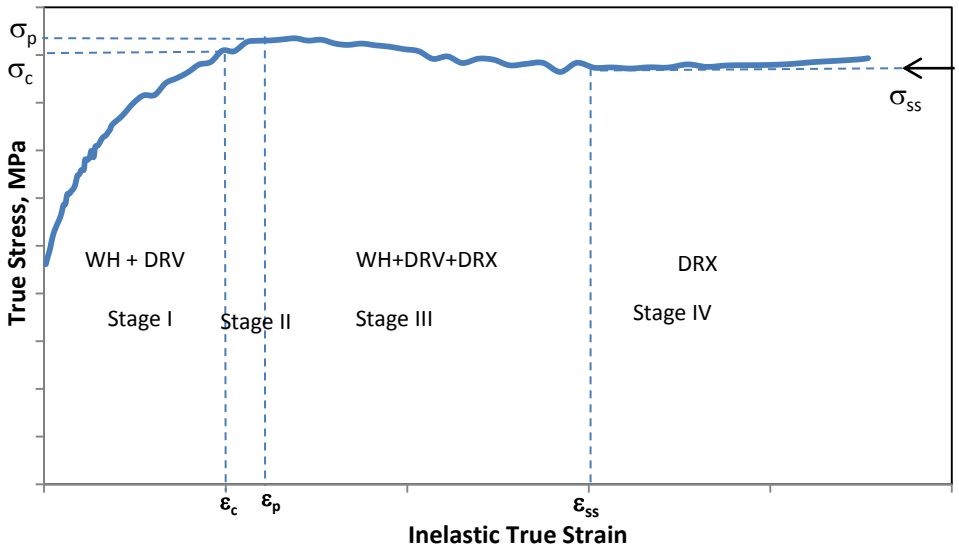

Figure 5.1 The flow stress curve can be divided into four stages: stage I (work hardening stage), stage II (transition stage), stage III (softening stage), stage IV (steady stage)

The work hardening rate overcomes the softening rate induced by DRV in stage I, and thus the stress considerably increases during initial deformation then rises at a decreased rate, followed by stage II. The competition between work hardening, and softening induced by both dynamic recovery and DRX, occurs in stage II. Usually dynamic recrystallization occurs only after a critical strain (ε_C) is exceeded [111,137]. The critical strain (ε_C) of metallic materials was observed to be less than the strain corresponding to the peak stress (ε_P). In stage II, the flow stress still increases with a continuous decrease in rate. The stress drops sharply, which is related to dominance of dynamic recovery and dynamic recrystallization in stage III. Finally, the stress levels off and the plateau formation in stage IV indicates a new balance between thermal softening and work hardening in newly recrystallized grains.

5.1.1. Constitutive equations for Stage I

Laasraoui and Jonas proposed the variation of dislocation density during deformation according to work hardening and dynamic recovery with the following equation [135]:

$$\frac{d\rho}{d\varepsilon} = U - \Omega\rho \quad (1)$$

where $\frac{d\rho}{d\varepsilon}$ is the rate of increase of dislocation density with strain, U represents the work hardening, ρ is the dislocation density and Ω is called the coefficient of dynamic recovery [113,137]. Assuming U and Ω are strain independent, integrating eqn. (1) gives:

$$\rho = \rho_0 e^{-\Omega\varepsilon} + \left(\frac{U}{\Omega}\right)\{1 - e^{-\Omega\varepsilon}\} \quad (2)$$

Here ρ_0 is the initial dislocation density at $\varepsilon = 0$. Utilizing eqn. (1) and calculating dislocation density for the steady state condition, the following relations can be derived:

$$\frac{d\rho}{d\varepsilon} = 0, \ \rho_{DRX} = \frac{U}{\Omega} \quad (3)$$

Also, the flow stress (σ) can be related to the dislocation density (ρ) as:

$$\sigma = \alpha Gb\rho^{0.5} \quad (4)$$

where α is a material constant, b is the distance between atoms in the slip direction and G is the shear modulus.

In addition, the variation of flow stress due to dynamic recovery during hot deformation is as follows:

$$\sigma^2 = [\sigma_{DRV}^2 + (\sigma_0^2 - \sigma_{DRV}^2)e^{-\Omega\varepsilon}] \qquad (\varepsilon < \varepsilon_C) \quad (5)$$

where σ is the flow stress, ε_C is the critical strain for dynamic recrystallization, ε is the total strain, σ_0 and σ_{DRV} are the yield stress and the steady state stress due to dynamic recovery, respectively. It should be noted that the above relation is applicable up to stage

II. After stage II, dynamic recrystallization mechanisms are effective as well. Stress σ_{DRV} could be attributable to dynamic recovery alone and corresponding to $\frac{d\sigma}{d\varepsilon} = 0$.

5.1.2. Constitutive equations for Stage II through Stage IV

Dynamic recrystallization typically occurs at high temperatures and low strain rates. After the onset of nucleation, the evolution of the dislocation density depends on the kinetics of dynamic recrystallization. The kinetics of dynamic recrystallization can be described by Avrami's equation [139].

$$X_D = 1 - \exp[-K\left(\frac{\varepsilon-\varepsilon_C}{\varepsilon_P}\right)^{n_d}] \qquad (\varepsilon \geq \varepsilon_C) \qquad (6)$$

where K and n_d are dynamic recrystallization parameters depending on chemical composition and hot deformation conditions [140] and ε_P is the strain corresponding to the peak stress. To determine the progress of dynamic recrystallization, the following expression is employed [141,142]:

$$X_D = \frac{\sigma_{DRV}-\sigma}{\sigma_P-\sigma_{DRX}} \qquad (7)$$

where X_D is the fraction of dynamic recrystallization. Also, σ_{DRX} and σ_P are the steady state flow stress due to dynamic recrystallization and peak stress, respectively. From eqn. (7), the amount of DRX can be obtained by means of the flow stress curves under different deformation conditions. Substituting eqn. (6) into eqn. (7) gives:

$$\sigma = \sigma_{DRV} - (\sigma_P - \sigma_{DRX})\{1 - \exp\left[-K\left(\frac{\varepsilon-\varepsilon_C}{\varepsilon_P}\right)^{n_d}\right]\} \qquad (\varepsilon \geq \varepsilon_C) \qquad (8)$$

5.1.3. Application of the model in severely deformed CP titanium

Following the methodology outlined in [111,137], the coefficient of dynamic recovery, Ω, can be obtained as a function of the Zener-Hollomon parameter (Z) to yield the below relation.

$$\Omega = 96.47\ Z^{-0.042} \quad (9)$$

Similarly, the dynamic recrystallization parameters K and n_d can be calculated for the different deformation conditions and the below relation can be obtained. n_d for the tested materials seems to approach a constant and equals to 1.6 [111,137,143].

$$K = 1.03\ \times 10^{-3}\ Z^{0.214} \quad (10)$$

The flow stress-strain response of severely deformed CP titanium at high temperatures can be predicted by applying Ω and K in Equations (5) and (8). Fig. 5.2 demonstrates that the model employed here provides decent description of the plastic region of stress-strain curves in the examined range of strain rates and temperatures.

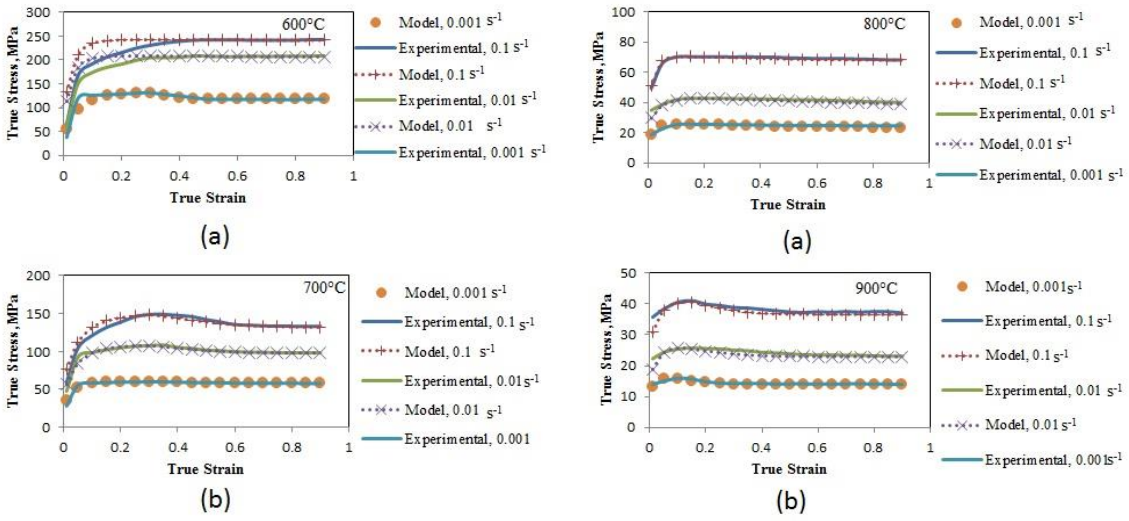

Figure 5.2 Comparison of the model predictions with experimental results at (a) 600, (b) 700, (c) 800, (d) 900°C

In order to evaluate the accuracy of the constitutive modeling, the error values between the predicted stress (σ_M) and experimental stress (σ_E) were also obtained as:

$$E\ (\%) = \frac{\sigma_M - \sigma_E}{\sigma_E} \times 100 \quad (11)$$

The highest error is less than 5% in all cases except at a temperature of 600°C and a strain rate of $0.1s^{-1}$. Moreover, this methodology is expected to be applicable for predicting flow stress curves for deformation conditions outside the experimental window as well. Since the deformation conditions bring in the equation through the Z parameter, the flow stress behavior can be predicted in the entire domain where the apparent activation energy for hot working is similar.

5.2. Prediction of Flow Stress by Arrhenius Modeling

Constitutive equations proposed by Zener and Hollomon have been used to describe the deformation behavior at high temperatures. In hot working processes, several constitutive equations have commonly been applied [15,83,129,130,144,145]:

$$Z = \dot{\varepsilon} \exp\left(\frac{Q}{RT}\right) = AF(\sigma) \quad (12)$$

Therefore:

$$\dot{\varepsilon} = AF(\sigma)\exp(\frac{-Q}{RT}) \quad (13)$$

where Z is the Zener-Holloman parameter, $\dot{\varepsilon}$ is the strain rate, Q is the apparent activation energy for hot deformation, R is the universal gas constant and T is the absolute temperature. $F(\sigma)$ is a function of flow stress which can be described as follows:

$F(\sigma) = A_1\sigma^n$ For low stress, (14)

$F(\sigma) = A_2\exp(\beta\sigma)$ For high stress, (15)

where A, α and n are material constants. Substituting the function of flow stress $F(\sigma)$ into Eqn. (13) gives:

$$\dot{\varepsilon} = B\exp(\beta\sigma)\exp(\frac{-Q}{RT}) \quad \text{For high stress,} \quad (16)$$

$$\dot{\varepsilon} = C(\sigma^n)\exp(\frac{-Q}{RT}) \quad \text{For low stress,} \quad (17)$$

Here B and C are the material constants, taking the logarithm of eqn. (16) and (17), gives:

$$(\frac{\partial \ln(\dot{\varepsilon})}{\partial \ln(\sigma_p)})_T = n \quad (18)$$

$$(\frac{\partial \ln(\dot{\varepsilon})}{\partial \sigma_p})_T = \beta \quad (19)$$

n and β are independent of deformation temperatures, and are related to each other by:

$$\alpha = \frac{\beta}{n} \quad (20)$$

The values of n and β can be obtained from the slope of the curves plotted according to Eqn. (18) and (19), respectively.

For the given strain rate conditions:

$$Q = Rn(\frac{d\{\ln[\sinh(\alpha\sigma_p)]\}}{d(\frac{1}{T})})_{\dot{\varepsilon}} \quad (21)$$

$$Q = nRS \quad (22)$$

where S is defined as $(\frac{d\{\ln[\sinh(\alpha\sigma_p)]\}}{d(\frac{1}{T})})_{\dot{\varepsilon}}$. Similarly, the value of Q can be derived from the $\ln\dot{\varepsilon}$–$\ln[\sinh(\alpha\sigma_p)]$ and $\ln[\sinh(\alpha\sigma_p)]$-1/T plots. The flow stress can be written as a function of Zener–Hollomon parameter, considering the definition of the hyperbolic law:

$$\sigma = \frac{1}{\alpha} Ln \{(\frac{Z}{A})^{1/n} + \left[\left(\frac{Z}{A}\right)^{2/n} + 1\right]^{\frac{1}{2}}\} \quad (23)$$

$$Z = \dot{\varepsilon} \exp\left(\frac{Q}{RT}\right) = A[\sinh(\alpha\sigma)]^n \quad (24)$$

The values of material constants (A, α and n) and the apparent activation energy for hot deformation (Q) of the constitutive equations were computed for 0.05 incremental strain levels within the range of 0.05 to 0.9. For this purpose, the least squares method was utilized. The variations of these constants with true strain can be represented by polynomial functions of strain. For the sake of brevity, only the plot pertaining to Q is shown in Fig. 5.3.

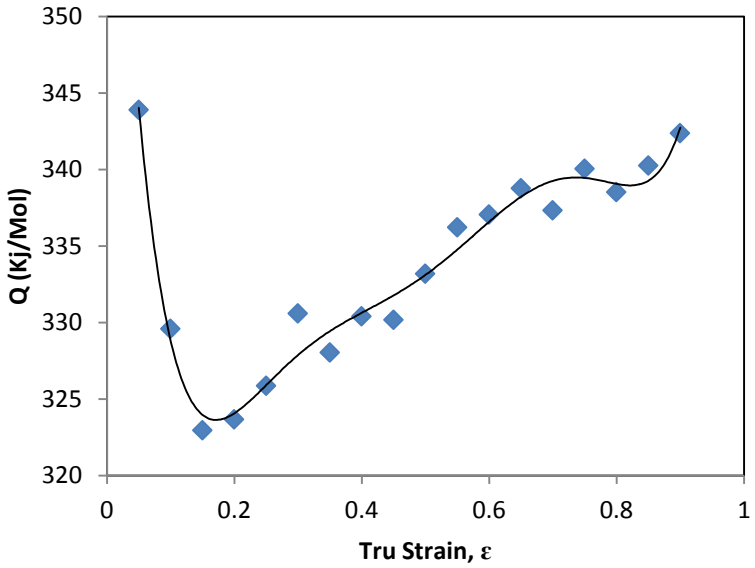

Figure 5.3 Relationships between Q and true strain by polynomial fit of UFG pure Ti

The activation energy ranges between 323 to 344 kJ/mol. Since Q represents the energy for deformation, higher Q would indicate the requirement for higher energy to activate relevant deformation mechanisms. The Q value for coarse grained pure Ti was reported as 218 to 240 kJ/mol, which is considerably lower than that observed in the present work [15]. ECAE processing increased the amount of activation energy to sustain

post hot deformation. At the beginning of the deformation, the activation energy sharply decreases with increasing strain and then increase followed by a dip around 0.2 true strain. The polynomial fitting results of n, α, Q and ln(A) for the present material are shown below and summarized in Table 5.1.

$$\alpha = B_0 + B_1\varepsilon + B_2\varepsilon^2 + B_3\varepsilon^3 + B_4\varepsilon^4 + B_5\varepsilon^5 + B_6\varepsilon^6$$

$$Q = C_0 + C_1\varepsilon + C_2\varepsilon^2 + C_3\varepsilon^3 + C_4\varepsilon^4 + C_5\varepsilon^5 + C_6\varepsilon^6$$

$$lnA = D_0 + D_1\varepsilon + D_2\varepsilon^2 + D_3\varepsilon^3 + D_4\varepsilon^4 + D_5\varepsilon^5 + D_6\varepsilon^6$$

$$n = E_0 + E_1\varepsilon + E_2\varepsilon^2 + E_3\varepsilon^3 + E_4\varepsilon^4 + E_5\varepsilon^5 + E_6\varepsilon^6 \quad (25)$$

Table 5.1 Polynomial fitting results for n, α, Q and ln A

α	Q	ln(A)	N
$B_0 = 0.017$	$C_0 = 378145.520$	$D_0 = 33.547$	$E_0 = 5.428$
$B_1 =$ -0.001	$C_1 =$ -946360.310	$D_1 =$ -7.914	$E_1 =$ -21.653
$B_2 = 0.020$	$C_2 = 6168607.150$	$D_2 = 20.509$	$E_2 = 99.354$
$B_3 =$0.025	$C_3 =$ -19347678.650	$D_3 = 29.633$	$E_3 =$ -268.380
$B_4 =$ -0.147	$C_4 = 32002373.400$	$D_4 =$ -91.292	$E_4 = 417.190$
$B_5 = 0.153$	$C_5 =$ -26650354.280	$D_5 = 33.085$	$E_5 =$ -337.330
$B_6 =$ -0.047	$C_6 = 8776537.410$	$D_6 =$21.472	$E_6 = 108.920$

The constants, summarized in Table 5.1, are substituted into eqns. (23), (24) and (25), to predict the flow behavior of UFG pure Ti. The stress-strain curves predicted by the model at different temperatures and strain rates are illustrated in Fig. 5.4. The Arrhenius model employed herein provides decent description of the flow response in the examined

range of strain rates and temperatures except 900°C. It is worth noting that the typical peak stress behavior induced by the interplay of dynamic recovery and recrystallization can be successfully captured in the predicted stress-strain curves. For the experiment at 900°C, apart from a slight undershoot of the flow stress level at $0.01s^{-1}$ and lack of stress plateau at $0.1s^{-1}$, the current approach can be of significant use for modeling the high temperature flow behavior of severely deformed Ti where competition between work hardening and softening is effective.

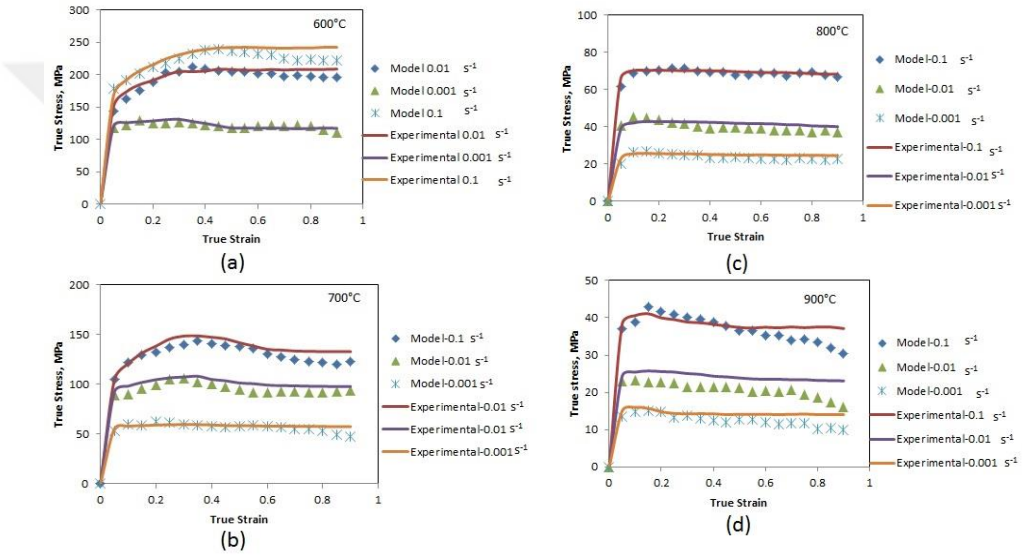

Figure 5.4 Comparison among model predictions and experimental results at: (a) 600°C, (b) 700°C, (c) 800°C, (d) 900°C

Figure 5.5 demonstrates the mean error values for the modeling approach based on Arrhenius formulation. The mean error plot reveals that simulations exhibit a better agreement at relatively lower temperatures. With increasing deformation temperature, a steady increase was observed in the error level. It was seen that the highest error level is less than 7% in all cases except at a temperature of 900°C and strain rates of 0.01 and $0.001s^{-1}$. Iterations in this work revealed that polynomial fitting up to a minimum of sixth power was required to achieve the current error levels. The major reason for higher

discrepancy in the highest temperature can be attributed to the relatively lower stress levels which magnifies the error levels. Moreover, this model does not account for softening mechanisms such as recovery or recrystallization. Furthermore, performance of the present model was compared with a similar Arrhenius type polynomial model up to fourth power for annealed pure Ti in a separate study [15]. In line with the current results, error levels increased with higher forming temperatures for annealed pure Ti as well. However, the error values shown here are noticeably less and hence improve our confidence in the proposed polynomial model for accurate flow behavior estimation of UFG titanium in the warm to hot working regime.

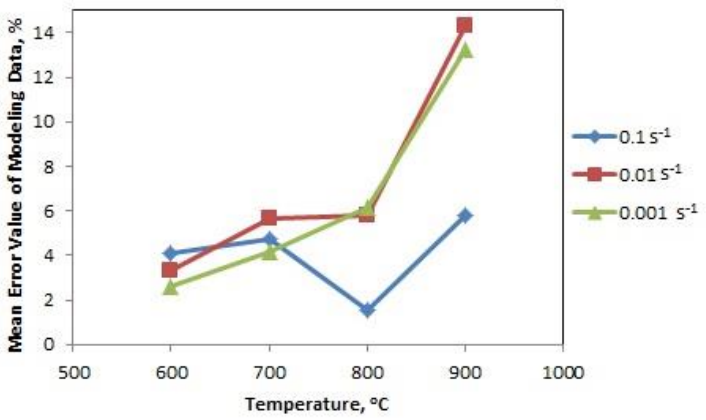

Figure 5.5 Mean error of model versus deformation conditions

5.3. Constitutive Equation for the Modified Johnson-Cook Model

In order to get a better understanding of the modeling response of severely deformed titanium, not only Arrhenius and Avrami models but also Johnson-Cook model was chosen to investigate modeling behavior of this material in this dissertation more effectively. Flow stress during hot deformation is dependent on strain (ε), strain rate ($\dot{\varepsilon}$), and temperature (T), which can be described by the following function:

$$\sigma = f(\varepsilon, \dot{\varepsilon}, T) \quad (26)$$

The Johnson-Cook (JC) and its modified models are utilized in different materials to predict their flow stress behavior at elevated temperature [146]. The modified JC equation for hot compression is as follows [147,148]:

$$\sigma = \left(\sigma_P + B(T)\varepsilon^{n(T)}\right)[1 + C(\varepsilon, T)\ln(\frac{\dot{\varepsilon}}{\dot{\varepsilon}_0})] \quad (27)$$

B(T) and n(T) are material constants, which are dependent on deformation temperature. C(ε,T) is the material constant that is a function of both deformation temperature and strain. $\dot{\varepsilon}$ is the reference strain rate. The lowest strain rate ($0.001s^{-1}$) is selected as the reference strain rate [147].

5.3.1. Calculation of B(T), n(T) and C(ε,T)

For the strain rate ($\dot{\varepsilon}$) of $0.001s^{-1}$, Equation (27) can be written as:

$$\sigma = \left(\sigma_P + B(T)\varepsilon^{n(T)}\right) \quad (28)$$

Where σ_P is the peak stress. Taking the logarithm of Equation (28), gives:

$$\ln(\sigma_P - \sigma) = \ln[-\mathrm{B(T)}] + n(T)\ln(\varepsilon) \quad (29)$$

The values of n and B can be obtained from Equation (29), according to the slope and intercept of the lines (Fig. 5.6), respectively. The linear relationship was seen to be better at higher deformation temperatures in comparison with that of lower temperatures. This could be attributed to the stability of the UFG structure at lower deformation temperatures bringing higher discrepancy at 600 °C and 700 °C. The values of n and B are presented in Table 5.2.

Table 5.2 The values of B and n under different temperatures and at a strain rate of $0.001s^{-1}$

Material Constants	600°C	700°C	800°C	900°C
B(T), MPa	-60.099	-11.806	-1.696	-1.995
n(T)	4.311	3.251	1.319	0.123

With the substitution of n(T) and B(T) into Equation (2), respective values of C(ε,T) can be calculated under various deformation conditions. The values of C(ε,T) versus strain for different deformation conditions are obtained by linear fitting (Fig. 5.7). As presented in Table 5.3 for selected true strain levels. For the sake of brevity, figures demonstrating the relation for the other deformation temperatures are not presented here.

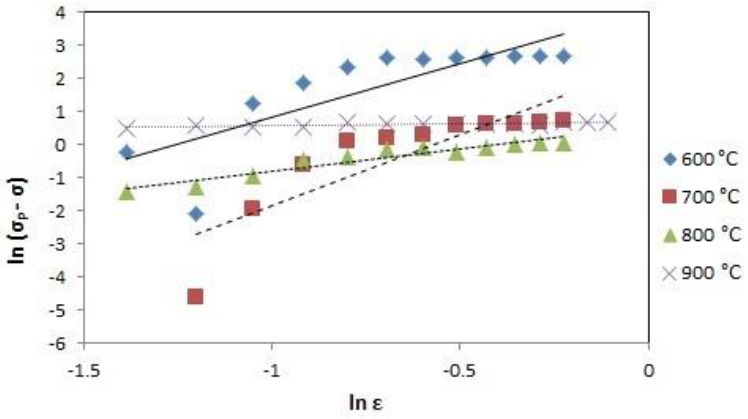

Figure 5.6 Relationship between $\ln(\sigma_P - \sigma)$ and $\ln(\varepsilon)$ at various temperatures and at a strain rate of $0.001s^{-1}$

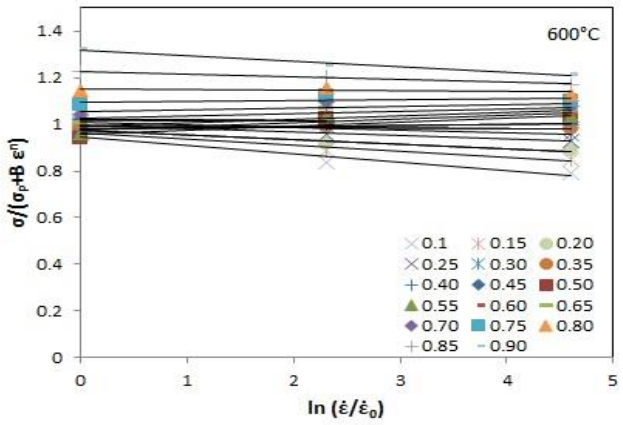

Figure 5.7 Relationship between $\frac{\sigma}{[\sigma_P + B(T)\varepsilon^{n(T)}]}$ and $\ln(\frac{\dot{\varepsilon}}{\dot{\varepsilon}_0})$

Table 5.3 The values of C at different deformation strain levels and temperatures

Strain	600°C	700°C	800°C	900°C
0.20	-0.0201	-0.013	0,0005	-0.013
0.40	0.0055	-0.0005	0.0016	-0.0005
0.60	0.015	-0.0162	-0.0019	-0.0162
0.80	-0.0029	-0.0265	-0.0035	-0.0265

5.3.2. Prediction of Flow Stress by the Modified Johnson-Cook Modeling

The flow stress behavior of ECAE processed pure Ti can be predicted by applying B(T), n(T) and C(ε,T) to Equation (27), as demonstrated in Fig. 5.8. This model is precise in predicting the flow stress at all deformation conditions except at a temperature of 600 °C. At lower deformation temperatures and higher deformation rates, the severely deformed microstructure is partly retained, and as such, the model may lose its accuracy in determining the actual softening behavior.

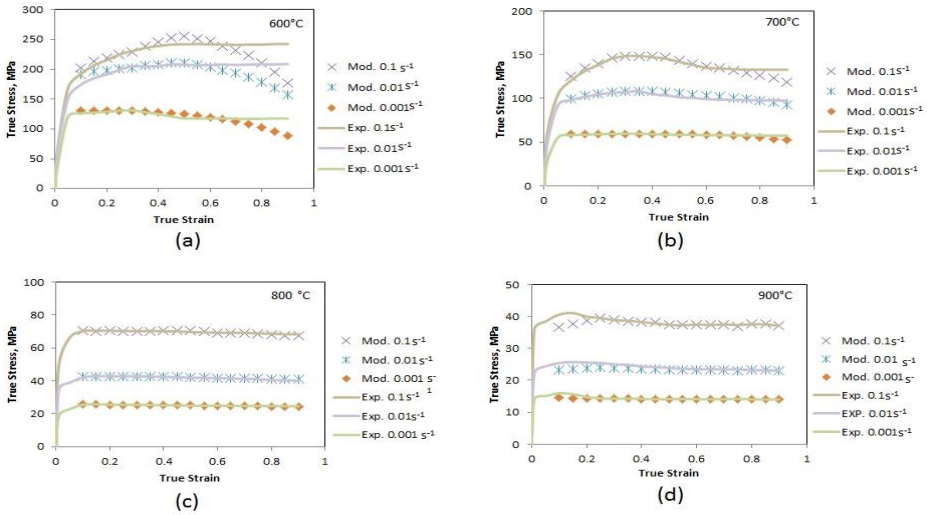

Figure 5.8 Comparison among model predictions and experimental results at: (a) 600°C, (b) 700°C, (c) 800°C, (d) 900°C

Furthermore, it is worth noting that the difference between the simulated and experimental data is higher with increasing strain at 600 °C. Here, the modeled flow stress curves generally reach a peak and then decrease sharply, which is a pronounced characteristic of dynamic recrystallization. However, few experimental flow stress curves feature a peak followed by an immediate plateau. This is a well-known behavior of dynamic recovery and can be observed at the lowest deformation temperature.

5.3.3. Extension of the Johnson-Cook Model for Prediction of ECAE Processed Ti with a Corrective Term

When modeling the deformation at 600 °C, there is a considerable discrepancy between the experimental and model flow responses especially after the peak stress. The variation of the material constants, n(T) and B(T), as a function of temperature is plotted in Fig. 5.9 exhibiting strong dependence on the deformation temperature. It is worth noting that n(T) increases with decrease of deformation temperature. Moreover, it was seen that the absolute value of B(T) shows a considerable increase with decrease of deformation temperature. However, at higher temperatures, B(T) is fairly constant and can be considered to be independent of temperature. With the increase of deformation temperature, a similar behavior for B(T) and n(T) was reported for modeling the high temperature behavior of an aluminum alloy [147].

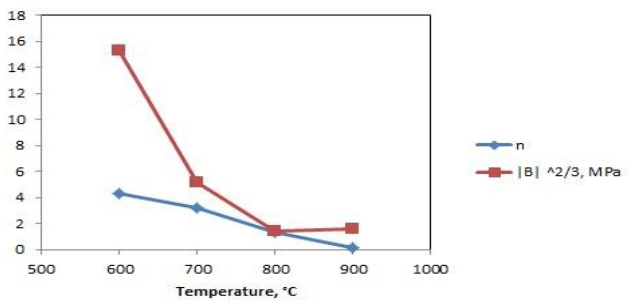

Figure 5.9 Deformation temperature versus n and $|B|^{2/3}$

Another important factor affecting the predictions of this model is the amount of true strain. As can be observed in Fig.5.8a, agreement of the model with the experimental data gets worse from peak strain up to a true strain of 0.9. Considering that the error levels are comparably larger for deformation at 600 °C, a new term accounting for this behavior is added to Equation (27). This corrective term can be formulated as [148]:

$$Corrective\ Term = \frac{(n(T)+\varepsilon).(\sigma_P.\varepsilon^{n(T)})}{|B(T)|^{\frac{2}{3}}} \quad (30)$$

The corrective term depends on the degree of deformation temperature via the inclusion of the material constants, n(T) and B(T). With the dependence of corrective term on true strain, flow stress levels are expected to remain constant and a plateau behavior can be obtained. The modified flow response prediction at the lowest deformation temperature of 600 °C is shown in Fig. 5.10 demonstrating better agreement with the experimental curve.

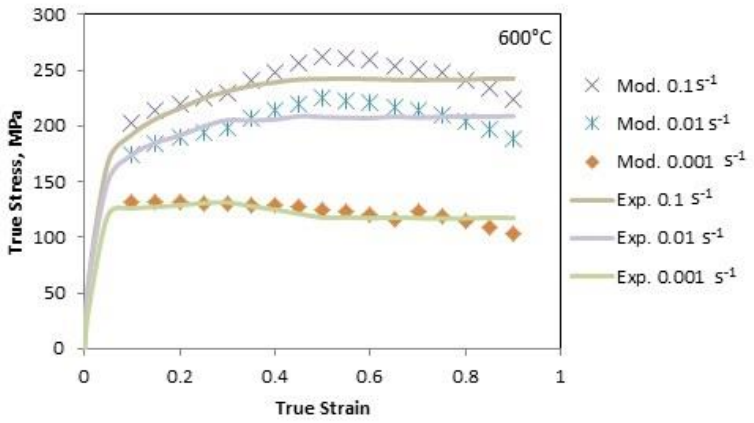

Figure 5.10 Comparison between improved model predictions and experimental results at 600°C

5.3.4. Verification of the Model

Fig. 5.11 demonstrates the mean error values for the modeling approach based on the modified JC equation. It can be seen that the highest error level is less than 5% in all

cases indicating reasonable agreement. In a separate study, models based on Arrhenius and dislocation density based formulations were employed for modeling the behavior of ECAE processed Ti in the warm to hot working regime. It can be seen that the error levels obtained using the current model is comparably less than those reported in section 5.1 and 5.2 of this chapter.

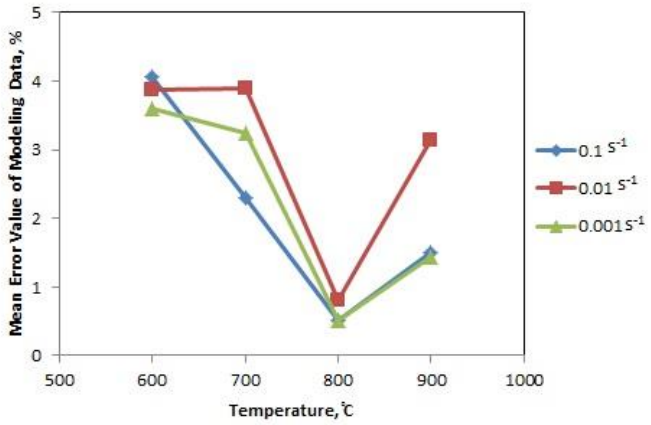

Figure 5.11 Mean error of the model for various deformation conditions

Although both the modified JC and dislocation density based models exhibit decent predictive capability at relatively higher temperatures, their accuracy depends on how the active softening mechanisms are treated according to the deformation temperature. Another assumption of these constitutive models is that, they typically consider coarse grained microstructures. However, it was mentioned that the average grain size of UFG titanium remained less than 3.5 µm at 600°C [149]. This finding was also confirmed in a different study [8-10]. On the other hand, the microstructure of ECAE processed Ti followed by hot compression tests (above 700 °C) contained grains with average size over 15 µm (See Chapter 4). Therefore, the relatively fine grain size at lower temperatures could lead to the higher error levels observed in the prediction of the flow response at 600 °C.

6. Effect of Purity Levels on the High Temperature Deformation Characteristics of Severely Deformed Titanium

In the present chapter, high temperature compression tests were conducted at strain rates of $0.001s^{-1}$-$0.1s^{-1}$ and at temperatures of $600^{o}C$-$900^{o}C$ in order to study the hot deformation characteristics and dynamic softening mechanisms of two different grades of commercial purity titanium after severe plastic deformation.

6.1. Microstructural Evolution

The optical micrographs for two grades of CP titanium in different processing states are demonstrated in Fig. 6.1. The grain size measurements based on the linear intercept method are also summarized in Table 6.1. It is worth noting that 8 passes ECAE processing instigated a significant refinement in both grades as compared with the initial coarse structures (Fig 6.1a and 6.1b). All micrographs of ECAE samples were recorded from the flow planes. Optical micrographs of ECAE grade 2 and 4 followed by heat treatment at 600°C and at 900°C are also represented in Fig. 6.1c-f. 3 minutes annealing period is selected based on the time it takes to achieve uniform heating of the samples at the desired compression test temperature. After the 600°C heat treatment for 3 and 30 minutes, the microstructure consists of both slightly coarsened grains and regions with ultrafine grains (Fig. 6.1c and d). However, it can be observed that a severe grain growth took place in both grades at 900°C (Fig. 6.1e). The 900°C heat treatment for 3 minutes resulted in the growth of statically recrystallized grains with an average grain size of 25µm and 16µm in grade 2 and 4, respectively. Although keeping specimens at 900°C for longer time periods led to a coarser structure (Fig. 6.1f), the grain growth rate considerably decreases. The drop of grain growth rate could be related to the depletion of driving

energy due to saturation of the microstructure. To reveal the effect of post SPD deformation, microstructures of UFG grade 2 and 4 Ti followed by hot deformation at 600°C-0.001s^{-1} and 900°C-0.001s^{-1} are shown in the Fig. 6.1g and h, respectively. After hot compression test at 600°C at the lowest deformation rate, microstructure of grade 2 still consists of some regions with ultrafine grains. In contrast, grade 4 has the structure with moderately coarsened grains. The sample subjected to compression at 900°C exhibits microstructure with considerably large grains in comparison with those of the compressed at 600°C. The existence of equiaxed grains is mostly apparent for this deformation temperature and could be distinguished as dynamically recrystallized structures.

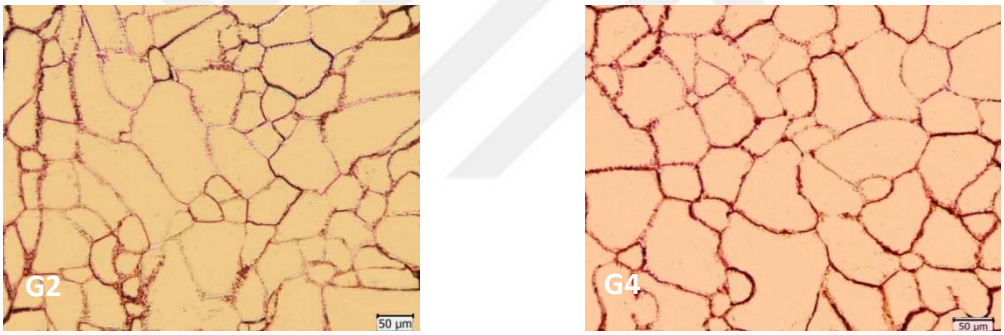

(a)

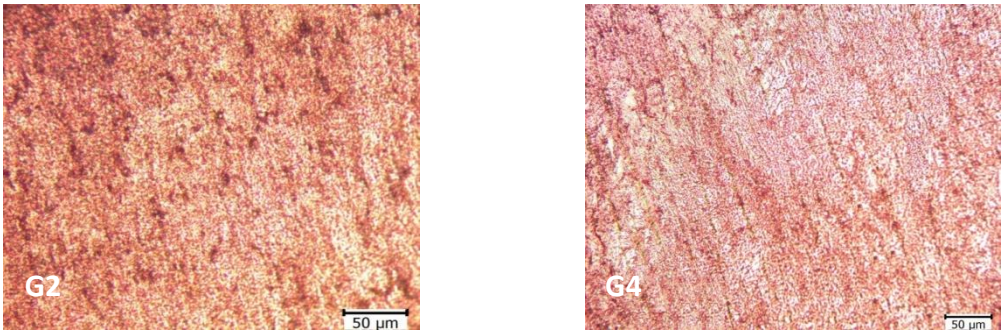

(b)

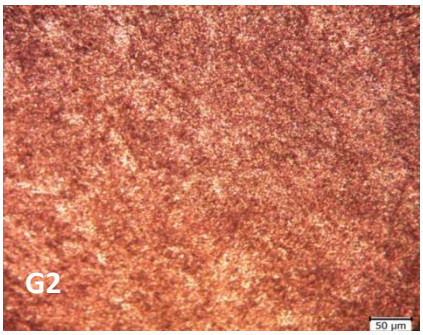

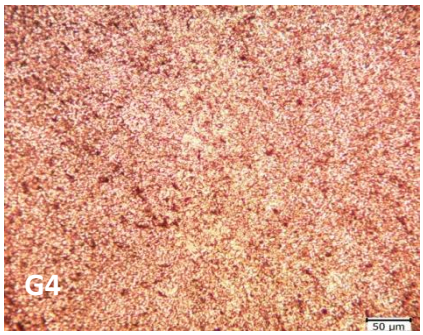

(c)

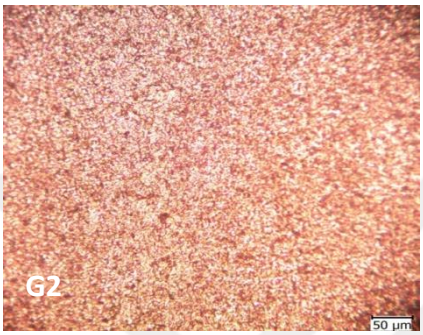

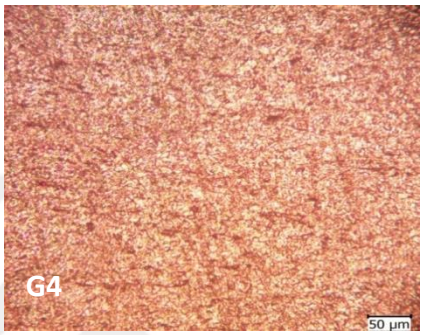

(d)

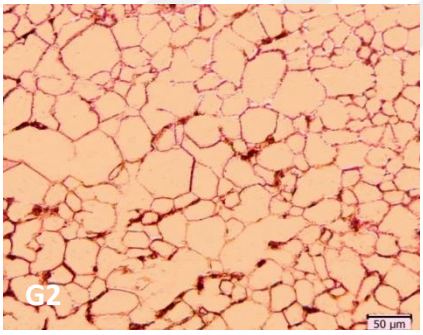

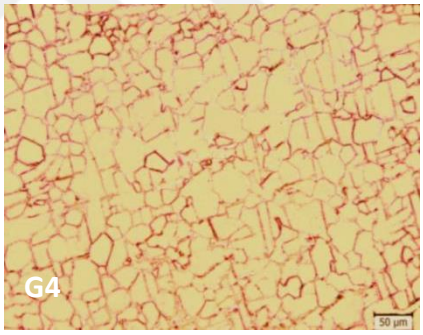

(e)

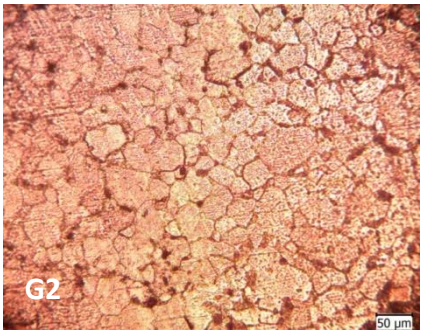

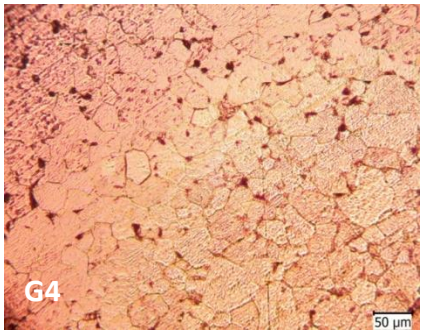

(f)

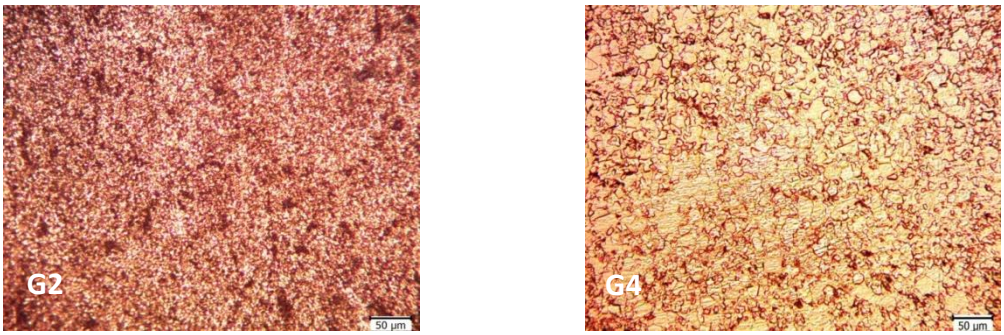

(g)

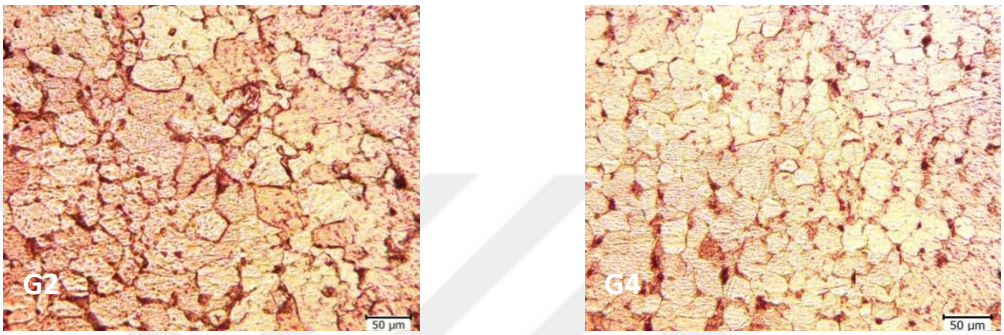

(h)

Figure 6.1 The microstructure of grade 2 and 4 CP Ti in a) as-received condition, b) ECAE processed, c) ECAE processed followed by 3 minutes of annealing at 600°C, d) ECAE processed followed by 30 minutes of annealing at 600°C, e) ECAE processed followed by 3 minutes of annealing at 900°C, f) ECAE processed followed by 30 minutes of annealing at 900°C, g) ECAE processed followed by compression at 600°C with a strain rate of $0.001s^{-1}$, h) ECAE processed followed by compression at 900°C with a strain rate of $0.001s^{-1}$

Table 6.1 Grain size of severely deformed titanium, before and after hot compression

Condition	Average Grain Size (μm)	
	Grade 2 Ti	**Grade 4 Ti**
As-Received	43	46
After 8 passes ECAE processing	0.3	0.3
After 8 passes of ECAE followed by 3 minutes of annealing at 600°C	1.9	2.4
After 8 passes of ECAE followed by 30 minutes of annealing at 600°C	3.7	4.1
After 8 passes of ECAE followed by 3 minutes of annealing at 900°C	25	16
After 8 passes of ECAE followed by 30 minutes of annealing at 900°C	30	26
After 8 passes of ECAE followed by compression at 600°C and $0.001s^{-1}$	8	12
After 8 passes of ECAE followed by compression at 900°C and $0.001s^{-1}$	29	24

Optical micrographs of ECAE processed grade 2 and grade 4 titanium followed by hot compression at 700°C and 800°C are presented in Fig. 6.2. Serrations of grain boundaries are observed and it can be seen that some new grains formed in the vicinity of former grain boundaries. Examples of such grains are highlighted by blue arrows in Fig. 6.2, for both grades.

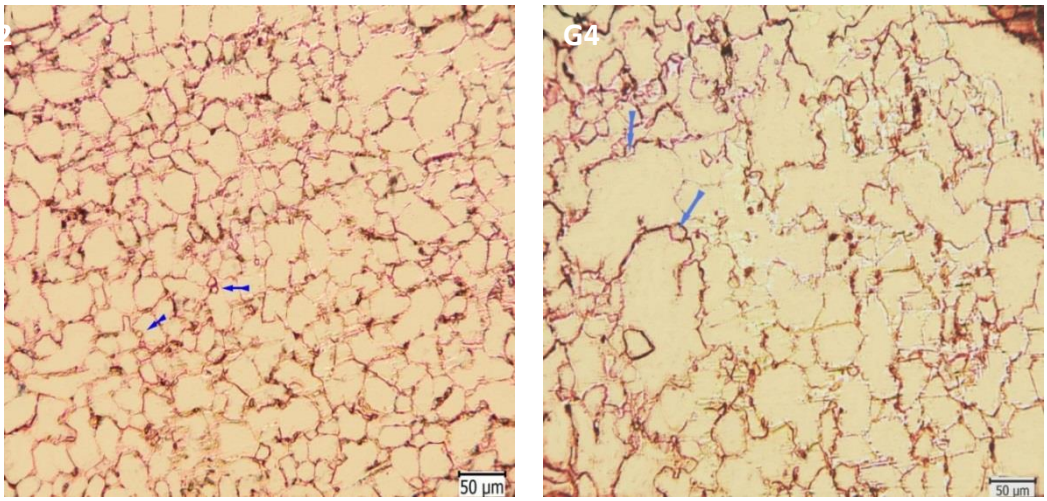

(a) (b)

Figure 6.2 Microstructure of ECAE processed titanium followed by hot compression (a) grade 2 at 700°C and 0.001s^{-1}, (b) grade 4 at 800°C and 0.001s^{-1}. The arrows indicate the nucleation of dynamically recrystallized grains at the original grain boundaries

The microstructural observations can also be traced by SEM micrographs in Fig. 6.3 especially for the case of 600°C heat treated sample due to its fairly fine structure. Similar to optical micrographs (Fig. 6.1b), it can be seen that 8 passes ECAE provides both grades with a significant refinement (Fig. 6.3a). As such, the microstructures from both grades do not reveal highly contrasting features, and contain ultrafine grains. These observations are in line with our previous work where the grain sizes of both grades were found to be around 300 nm. In the same study, comparative microstructural examinations showed relatively small dislocation density and a more recrystallized structure in grade 4 Ti. Therefore, the fraction of high angle grain boundaries (HAGB) in severely deformed grade 2 Ti can be expected to be larger. In Fig. 6.3b, grain coarsening which was hardly detected in Fig. 6.1c is evident after 3 minutes annealing at 600°C. Annealing at this temperature led to an average grain size of 1.9 and 2.4 microns for grade 2 and 4, respectively (Fig. 6.3b). It is also worth noting that at this temperature,

grade 2 CP Ti microstructure after 8 passes of ECAE is more stable than that observed in grade 4.

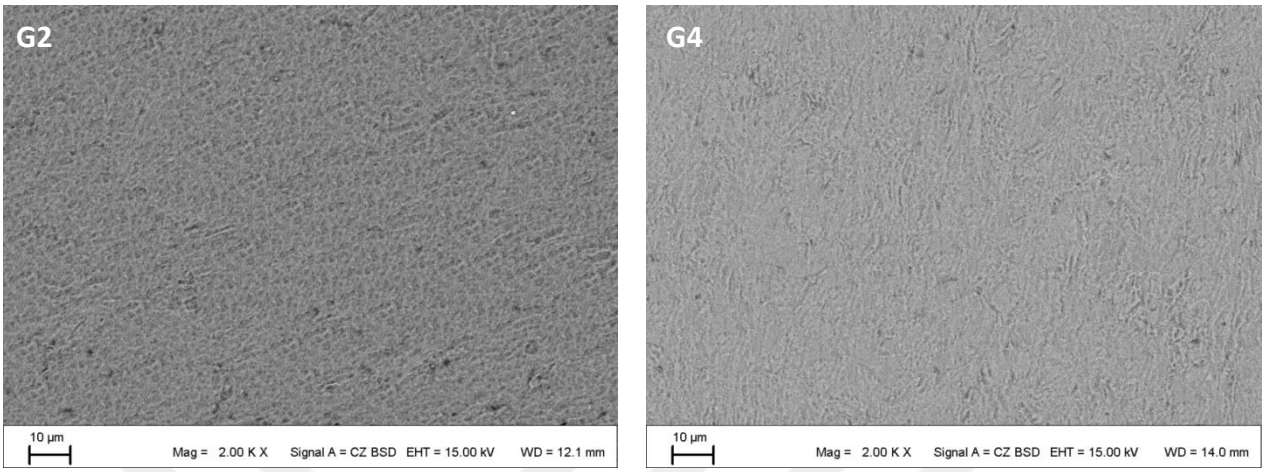

(a)

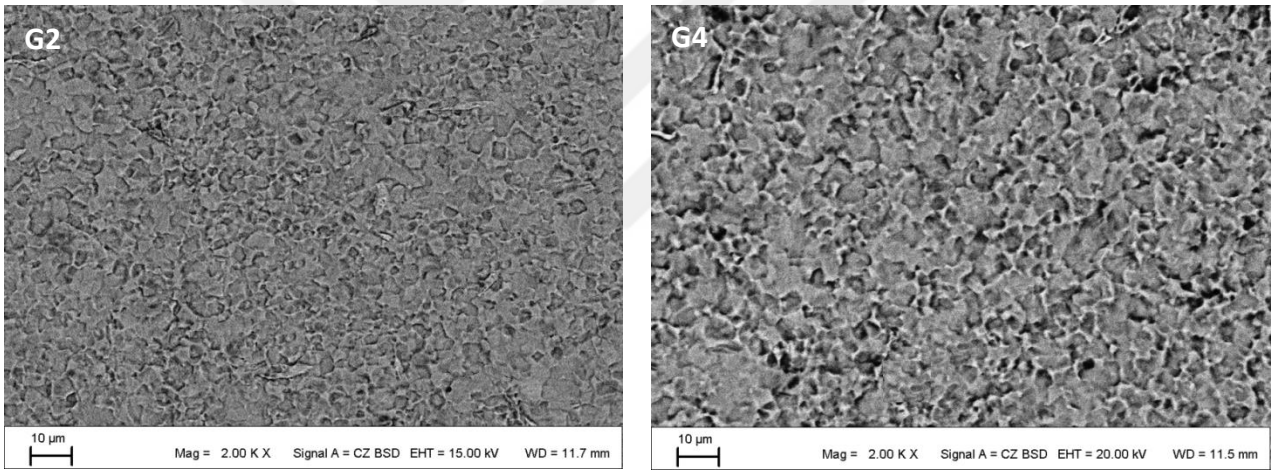

(b)

Figure 6.3 SEM images of grade 2 and 4 CP Ti on the flow plane after (a) 8 passes ECAE (b) 8 passes ECAE followed by heat treatment at 873K (600^{o}C) for 3 minutes

6.2. Mechanical Behavior

Fig. 6.4 and 6.5 represent the true stress-true strain curves for the compression tests of severely deformed CP grade 2 and 4 titanium at various temperatures for the strain rates of 0.001s^{-1}, 0.01s^{-1} and 0.1s^{-1}. It can be seen that the flow stress of both grades is sensitive to both deformation rate and temperature. Flow stress levels of both

grades sharply drop with increase of deformation temperature or decrease of strain rate. At 600^{o}C, grade 2 Ti demonstrated higher flow stress levels for all strain rates. However, grade 4 Ti showed higher levels of stress at the deformation temperatures of 800^{o}C and 900^{o}C. Deforming metallic materials at elevated temperatures can lead to the occurrence of softening during deformation. In a previous study, it was mentioned that DRX process and the dynamically recrystallized grain size depends only on the strain rate and temperature [99,150]. In essence, the Zener-Holloman (Z) parameter, utilized to describe the effects of temperature and strain rate on deformation characteristics of metals, affects the DRX process and the recrystallized grain size [151]. At higher deformation temperatures, there is significant thermal energy to promote nucleation and rapid growth of dynamically recrystallized grains [151]. In the present study, lower flow stress levels and coarser structure for both grades were also obvious at higher deformation temperatures. Similar tendency to rapid grain growth was reported for CG titanium deformed in the range of 600^{o}C-800^{o}C [13].

Another important effect which dramatically influences the Z parameter is the strain rate. It is well known that DRX process might be less obvious at higher deformation rates since samples deformed at high rates do have shorter periods to complete the onset of DRX [14]. As a result, increased strain rate hampers the DRV and DRX mechanisms, thereby accelerating the dislocation generation [152,153]. However, deforming at low deformation rates can lead to rapid grain growth having an adverse effect on the possible refinement brought about by DRX. Thus, the flow behavior is interpreted based on the subsequent evolution of the microstructure.

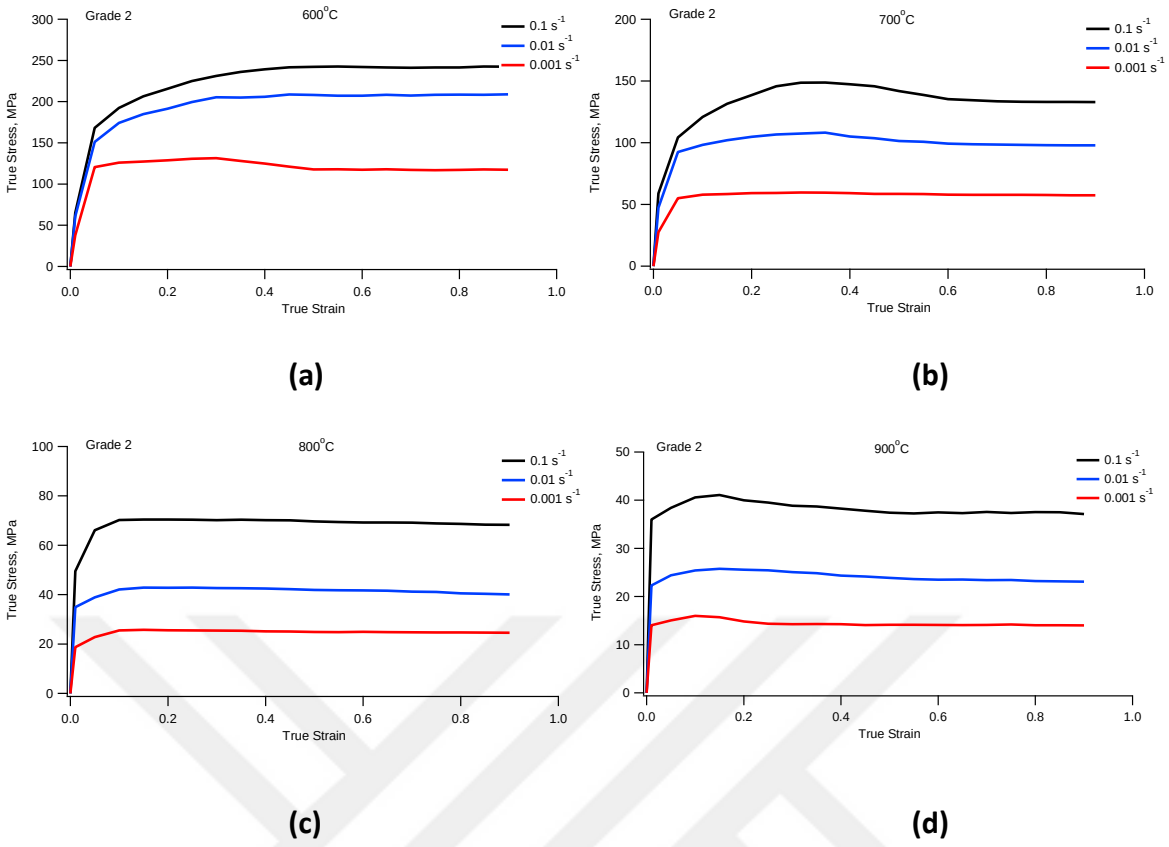

Figure 6.4 True stress-true strain response of severely deformed CP grade 2 titanium with different strain rates at (a) 600°C, (b) 700°C, (c) 800°C, and (d) 900°C

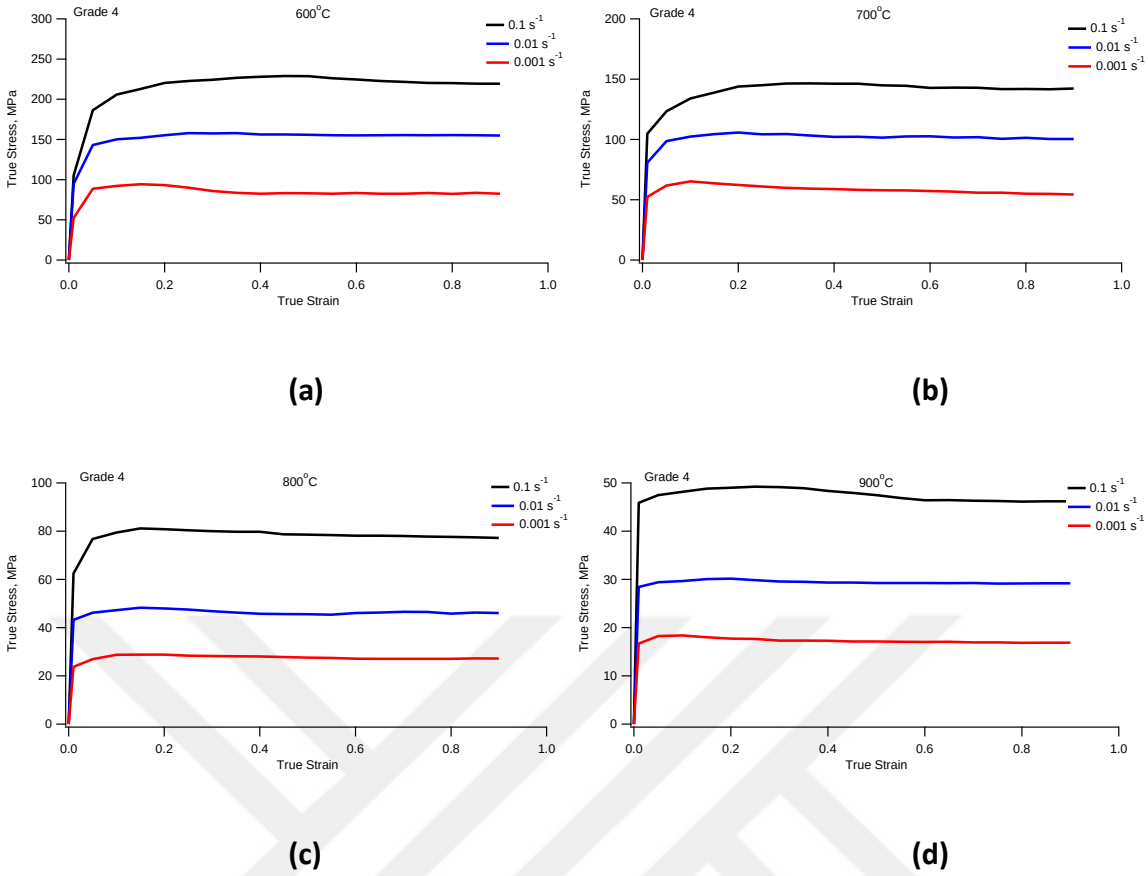

Figure 6.5 True stress-true strain response of severely deformed CP grade 4 titanium with different strain rates at (a) 600°C, (b) 700°C, (c) 800°C, and (d) 900°C

Fig. 6.6 compares the flow curves of both CP Ti grades with CG and UFG microstructures at a deformation temperature of 600°C and at a strain rate of $0.1s^{-1}$. It is worth noting that flow stress level for CG grade 4 titanium is higher than that of grade 2 (Fig. 6.6a). This could be attributed to the higher content of oxygen in grade 4. It is also worth mentioning that severely deformed samples of both grades exhibit higher flow stress levels at 600°C (Fig. 6.6b and c). The difference between flow stress levels of severely deformed samples with CG counterparts is considerably larger for grade 2 titanium. Higher fraction of HAGBs obtained through processing at the lower temperature (300°C for grade 2 versus 450°C for grade 4) could be a potential reason for the current observation as elaborated further in the following sections.

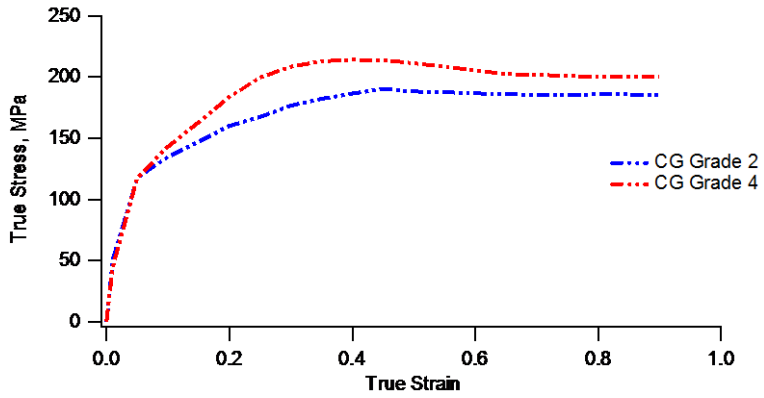

(a)

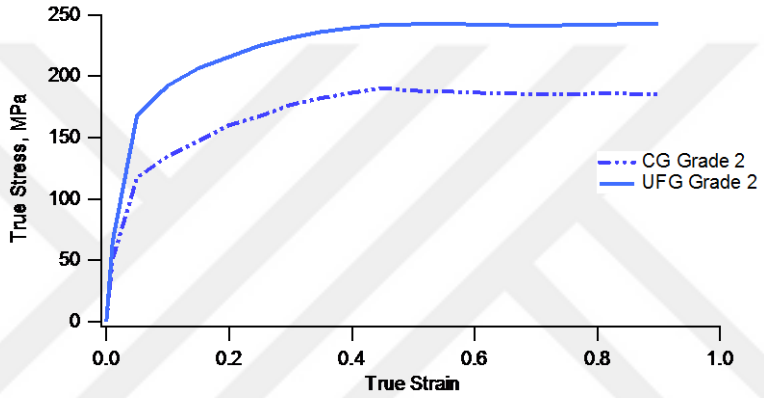

(b)

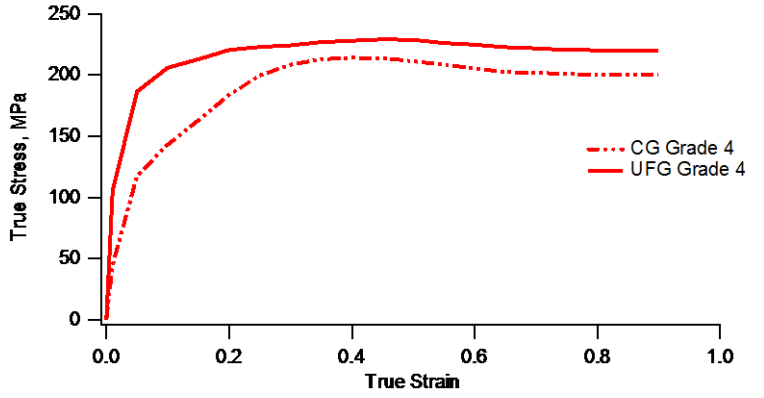

(c)

Figure 6.6 True stress- true strain response of grade 2 and grade 4 titanium at 600^{o}C-0.1s^{-1}, (a) grade 2 and grade 4 CG titanium, (b) grade 2 CG and UFG titanium and (c) grade 4 CG and UFG titanium

6.3. Strain Rate Sensitivity

Strain rate sensitivity is an important factor that influences formability of materials and can be considered as an indication of workability. It displays the effect of strain rate on dislocation generation and propagation and can be calculated by employing the following well-known relation.

$$m = \frac{\partial \ln(\sigma)}{\partial \ln(\dot{\varepsilon})}\Big|_{\varepsilon} \quad (1)$$

The values of m can be obtained from the slope of the lines plotted according to Eqn. (1) at a constant strain. The variation of the strain rate sensitivity of both grades as a function of strain is plotted in Fig. 6.7 displaying strong dependence to deformation temperature, especially for grade 2 Ti. On the other hand, the strain rate sensitivity of grade 4 shows somewhat less dependence to temperature especially above a true strain level of 0.4. Moreover, m values of grade 4 are considerably higher than those of grade 2 at 600^{o}C representing the dominance of DRX for grade 4 at this deformation temperature. Considering the strain dependence of rate sensitivity of grade 4, the m values at 600°C and 700°C increase and reach a peak at a strain around 0.4 and stay almost constant with increasing strain. It can be concluded that for UFG Ti, higher strain rate sensitivity levels are observed with increasing deformation temperature as expected. However, m is not a strong function of strain at or above 800°C. In contrast, the rate sensitivity at or above 800°C do not show strong dependence to strain. This phenomenon can be attributed to the increased activity of diffusion related mechanisms and dynamic recrystallization at higher temperatures resulting in higher strain rate sensitivity [154]. The behavior for grade 2 Ti is similar albeit a noticeable gap between the 600°C and 700°C responses

below 0.4 true strain. This could be related to the higher stability of grade 2 Ti that could postpone dynamic recrystallization at lower deformation temperatures.

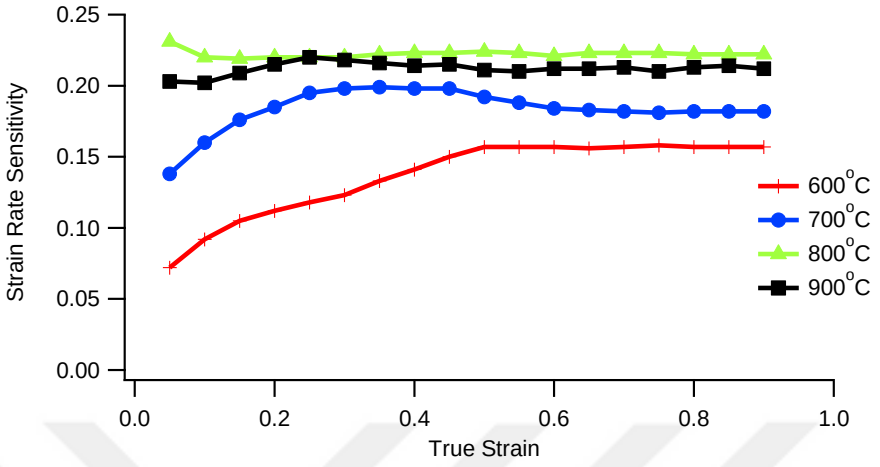

(a)

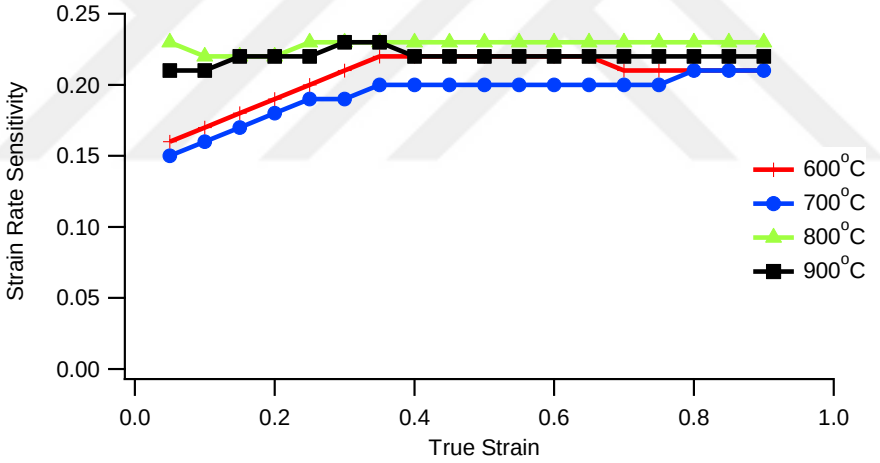

(b)

Figure 6.7 Strain dependence of strain rate sensitivity at various temperatures (a) grade 2 titanium, (b) grade 4 titanium

6.4. Activation Energy for Hot Deformation and Flow Behavior Prediction at Elevated Temperatures

In the previous chapters, activation energy calculation of hot deformation and modeling techniques were comprehensively explained. Therefore, due to the sake of brevity, only calculated values are presented in the present chapter. The values of the activation energy Q can be obtained as shown in Table 6.2. As compared to grade 4, severely deformed grade 2 titanium requires more energy for hot deformation. The highest difference in activation energy values can be observed at the lowest deformation temperature. In contrast, the lowest difference takes place at the highest deformation rate for all temperatures.

Table 6.2 Comparison of the activation energy (Q) values for severely deformed grade 2 and grade 4 titanium

Condition	SPD Grade 2 CP Ti (kJ)	SPD Grade 4 CP Ti (kJ)
873K (600°C)-0.1s^{-1}	292.7	210.6
873K (600°C)-0.01s^{-1}	322.4	210.9
873K (600°C)-0.001s^{-1}	292.5	198.5
973K (700°C)-0.1s^{-1}	272.4	263.1
973K (700°C)-0.01s^{-1}	300.1	263.6
973K (700°C)-0.001s^{-1}	272.2	248.0
1073K (800°C)-0.1s^{-1}	288.7	227.6
1073K (800°C)-0.01s^{-1}	318.0	228.0
1073K (800°C)-0.001s^{-1}	288.5	214.5
1173K (900°C)-0.1s^{-1}	311.0	244.5
1173K (900°C)-0.01s^{-1}	342.6	245.0
1173K (900°C)-0.001s^{-1}	310.8	230.5

The constitutive equations utilized herein describe the flow behavior in terms of work hardening (WH), DRV and DRX regions. As it was mentioned in the previous chapter, due to the combined effect of work hardening and thermally activated softening mechanisms, most of the flow stress curves at elevated temperatures include four stages especially at relatively low strain rates: stage I (work hardening stage), stage II (transition stage), stage III (softening stage) and stage IV (steady stage).

The fundamental flow stress relations used are:

$$\sigma^2 = [\sigma_{DRV}^2 + (\sigma_0^2 - \sigma_{DRV}^2)e^{-\Omega\varepsilon}] \qquad (\varepsilon < \varepsilon_C) \qquad (2)$$

$$\sigma = \sigma_{DRV} - (\sigma_P - \sigma_{DRX})\{1 - \exp\left[-K\left(\frac{\varepsilon-\varepsilon_C}{\varepsilon_P}\right)^{n_d}\right]\} \qquad (\varepsilon \geq \varepsilon_C) \qquad (3)$$

where σ is the flow stress, ε_C is the critical strain for DRX, ε is the total strain, σ_0 and σ_{DRV} are the yield stress, and the steady state stress due to DRV, respectively. σ_{DRX} and σ_P are the steady state flow stress due to DRX and peak stress, respectively. The coefficient of dynamic recovery, Ω, and dynamic recrystallization parameters, K and n_d, for grade 4 titanium can be determined as a function of the Zener-Holloman parameter for different deformation conditions and the below relations can be obtained following the methodology outlined in chapter 5:

$$\Omega = 114.76\, Z^{-0.057} \qquad (4)$$

$$K = 1.85 \times 10^{-2}\, Z^{0.142} \qquad (5)$$

The flow behavior of grade 4 titanium is modeled by applying the above formulas to Eqs. (2) and (3) as shown in Fig 6.8.

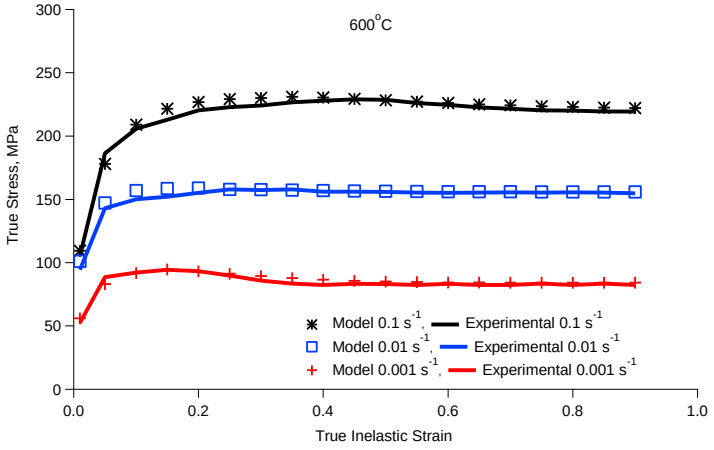
600°C
True Stress, MPa
True Inelastic Strain
Model 0.1 s-1, Experimental 0.1 s-1
Model 0.01 s-1, Experimental 0.01 s-1
Model 0.001 s-1, Experimental 0.001 s-1

(a)

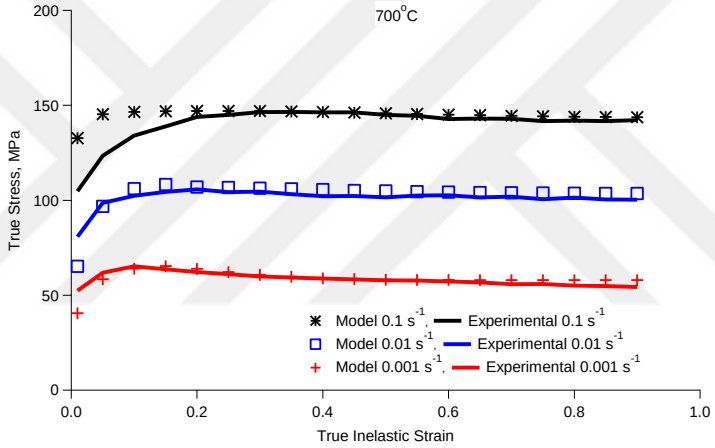
700°C
True Stress, MPa
True Inelastic Strain
Model 0.1 s-1, Experimental 0.1 s-1
Model 0.01 s-1, Experimental 0.01 s-1
Model 0.001 s-1, Experimental 0.001 s-1

(b)

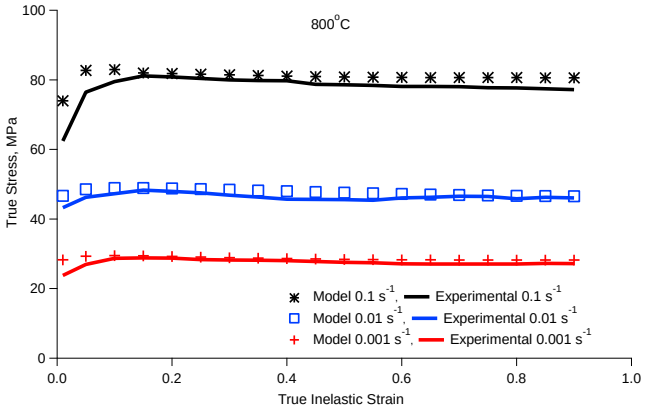
800°C
True Stress, MPa
True Inelastic Strain
Model 0.1 s-1, Experimental 0.1 s-1
Model 0.01 s-1, Experimental 0.01 s-1
Model 0.001 s-1, Experimental 0.001 s-1

(c)

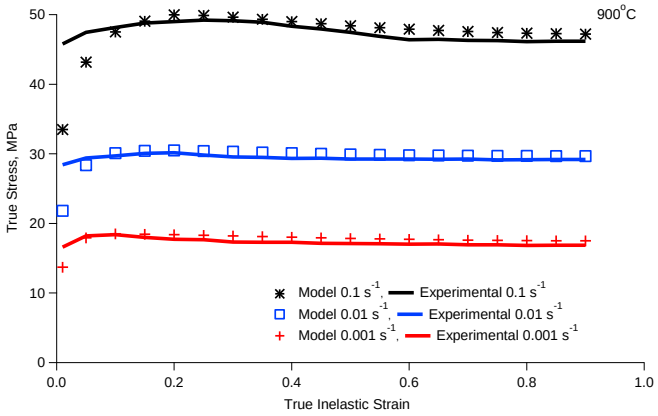

(d)

Figure 6.8 Comparison of the model predictions with experimental results of severely deformed grade 4 titanium at (a) 873K (600°C), (b) 973K (700°C), (c) 1073K (800°C), and (d) 1173K (900°C)

This model is accurate in predicting the mechanical behavior at all deformation temperatures. In order to evaluate the accuracy of the constitutive modeling, the error values between the predicted stress (σ_M) and experimental stress (σ_E) were also obtained as:

$$E\,(\%) = \frac{\sigma_M - \sigma_E}{\sigma_E} \times 100 \qquad (6)$$

As calculated per the average for the whole range of strain at each deformation condition, the highest error level is around 4.5% in all cases. It is worth noting that the model was not able to provide reasonable predictions of the flow behavior at low strain values below 0.1. The higher discrepancy can be attributed to the assumptions of the present model. Similar error levels were also obtained for the case of grade 2 Ti with the same modeling approach (See Chapter 5).

6.5. Thermal Stability of UFG Titanium

During annealing at a temperature of 600^{o}C, gradual grain growth took place in the microstructure of both grades (Fig. 6.1c and Fig. 4b), as could be attributed to the recrystallization of severely deformed grains. Similar results with the same average grain size were reported for UFG CP titanium where a normal grain growth occurred through the microstructure up to 600^{o}C [149]. Since higher temperatures bring about a remarkable driving force, deformation up to 900^{o}C was considered in order to better investigate the effect of temperature on the stability. As expected, grain size of both CP grades sharply increased at 900^{o}C in relation with the higher driving force for grain growth. Moreover, it is known that the drop of internal energy due to decrease of grain boundary fraction has strong influence on the nucleation and growth of new grains [149,153,155]. Therefore, while short durations of annealing at high temperatures can easily promote rapid grain growth, longer periods may not have apparent effects on the grain size. This can be observed in the present case when comparing Figs. 6.1e and 2f.

In analyzing the stability of UFG microstructures, the effect of processing temperature should be discussed as well. Severe plastic deformation temperature can play a significant role in dictating the level of refinement and the grain boundary character distribution (GBCD). A study on the principles of ECAE showed that the fraction of low angle grain boundaries (LAGB) increased with increasing processing temperature [34]. This was attributed to the faster recovery of grain boundaries at higher temperatures leading to an increased annihilation of dislocations within the grains and a consequent decrease in the number of dislocations absorbed into the subgrain walls. It was also revealed that the mobility of LAGBs is higher than that of HAGBs at high homologous temperatures [34].

In the previous work, formation of HAGBs was favored for grade 2 UFG Ti processed at a lower temperature than grade 4 [156]. Therefore, at an annealing temperature of 600^{o}C, higher thermal stability was observed for grade 2 UFG Ti since ECAE processing temperature was 300^{o}C and 450^{o}C for grade 2 and grade 4, respectively (Fig. 6.3b). The high temperature flow stress behavior of both grades can also confirm this statement (Fig. 6.4, 6.5 and 6.6). While the flow stress level of grade 4 Ti with coarse structure was seen to surpass that of grade 2 at 600^{o}C-0.1s^{-1}, severely deformed grade 2 Ti exhibited higher flow stress levels than grade 4 at the deformation temperatures of 600^{o}C and 700^{o}C possibly due to higher fraction of grains with HAGBs [156]. Faster recovery of grain boundaries at higher processing temperatures was reported elsewhere for a number of UFG materials such as CP Ti, Al and Mg alloys [157–159]. In these materials, the fraction of HAGBs increased with the drop of severe plastic deformation temperature.

Interstitial oxygen is influential in the grain growth kinetics of titanium, since higher oxygen content could suppress the grain growth and lead to a lower growth exponent [160]. Due to the diffusion of oxygen along grain boundaries at elevated temperatures, its effect on thermal stability should be considered. Therefore, at 900^{o}C, grain growth can be affected by not only the fraction of grains with high angle grain boundaries but also by the diffusion of oxygen along grain boundaries. Evidently, grain size of grade 2 Ti was observed to be similar to that of grade 4 at the higher end of the investigated temperature range. These microstructural observations were also supported by the similar flow stress levels of both grades over 800^{o}C (Fig. 6.4c, 6.4d, 6.5c and 6.5d).

6.6. Mechanism of Softening during Hot Deformation

Typically, two structural mechanisms are mainly responsible for the occurrence of DRX phenomenon [93]. One of them is related to the grain boundary bulging and this type of recrystallization is well-known as discontinuous dynamic recrystallization (dDRX). The creation of grain boundary serrations through dDRX is called strain induced-grain-boundary migration (SIBM) [96]. According to dDRX and SIBM theories, dynamically recrystallized grains nucleate on the original grain boundaries via the bulging mechanism. On the other hand, SIBM mechanism is based on the movement of boundaries caused by the difference in energy stored at two adjacent grains [161]. Different density of dislocations on both sides of a grain boundary exerts a driving force for bulging. Grain boundaries move to the side with higher dislocation density in order to decrease the internal energy [96]. Recrystallization taking place at former grain boundaries was shown previously (Fig. 6.2). For hot deformed titanium, observance of equiaxed fine grains at triple points and existing boundaries was interpreted with a similar mechanism based on the formation of dynamically recrystallized grains via boundary bulging [162]. A supporting argument was also reported for a beta titanium alloy deformed at 850^{o}C [99]. Observation of grain boundary serrations and nucleation of dynamically recrystallized grains in the vicinity of original grain boundaries suggest that dDRX took place during hot deformation of severely deformed Ti. Similar microstructural features during deformation of a nickel superalloy up to 1040^{o}C also support the occurrence of this DRX type in the present work [163,164].

Another possible mechanism for the formation of a recrystallized structure which was not observed for CP titanium at the examined range of temperatures and strain rates is continuous dynamic recrystallization (cDRX) [94]. The cDRX mechanism consists of the

development of subgrains with low angle boundaries in grain interiors. The boundary misorientations increase gradually during deformation leading to new grain formation at high strain levels [95,162]. In metals with high stacking fault energy, bulging of grain boundaries and their serrations occur at high strain levels leading to the evolution of equiaxed subgrains/grains from pre-formed pancaked substructure. This type of recrystallization is known as geometric DRX (gDRX) [93]. Although dDRX was the noticeable softening mechanism in the present study, other types of DRX may also be active over the course of high temperature compression.

6.7. Dynamic Recrystallization and the Model Predictions

A similar model was utilized in the chapter 5 to predict the high temperature flow response of severely deformed grade 2 titanium. It can be pointed out that especially at the lowest deformation temperature of 600^{o}C, the deviations between the predicted stress and experimental stress values for grade 4 Ti was lower as compared to the case for grade 2. The flow stress relations presented herein typically display decent predictions for cases where dynamic recrystallization is the dominant softening mechanism [135,137]. Owing to its lower processing temperature, grade 2 titanium would possibly contain a higher fraction of HAGBs [34,156,157]. On the other hand, higher processing temperature brings about a noticeable LAGB fraction in grade 4 titanium. Since the mobility of a LAGB is remarkably higher than that of a HAGB, the GBCD has a clear influence on the recrystallization kinetics [145]. Indeed, a recent study showed that recrystallization was favored for LAGBs at high homologous temperatures [165]. This could indicate a higher propensity for dynamic recrystallization during post-SPD high temperature compression of grade 4 titanium. This methodology is appropriate to a

certain degree for predicting flow stress curves for deformation conditions outside the experimental window as well. Since the deformation conditions are brought in the equation through the Z parameter, the flow stress behavior can be predicted in the entire domain where the apparent activation energy for hot working is similar.

Accelerated recrystallization of grade 4 titanium can also be traced by comparing the m values of both grades. It is well-known that the increased activity of diffusion related mechanisms and dynamic recrystallization at higher temperatures result in higher strain rate sensitivity [123]. In the present study, strain rate sensitivity of grade 2 points to a substantial increase above 700^{o}C, while strain rate sensitivity of grade 4 demonstrates a sharp rise at 600^{o}C indicating a sooner onset with the dominance of DRX mechanisms. The strain rate sensitivity values obtained at 800^{o}C are slightly greater than those obtained at 900^{o}C for the whole strain intervals of both grades. It is expected that m values increase with the rise of deformation temperature due to thermally activated mechanisms. However, constancy of m can be attributed to the onset of DRX processes which may occur over a range of strain rates and temperatures [9,124]. Lower activation energy values can also be ascribed to the presence of softening mechanisms such as DRX. As depicted in section 6.4, energy required to activate post-SPD hot deformation in the examined range was observed to be lower for severely deformed grade 4 titanium as possibly related to its higher processing temperature.

7. Warm Tensile Deformation and Fracture Behavior of Ultrafine-Grained Grade 4 Titanium

By conducting hot compression tests on two grades of titanium after SPD, it was found that severely deformed grade 4 Ti was less stable at 600^{o}C due to the aforementioned reasons in the previous chapter. Therefore, it was necessary to investigate the warm characteristics of severely deformed Ti to get a better understanding of DRV and DRX mechanisms in this UFG material. Since compression test is a great experiment for estimating required forces to be applied during hot rolling or forging of metals, hot compression tests were performed. In the cold to the warm regime, obtaining the mechanical properties such as ductility, strength and toughness can play an important role in designing parts. These mechanical properties can be calculated by conducting tension tests. Thus, tensile tests were carried out in the warm regime.

7.1. Mechanical Response of Severely Deformed Grade 4 Ti at Ambient and Warm Temperature

Fig. 7.1 displays the tensile stress-strain curves of severely deformed titanium at various temperatures ranging from ambient to 600^{o}C and strain rate of 0.001-0.1s^{-1}. Flow stress levels remarkably drop with the rise of deformation temperature. The flow stress obtained at ambient temperature is noticeably greater than those obtained at temperatures above it. This can be attributed to the temperature dependence of diffusion related dynamic softening mechanisms such as DRV and DRX [16,114,166]. It is well-established that higher deformation temperatures accelerate dislocation motion which in turn facilitates dynamic softening mechanisms [167]. It is also worth noting that at 600^{o}C, ECAE processing enabled higher ductility reaching over 10%. This behavior can

be explained by the occurrence of DRV and DRX at this deformation temperature. Semenova et al. [168] reported that ductility of UFG titanium rods considerably increases with the rise of temperature. Higher ductility of UFG titanium rods was achieved by changes in grain boundary structure [168].

Another important observation in Fig. 7.1 is the influence of deformation rate on stress-strain curves of severely deformed titanium. It can be seen that flow stress levels are more sensitive to the rate of deformation when the deformation temperature reaches at or above 400^{o}C. Particularly, reduction in the rate of deformation results in decrease of flow stress levels. It is well-known that lower strain rates weaken the tendency for defect interactions and provide longer time for recovery and recrystallization of deformed structure [168,169]. The variation of the elongation with the rate of deformation at different temperatures also needs to be taken into account. At all deformation temperatures except 600^{o}C, ductility of severely deformed titanium is improved with the decrease of strain rate. At 600^{o}C, although stress levels are very sensitive to the rate of deformation, elongation values are almost similar at different strain rates.

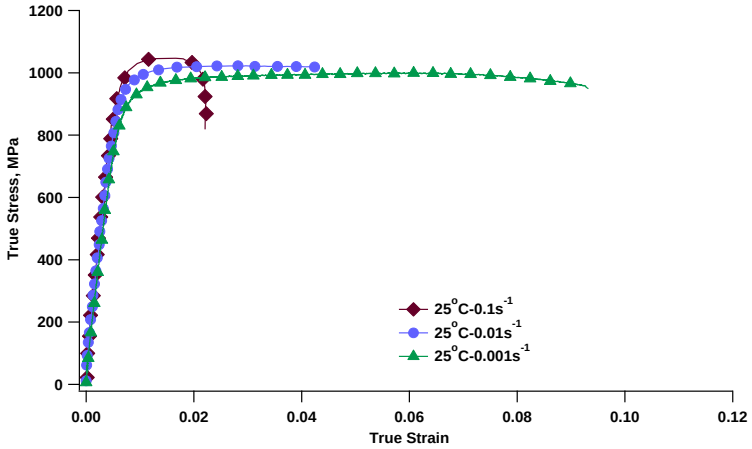

(a)

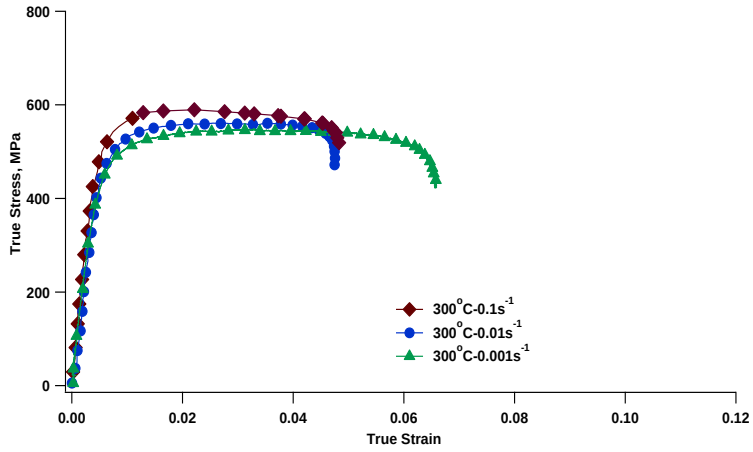
True Stress, MPa
True Strain
300°C-0.1s-1
300°C-0.01s-1
300°C-0.001s-1

(b)

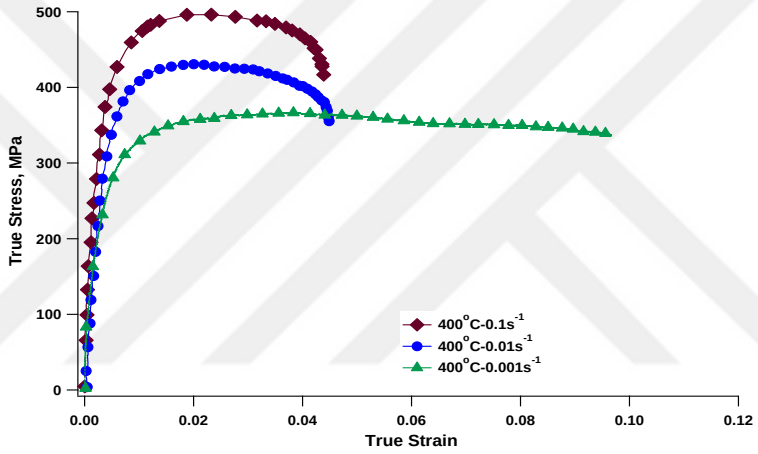
True Stress, MPa
True Strain
400°C-0.1s-1
400°C-0.01s-1
400°C-0.001s-1

(c)

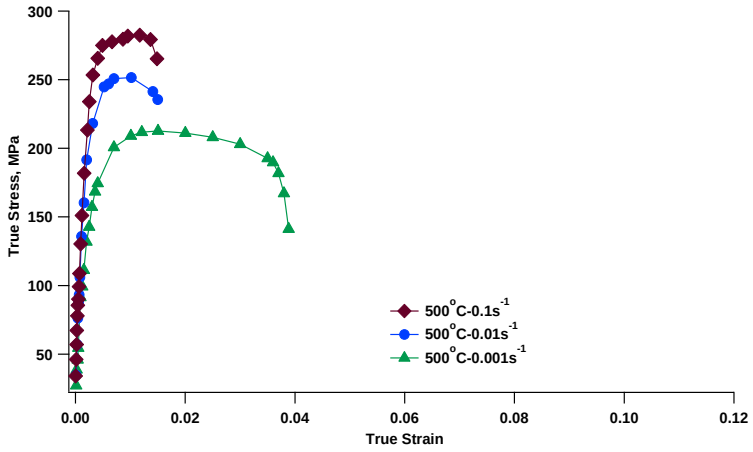
True Stress, MPa
True Strain
500°C-0.1s-1
500°C-0.01s-1
500°C-0.001s-1

(d)

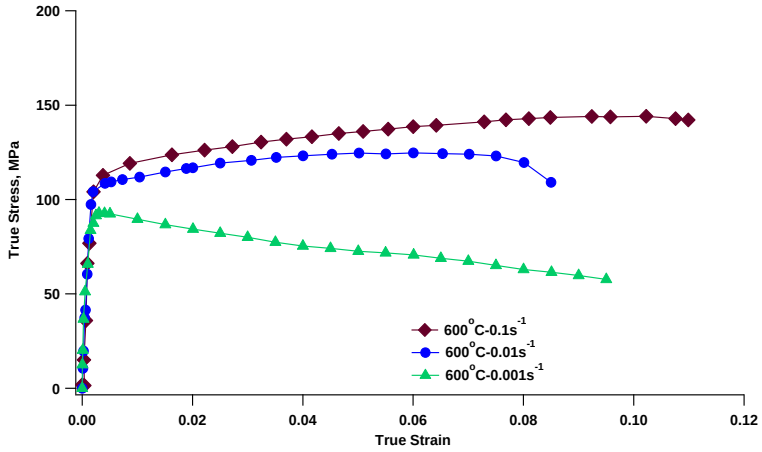

(e)

Figure 7.1 True stress–true strain response of severely deformed Ti with different strain rates at (a) 25°C, (b) 300°C, (c) 400°C, (d) 500°C, and (e) 600°C

In order to investigate the impacts of ECAE processing on warm characteristics of CP grade 4 titanium, warm temperature tensile tests were performed on both as-received and severely deformed CP titanium at a strain rate of $0.01s^{-1}$ and at temperatures of 300-600°C (Fig. 7.2). It follows from Fig. 7.2 that ECAE could enhance the strength of CP grade 4 Ti at or below 500°C. The rise of flow strength is related to the effect of the dislocation substructure and the high density of grain boundaries [110, 111]. A report on Ti-6Al-4V alloy stated that higher strength levels were seen up to 500°C for UFG material in comparison with its coarse structure; the effect of UFG microstructure diminished above 500°C due to recrystallization and growth [122]. The enhancement in strength of UFG materials during warm deformation was also reported at a temperature range of 300-450°C for Al6063 alloy [121]. At 600°C, strength of severely deformed sample was observed to be similar to that of the coarse grained one. This behavior can be rationalized in terms of the manifestation of dynamic recrystallization at such a high deformation temperature as reported in the chapter 6. It is well-documented that at elevated temperature UFG materials are prone to severe recovery and recrystallization due to their

high dislocation density and high fraction of sub-grain and grain boundaries [170]. In addition, SPD was found to have detrimental effects on the ductility of CP titanium at temperatures less than 600°C. At the highest deformation temperature (600°C), severely deformed samples showed a more ductile behavior than the CG one. This could be attributed to the activation of grain boundary mediated mechanisms in addition to improved dislocation glide with multiple slip systems [111, 160, 161]. Grain boundary diffusion mechanisms such as grain boundary sliding (GBS) need to be considered at high temperatures. Especially, GBS might be the controlling deformation mechanism for UFG materials due to the fact that these materials contain relatively higher density of boundaries and shorter path ways of diffusion [172,173]. On the other hand, Low ductility of as-received sample can be connected with the hot embrittlement at elevated temperature [174]. It was reported that dynamic recrystallization took place in UFG structure in a higher degree, which inhibits nucleation and propagation of microvoids and cracks.

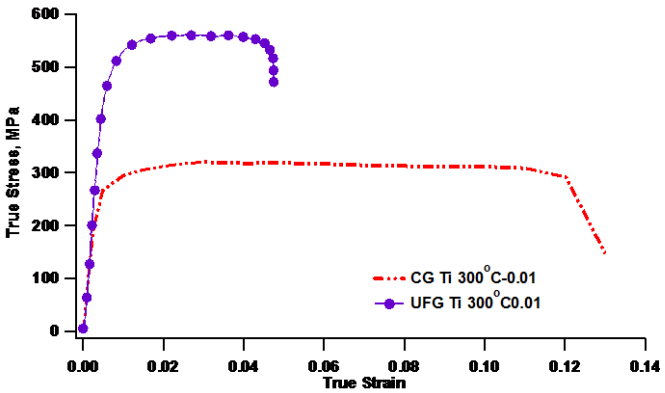

(a)

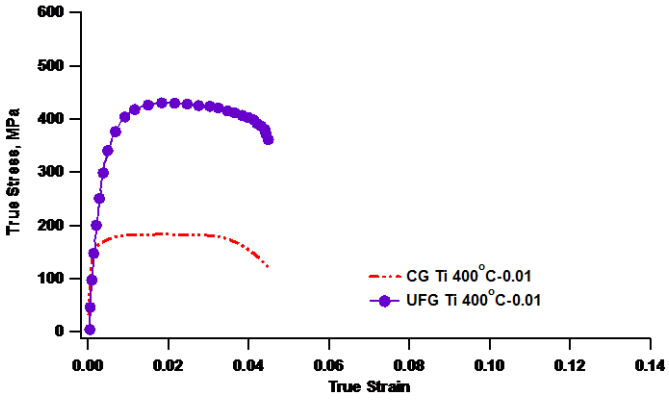

(b)

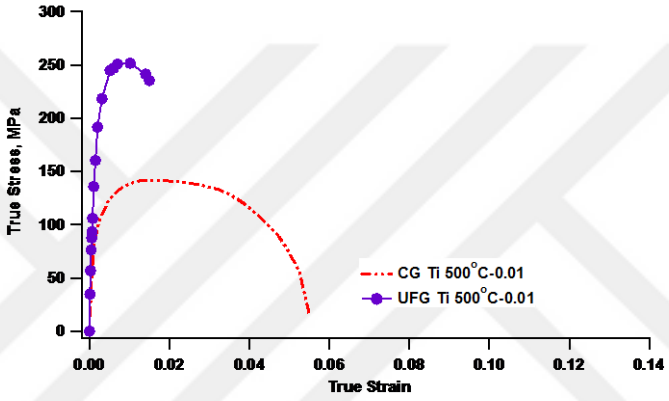

(c)

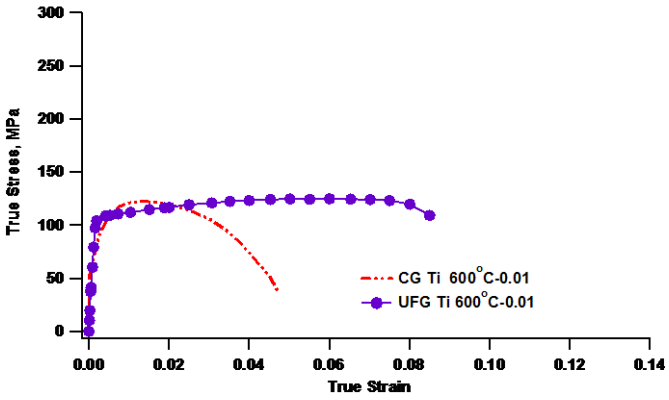

(d)

Figure 7.2 True stress- true strain response of CG and UFG titanium at (a) 300^{o}C with strain rate of 0.01s^{-1} (b) 400^{o}C with strain rate of 0.01s^{-1} (c) 500^{o}C with strain rate of 0.01s^{-1} and (d) 600^{o}C with strain rate of 0.01s^{-1}

The variation of peak stress as a function of temperature at different strain rates is represented in Fig. 7.3a. Peak stress values considerably decrease with increasing deformation temperature at all strain rates. This observation can be attributed to reduced dislocation interactions leading to lower work hardening rate [114]. Fig. 7.3b demonstrates the variation of elongation to fracture versus deformation temperature. At all deformation rates, samples deformed at 600^{o}C exhibited the highest elongation to fracture which can be explained by the activation of GBS mechanism at this temperature. As it was mentioned earlier, ductility can be enhanced by the occurrence of GBS.

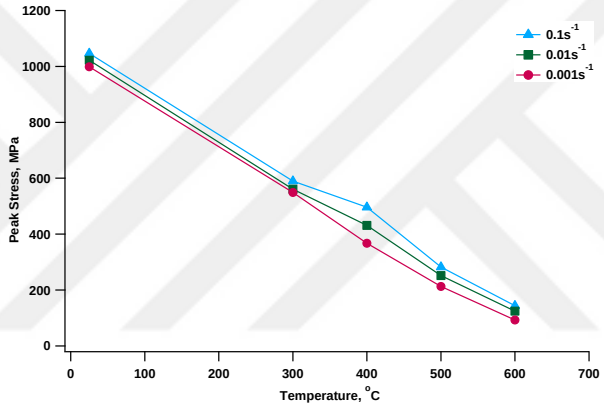

(a)

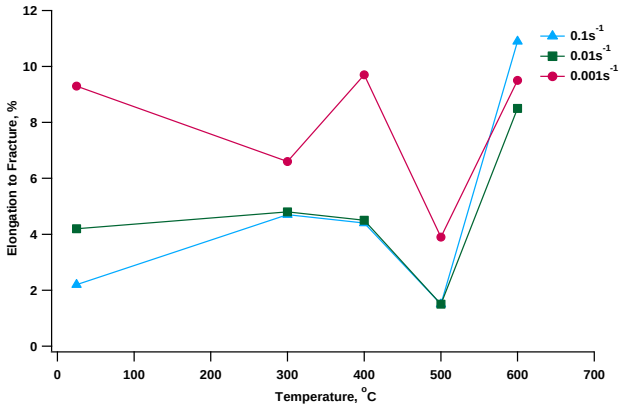

(b)

Figure 7.3 Effects of deformation parameters on the (a) peak stress and (b) elongation to fracture

Strain rate sensitivity is an important property to study workability and formability of materials at various temperatures. Strain rate sensitivity, m, is related to the influence of strain rate on dislocation generation and propagation and as such is an index of workability. m values are evaluated from the slope of the $\ln\sigma$-$\ln\dot{\varepsilon}$ curve at constant temperature and strain. Fig. 7.4 shows the variation of strain rate sensitivity as a function of strain. It follows from Fig. 7.4 that strain rate sensitivity remarkably increases with rise of temperature due to thermally activated mechanisms. It is well-known that the increased activity of diffusion related mechanisms and DRX at higher temperatures resulting in higher strain rate sensitivity [9,124].

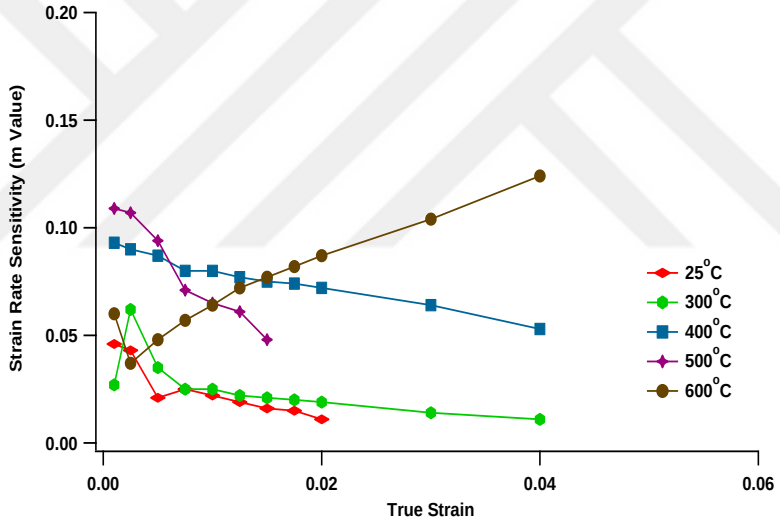

Figure 7.4 Effect of deformation strain on the strain rate sensitivity coefficient (m) of the severely deformed titanium

7.2. Microstructure Evolution of Severely Deformed Grade 4 Ti during Warm Deformation

To investigate the effects of ECAE processing on microstructure evolution of CP grade 4 Ti, SEM studies were carried out. The SEM micrographs of the CG and severely

deformed CP titanium followed by tensile tests at various temperatures are shown in Fig. 7.5. Evidently, deforming coarse-grained titanium at higher deformation temperature (600^{o}C) led to a slight grain growth (comparing Fig. 7.5a and b). Fig.7.5c-g display the impacts of test temperature on the microstructural evolution of severely deformed titanium. It can be seen that a gradual grain growth took place at temperatures below 600^{o}C, while a noticeable grain growth occurred at the highest deformation temperature. The presence of equiaxed grains is mostly detectable for this deformation temperature and could be identified as dynamically recrystallized structures. The growth of dynamically recrystallized grains with rise of deformation temperature up to 600^{o}C was also reported for UFG titanium elsewhere [175]. These SEM observations were also supported by the similar flow responses of severely deformed titanium at 600^{o}C (Fig. 7.1e).

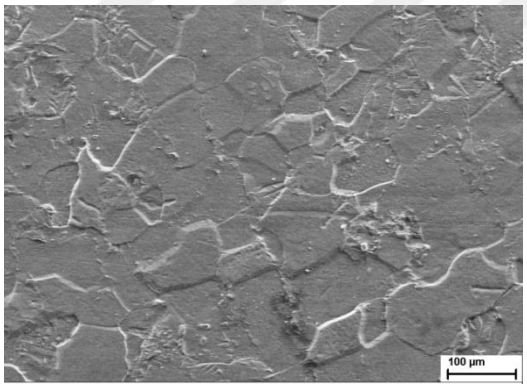

(a)

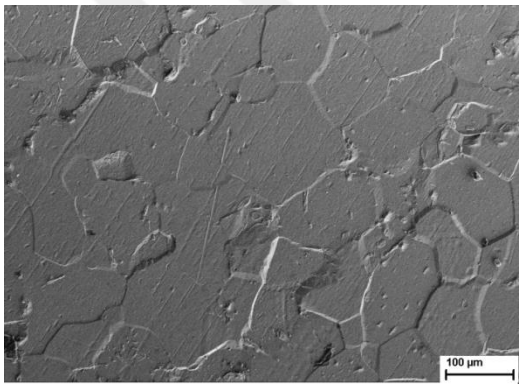

(b)

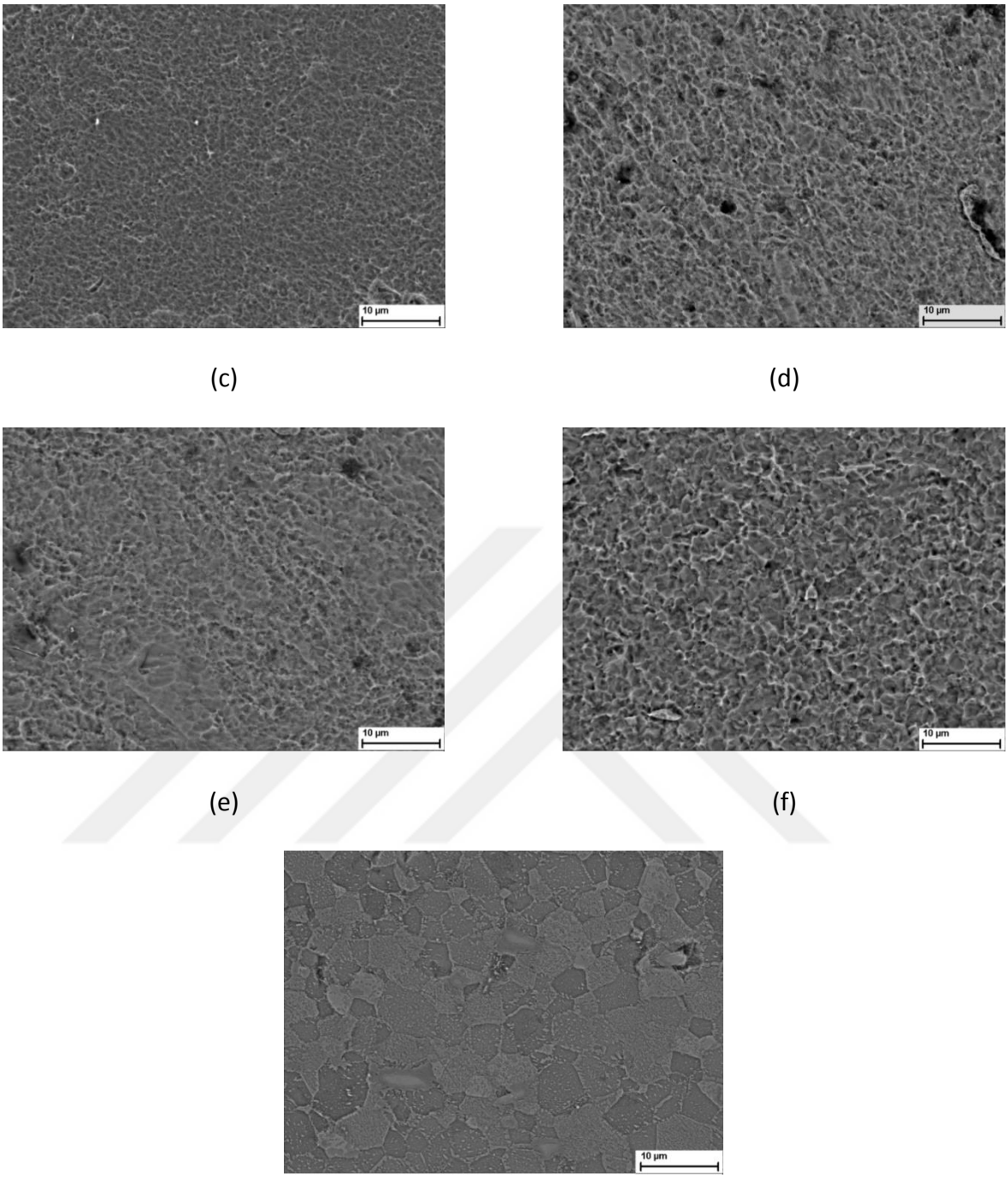

Figure 7.5 SEM micrographs of the following conditions; as-received titanium tested at 300^{o}C with the strain rate of 0.01s^{-1}, (b) as-received titanium tested at 600^{o}C with the strain rate of 0.01s^{-1}, (c) severely deformed titanium tested at 25^{o}C with the strain rate of 0.1s^{-1}, (d) severely deformed titanium tested at 300^{o}C with the strain rate of 0.1s^{-1}, (e) severely deformed titanium tested at 400^{o}C with the strain rate of 0.1s^{-1}, (f) severely deformed titanium tested at 500^{o}C with the strain rate of 0.1s^{-1}, (g) severely deformed titanium tested at 600^{o}C with the strain rate of 0.1s^{-1}

The influences of deformation rate on the microstructure evolution of severely deformed titanium are also studied as shown in Fig. 7.6. The rate of deformation is not highly influential at lower temperatures, while deforming samples at 600 °C for longer periods caused a coarser structure since dynamically recrystallized grains had enough time to grow after nucleation (Fig. 7.6a-d). Higher temperatures provide the microstructure with a remarkable driving force for DRX [176]. Therefore, exposure to high temperature (600^{o}C) for longer times led to such a coarse structure with the average grain size of 9µm.

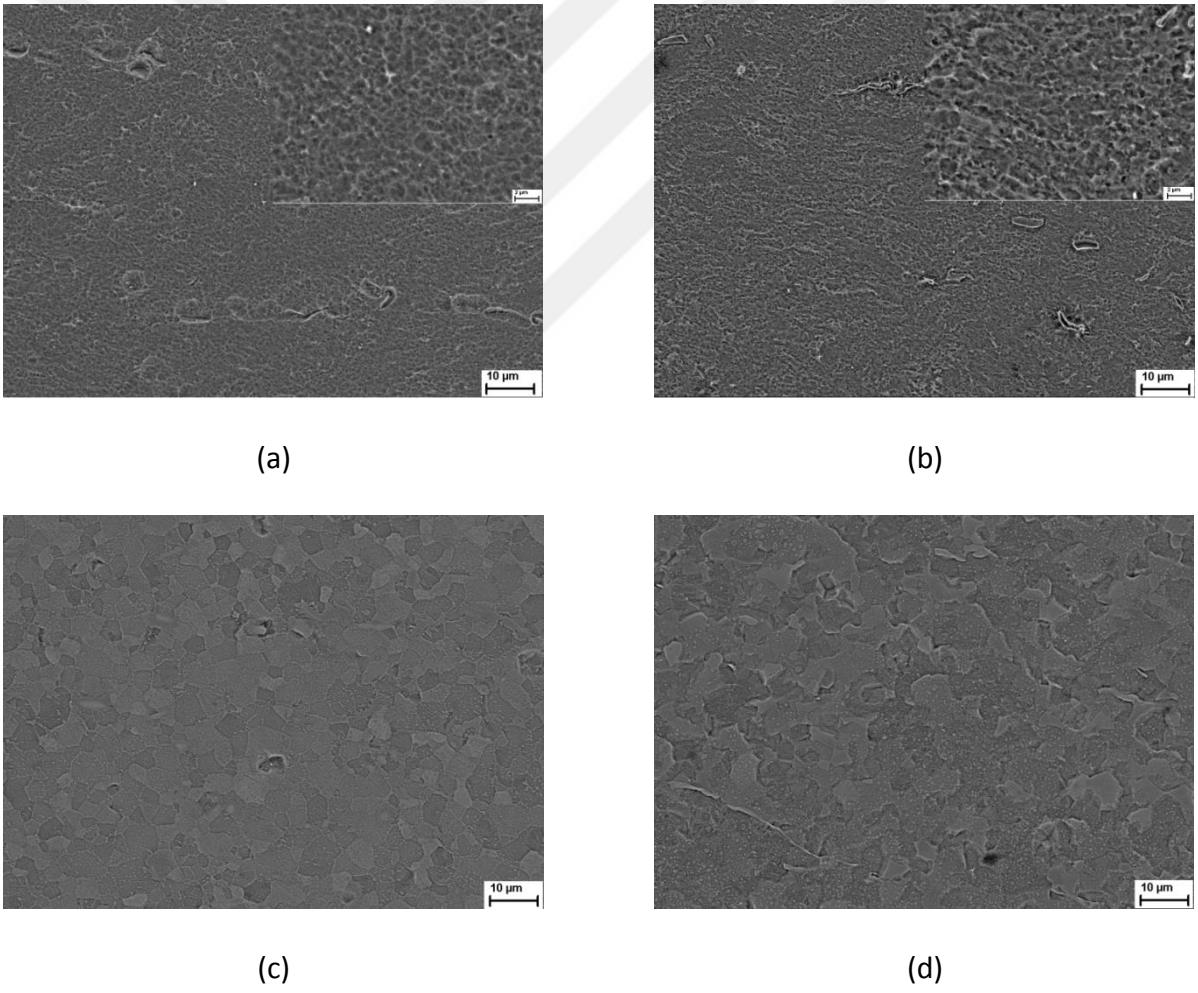

(a) (b)

(c) (d)

Figure 7.6 SEM micrographs of the following conditions; (a) severely deformed titanium tested at 300^{o}C with the strain rate of 0.1s^{-1} (low and high magnification), (b) severely deformed titanium tested at 300^{o}C with the strain rate of 0.001s^{-1} (low and high magnification), (c) severely deformed titanium tested at 600^{o}C with the strain rate of 0.1s^{-1}, (d) severely deformed titanium tested at 600^{o}C with the strain rate of 0.001s^{-1}

7.3. Fracture Surface Analysis of Severely Deformed Grade 4 Ti during Warm Deformation

In order to reveal the fracture behavior of UFG titanium during warm tensile tests, SEM investigations have been conducted on deformed samples. Fig. 7.7 demonstrates the effects of deformation temperature on fracture surfaces of severely deformed titanium. All micrographs are captured at the same magnification to make the comparisons more meaningful. Accordingly, the fracture surfaces of all samples show a noticeable amount of equiaxed dimples and micro-voids confirming the occurrence of ductile fracture. At ambient temperature, dimpled rupture on fracture surfaces is apparent which suggests the existence of localized deformation in UFG titanium. Fracture behavior of severely deformed titanium followed by tensile tests at ambient temperature was previously studied elsewhere reporting similar findings on fracture morphology of this material [177]. It is noteworthy that the size of dimples and micro-voids sharply increases with the rise of deformation temperature. A denser dimple structure at the fracture surface was observed for the sample deformed at room temperature. With increased temperature, void coalescence occurs as a fracture mechanism [171]. This can be attributed to the enhancement of diffusion rate at higher deformation temperatures [66,138]. It is also well-established that coalescence of voids is an internal necking mechanism which takes place repeatedly at low to moderate stress levels within elevated temperature deformation [178,179].

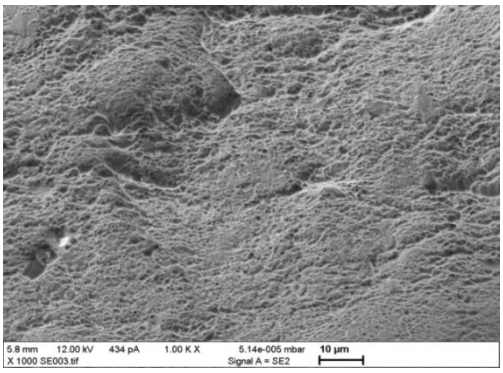

(a)

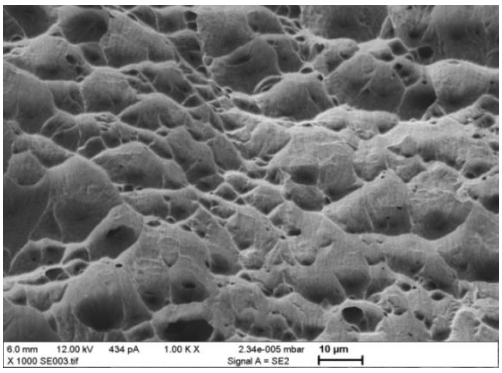

(b)

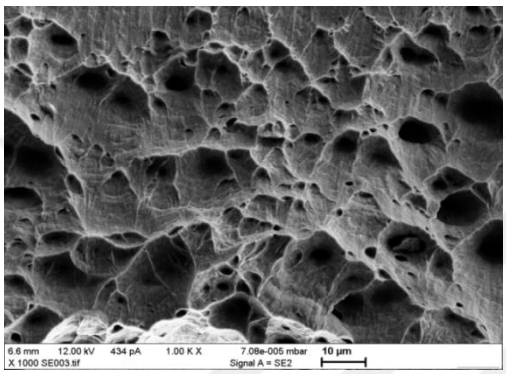

(c)

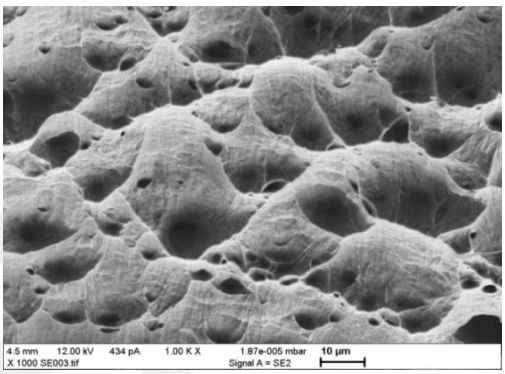

(d)

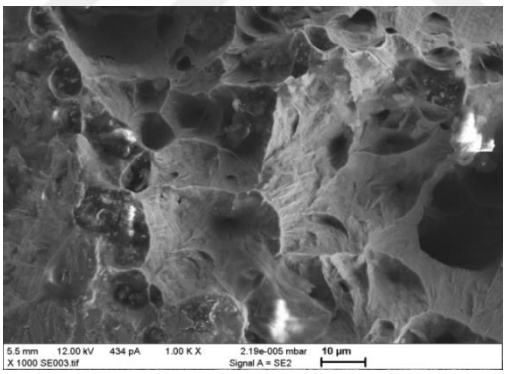

(g)

Figure 7.7 Fracture surface of the specimens; (a) severely deformed Ti tested at 25^{o}C with the strain rate of 0.001s^{-1}, (b) severely deformed Ti tested at 300^{o}C with the strain rate of 0.001s^{-1}, (c) severely deformed Ti tested at 400^{o}C with the strain rate of 0.001s^{-1}, (d) severely deformed Ti tested at 500^{o}C with the strain rate of 0.001s^{-1}, (g) severely deformed Ti tested at 600^{o}C with the strain rate of 0.001s^{-1}

The effect of strain rate on fracture surfaces of severely deformed titanium was also studied as presented in Fig. 7.8. Similar to the case of grain size (Fig. 7.6), deforming titanium at various strain rates and at a temperature of 300^{o}C did not show a different

fracture behavior (Fig. 7.8a and 7.8b). On the other hand, at 600^{o}C size of dimples and micro-voids varied with strain rate displaying mainly larger voids and dimples at lower deformation rate. It is worth noting that growth of dimples and voids takes place with the decrease in strain rate since lower rate of deformation provides sufficient time for coalescence and growth [171]. Besides, higher deformation temperature (600^{o}C) facilitates internal necking ability that leads to higher resistance of structure to cavity formation and hence higher ductility [167]. Therefore, microstructural features on the fracture surfaces support the higher elongation observed at 600^{o}C.

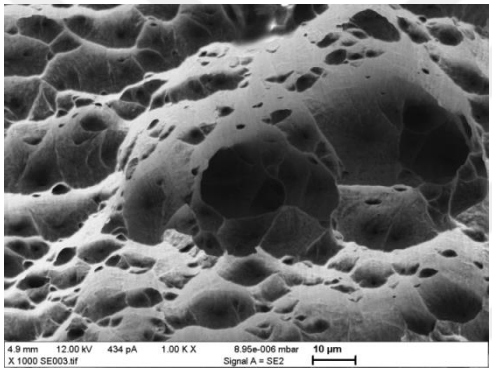

(a)

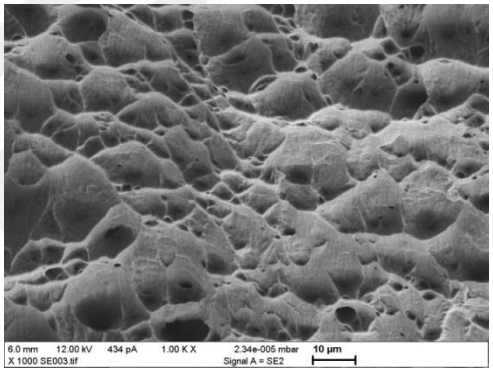

(b)

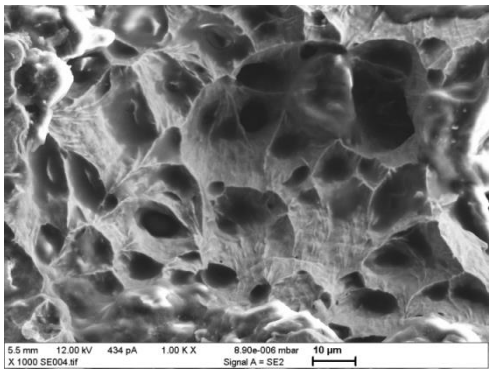

(c)

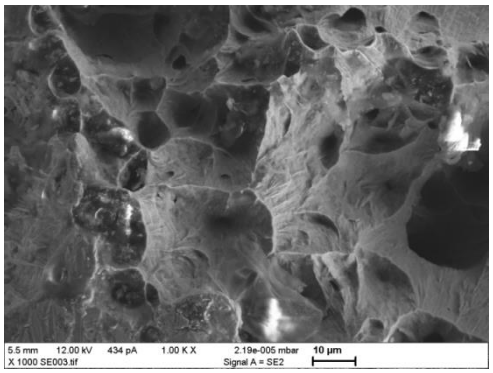

(d)

Figure 7.8 Fracture surface of the specimens; (a) severely deformed titanium tested at 300^{o}C with the strain rate of 0.1s^{-1}, (b) severely deformed titanium tested at 300^{o}C with the strain rate of 0.001s^{-1}, (c) severely deformed titanium tested at 600^{o}C with the strain rate of 0.1s^{-1}, (d) severely deformed titanium tested at 600^{o}C with the strain rate of 0.001s^{-1}

A very important finding on monotonic behavior of severely deformed titanium in the previous and the current chapters is that UFG grade 2 and grade 4 titanium showed a stable monotonic deformation response up to homologous temperatures of T_h=0.45 and T_h=0.40, respectively. As can be observed in Table 7.1, UFG materials display recovery and recrystallization at various homologous deformation temperatures. It is well-known that SPD processing at lower processing deformation led to the rise of the homologous temperature for occurrence of softening mechanisms [158]. Therefore, higher ECAE processing temperature for fabrication of UFG grade 4 resulted in the lower homologous temperature in this material compared to that of grade 2.

Table 7.1 The comparison of homologous temperatures for various UFG materials in monotonic loading

Alloy	T_h
UFG Grade 4 Ti	0.40, Present Study
UFG Grade 2 Ti	0.45, Present Study
UFG Ta	0.21 [180]
UFG Au	0.35 [181]
UFG Cu	0.42 [182]
UFG Mg-3Al-Zn	0.52 [103]

7.4. Tension–Compression Asymmetry of Severely Deformed Grade 4 Ti at 600^{o}C

Tensile and compressive flow stresses and their corresponding microstructural features of severely deformed grade 4 titanium are shown in Fig 7.9. It is obvious that

there is a significant tension-compression asymmetry for the samples deformed at 600°C with a strain rate of $0.1s^{-1}$. However, the asymmetry is not considerable in the samples deformed at lower deformation rates. It is well-documented that softening mechanisms reduce the level of asymmetry [183,184]. Deforming severely deformed titanium at lower rate of deformation provides longer time for energy accumulation and higher dislocation mobility around boundary regions. Micrographs also revealed the occurrence of recrystallization and grain growth at lower strain rates. Therefore, drop of tension-compression asymmetry at lower strain rate can be connected to the occurrence of DRV and DRX.

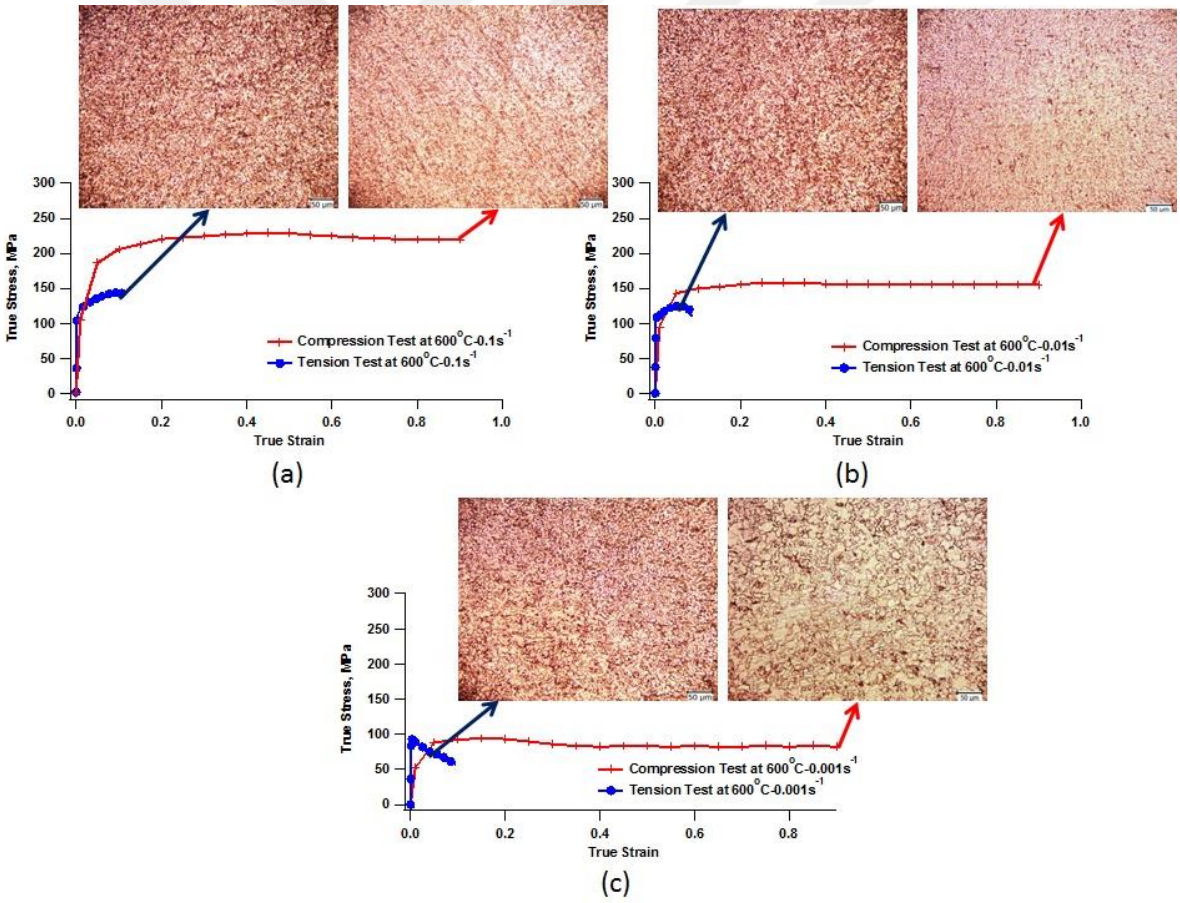

Figure 7.9 Tensile and compressive flow stresses with their corresponding microstructural features of severely deformed grade 4 titanium at 600°C and at strain rate of (a) $0.1s^{-1}$ (b) $0.01s^{-1}$ and (c) $0.001s^{-1}$

8. Cyclic Deformation Response of Ultrafine-grained Ti at Elevated Temperatures

Monotonic deformation response of UFG Ti has been the subject of previous chapters. The necessity of investigating the fatigue properties of UFG Ti to demonstrate its performance under cyclic loads has drawn our attention towards the cyclic deformation response (CDR) of this material. Therefore, the aim of this chapter is to investigate the cyclic stability of ECAE processed titanium with varying routes by underlining the similar and contrasting features. In this quest, CDR and microstructural evolution of severely deformed grade 4 titanium at different temperatures (up to 600^{o}C) and various strain amplitudes are presented. Until now, low cycle fatigue (LCF) behavior at elevated temperature has not been not been considered for severely deformed titanium. This effort was made in order to complement the understanding on the thermo-mechanical behavior of CP Ti.

8.1. Cyclic Response of CP Ti at Room Temperature

Fig. 8.1 represents the evolution of cyclic stress versus the number of cycles at various strain amplitudes and mid-life hysteresis loops for CG and route-8E processed UFG Ti at ambient temperature. Generally, fatigue life and cyclic stability of both UFG and CG Ti are degraded with the increase of strain amplitude. It is well-known that fatigue crack propagation can be accelerated with rising strain amplitude [185]. Similar cyclic deformation behavior was also reported for Ti alloy IMI 834 [186]. At the same strain amplitude, UFG Ti shows higher fatigue life and stress rage values than those of CG material. By considering mid-life hysteresis loops of probed specimens as depicted in Fig. 8.1b, fatigue behavior of this material can be studied in more detail. The area of a

hysteresis loop presents energy dissipation and hence fatigue performance of a material. It is well-known that a higher energy dissipation per cycle leads to a more intense dislocation activity which makes microstructure prone to crack nucleation [187]. Therefore, half-life hysteresis loops of UFG and CG Ti also confirm that a better fatigue performance can be expected in severely deformed Ti. Previously, a stable CDR was also reported for UFG Ti at room temperature [73].

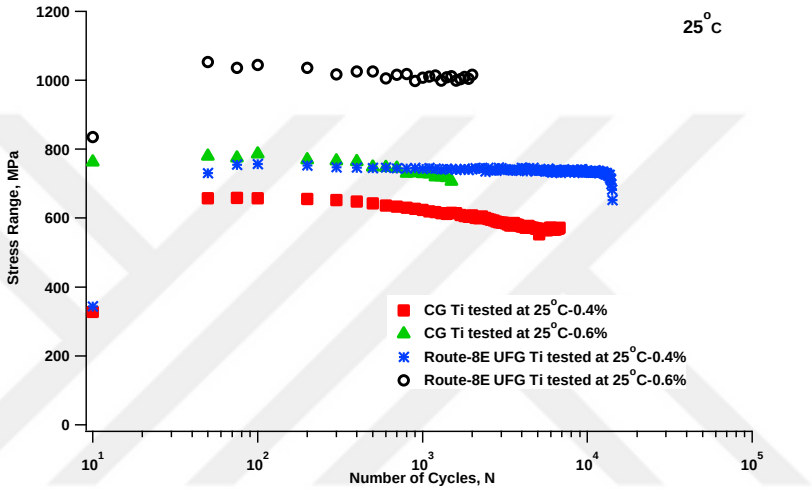

(a)

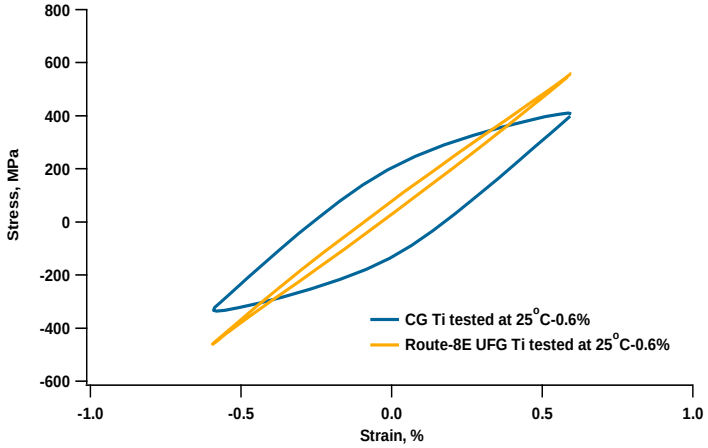

(b)

Figure 8.1 (a) CDR of CG and UFG Ti at ambient temperature (b) Mid-life hysteresis loops of CG and UFG Ti at ambient temperature with strain amplitude of 0.6%

8.2. Cyclic Response of CP Ti at Elevated Temperature

The stress range-fatigue life curves of both UFG and CG Ti at 400 and 600^{o}C are displayed in Fig. 8.2. It is evident that the cyclic stabilities of both UFG and CG Ti are sensitive to both temperature and strain amplitude. It can be seen that at all examined strain amplitudes, UFG Ti exhibits higher stress range values than those of CG Ti at 400^{o}C. In contrast, CG Ti surpassed UFG Ti at the higher temperature of 600^{o}C (Fig. 8.2b). Higher stress range levels of UFG materials during LCF can be imputed to their higher volume fraction of HAGBs which hinder movement of dislocations [73]. However, high temperature can facilitate the occurrence of recrystallization and grain growth which leads to lower strength levels [151]. A study on UFG interstitial free (IF) steel also showed that UFG structure remains thermally stable up to 500^{o}C and stress range levels considerably decreased at higher temperatures [188]. Another parameter which needs to be investigated is the fatigue life. Fatigue lives of both UFG and CG Ti drop with the rise of temperature which could be rationalized in terms of homologous temperature (T_h=T/T_m). It is well-documented that fatigue lives of UFG materials can be influenced by being exposed to temperatures above a critical T_h value [106,107,188,189]. This value was reported as 0.20, 0.26, 0.32 and 0.40 for UFG copper, UFG IF steel, NbZr and UFG AlMg alloy, respectively. Temperatures above 400^{o}C exceed T_h of 0.35 and hence adversely affect fatigue life of CP Ti. Therefore, UFG Ti is still stable at or below 400^{o}C, whereas, cyclic and thermal instability was observed at 600^{o}C, corresponding to 0.46 T_h. In Chapter 6, thermal stability of severely deformed grade 4 titanium under monotonic loading was seen to be up to 500^{o}C (T_h=0.40). Lower homologous temperature under cyclic loading can be attributed to the higher exposure time for the fatigued samples.

To study the impact of strain amplitude on CDR, three amplitudes of 0.2, 0.4 and 0.6% were selected. Results imply that both stress range and fatigue life show a strong dependence to strain amplitude (Fig. 8.2). Accordingly, UFG and CG Ti could tolerate higher cycle numbers at lower strain amplitudes. This was previously rationalized in terms of grain boundary stabilization by the impurities in the microstructure which was mentioned for UFG Ti and other materials [73,188,190–193]. At 400^{o}C for a strain amplitude of 0.2%, fatigue life of UFG Ti was seen to reach over 85000 cycles, while CG structure withstood less than 16000 cycles. Noteworthily, LCF experiments on UFG Ti at 400^{o}C with strain amplitudes of 0.4 and 0.6% resulted in cyclic hardening which is replaced by a subsequent softening and cyclic instability. This could be attributed to the occurrence of two significant damaging mechanisms as elaborated in the next section.

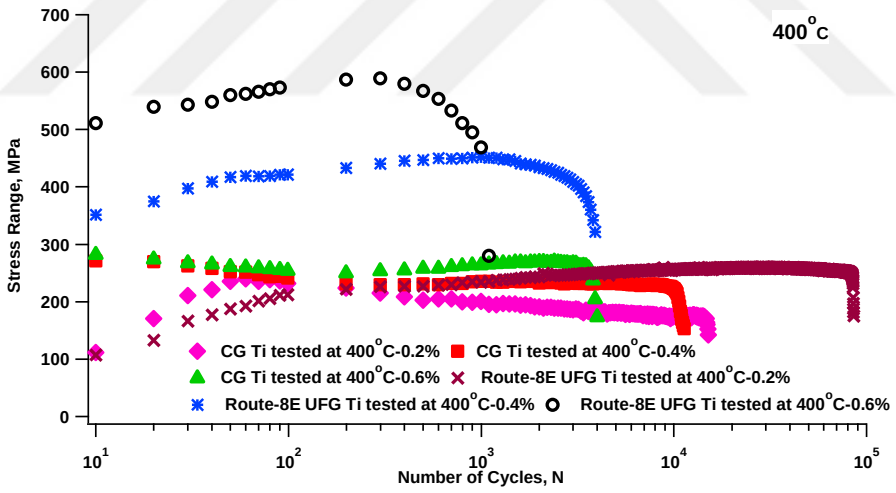

(a)

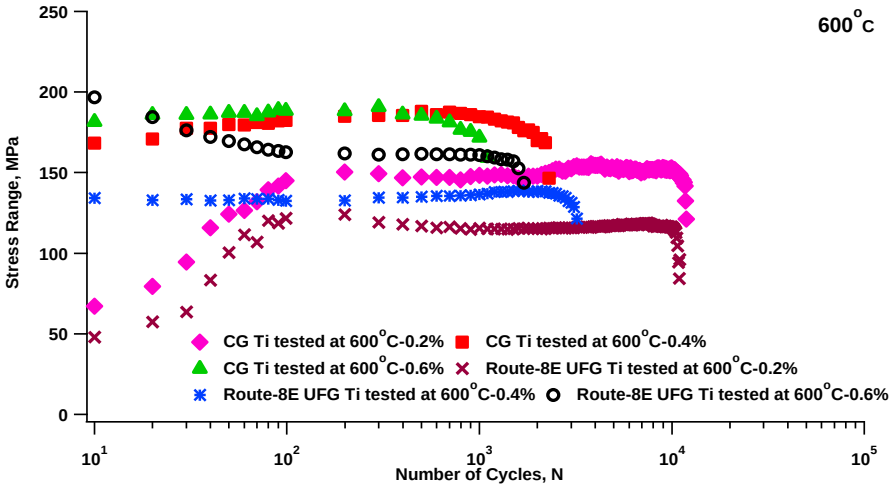

(b)

Figure 8.2 CDR of CG and UFG Ti at (a) 400°C and (b) 600°C

8.3. Cyclic Response of CP Ti at Various Temperatures

In order to observe the effect of testing temperature on fatigue behavior of CG and UFG Ti, cyclic deformation responses at various temperatures are depicted in Fig. 8.3. Irrespective to the grain size, stress range values and fatigue lives noticeably decrease with increasing testing temperature. As it was mentioned earlier, UFG Ti shows cyclic stability up to 600°C. For the sake of brevity, aforementioned reasons for cyclic behavior of CG and UFG Ti are not repeated in the present section.

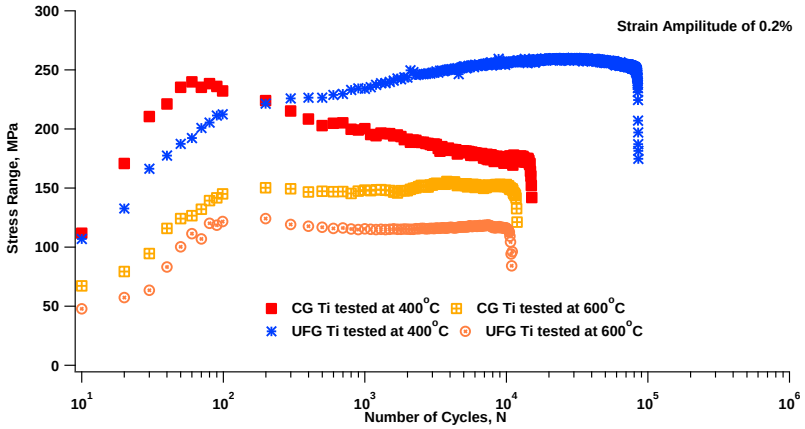

(a)

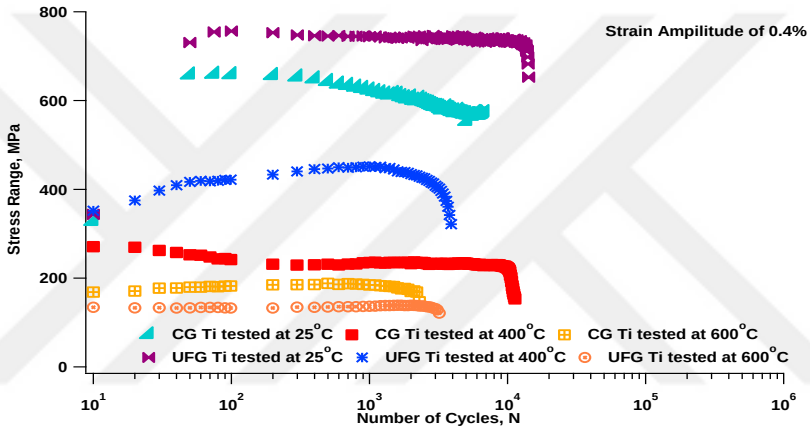

(b)

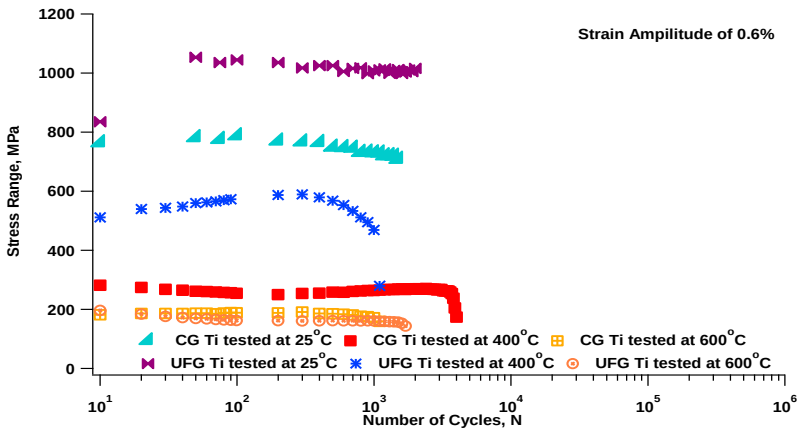

(c)

Figure 8.3 CDRs of CG and UFG Ti at various temperatures with strain amplitudes of (a) 0.2%, (b) 0.4% and (c) 0.6%

Fig. 8.4 represents the mid-life hysteresis loops of CG and UFG Ti at elevated temperatures. It can be seen that the loops of both CG and UFG structure are symmetrical. Regardless of the grain size, stress range values noticeably increase with the rise of strain amplitude. Similar symmetrical mid-life hysteresis loops were also reported for Ti alloys where the fatigue experiments were conducted at room temperature [194,195]. It is also noteworthy that at 400^{o}C, the area of UFG Ti hysteresis loops is significantly less than that attained for CG Ti samples. On the other hand, at 600^{o}C UFG Ti hysteresis loops show similar area as compared to CG loops. This would mean that inferior fatigue performance is expected at the highest testing temperature. Therefore, these findings support superior fatigue performance and high stress range levels of UFG Ti at or below 400^{o}C.

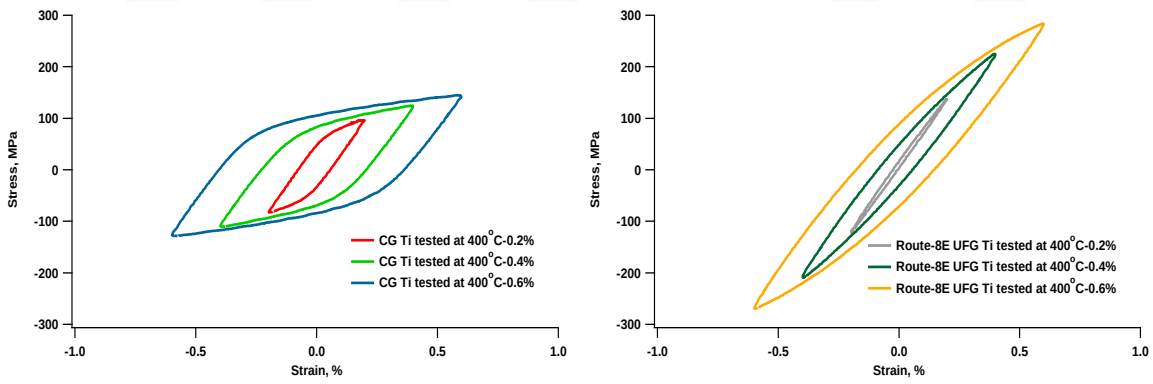

(a) (b)

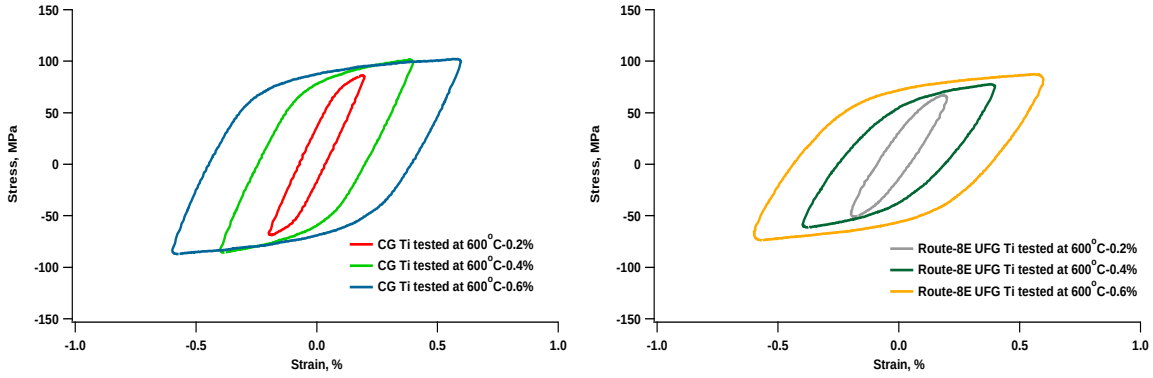

(c) (d)

Figure 8.4 Mid-life hysteresis loops of (a) CG Ti at 400°C, (b) UFG Ti at 400°C (c) CG Ti at 600°C and (d) UFG Ti at 600°C

8.4. Microstructural Evolution

Optical micrographs of UFG Ti subjected to cyclic loading at 400°C and 600°C with strain amplitude of 0.2% are presented in Fig. 8.5. Images were captured in the vicinity of fatigue cracks. It is clear that microstructure of UFG Ti sample fatigued at 400°C still consists of regions with ultrafine grains. In contrast, recrystallization and grain growth happened in severely deformed Ti sample under cyclic loading at 600°C. It is documented that the movement of grain boundaries, which is known as the main mechanism of grain growth, is facile at such a high temperature [154,196].

In order to study the influence of ECAE processing on the fracture behavior of UFG titanium within cyclic loading, SEM studies were carried out. The SEM micrographs of the severely deformed CP titanium followed by LCF experiments at various temperatures are shown in Fig. 8.5c and 8.5d. The micrographs were captured in the vicinity of the crack initiation sites and along the crack propagation zone of the fatigued samples. A typical fracture surface including striations and beach mark patterns were seen at both examined temperatures. Generally, crack propagation zone is distinguished by the aforementioned

striations that are perpendicular to the crack growth direction [197]. It can also be noticed that cyclic loading at higher temperatures resulted in coarser fatigue striations. Kitahara et al. also reported a similar striation pattern for fatigue crack growth tests of UFG titanium processed via ARB [76].

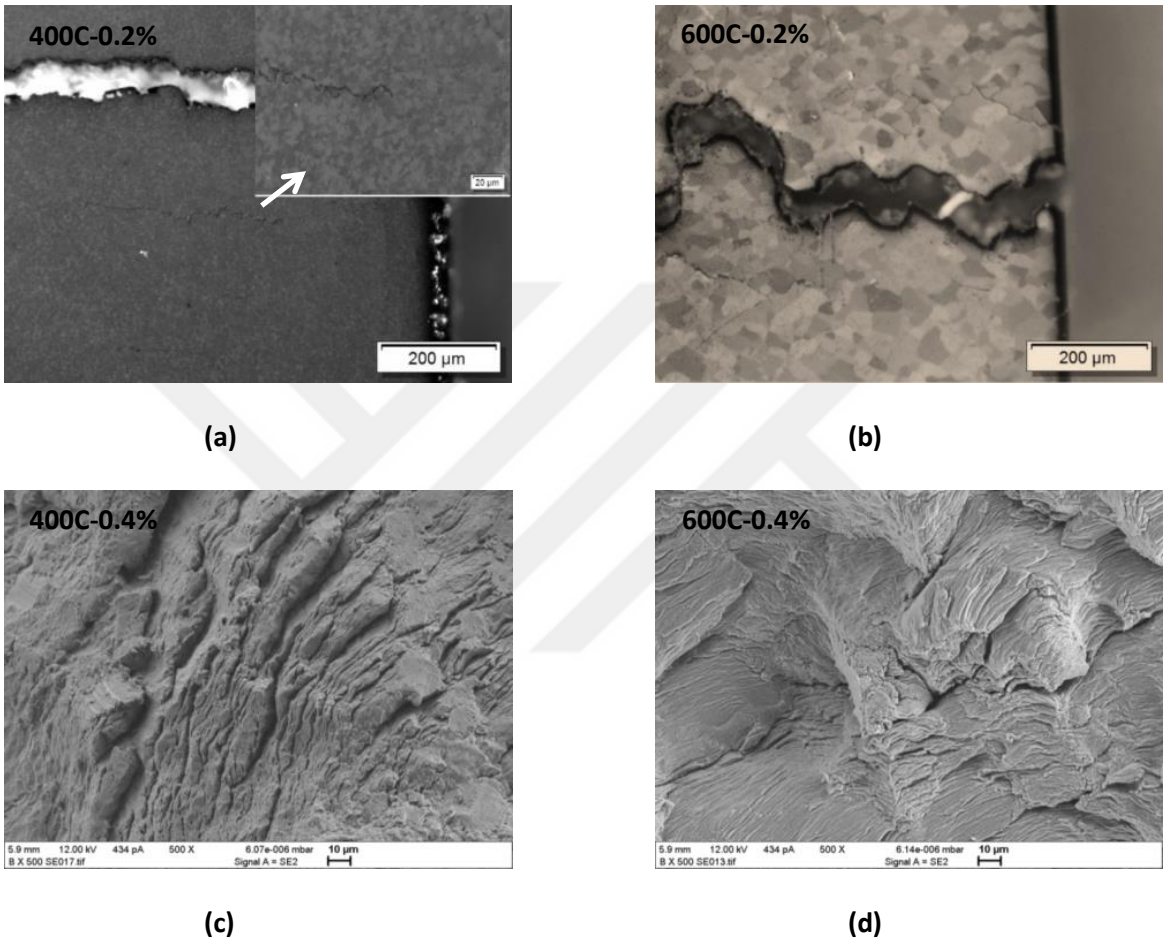

Figure 8.5 Optical micrographs of UFG Ti following cyclic loading (a) at 400^{o}C with strain amplitude of 0.2% (low and high magnifications), (b) at 600^{o}C with strain amplitude of 0.2% (Images were captured in the vicinity of cracks), fracture surfaces of sample fatigued (c) at 400^{o}C with strain amplitude of 0.4% and (d) at 600^{o}C with strain amplitude of 0.4%

EBSD images and corresponding misorientation distribution histograms of severely deformed Ti after cyclic tests at elevated temperatures are provided in Fig. 8.6. It follows from Fig. 8.6 that after cyclic deformation at 400^{o}C and for the lowest strain amplitude, microstructure of severely deformed Ti still consists of some regions with ultrafine grains which was also observed under optical microscope (Fig. 8.5a and 8.6a). However, the

sample subjected to LCF at 600^{o}C shows microstructure with remarkably large grains in comparison with those of the fatigued sample at 400°C (Fig. 8.5b and 8.6b). Grain growth occurs after completion of softening mechanisms such as static and dynamic recrystallization in order to reduce the internal energy of structure [198]. EBSD observations align well with cyclic response of UFG Ti, as mentioned in section 8.2.

Influence of strain amplitude is also studied. Interestingly, higher strain amplitude at 400^{o}C led to the formation of a bimodal microstructure which is a mixture of CG and UFG regions (Fig. 8.6c). It is well-known that high strain amplitude and moderate temperatures may result in localized grain growth in UFG microstructures [105]. These large grains cause localized damages and adversely affect cyclic stability. This argument supports the observed inferior CDR of UFG Ti at 400^{o}C with the strain amplitudes above 0.2% (Fig. 8.2a). At 600^{o}C with strain amplitude of 0.6%, grain growth took place still, due to the higher amount of strain, dynamically recrystallized grains are relatively finer than those observed at the strain amplitude of 0.2%. It was found that increasing stress levels leads to a reduction of DRX grain size at high strains [117,118].

Number fractions of each misorientation angle are also plotted versus measured misorientation angle. The grain boundaries with misorientation angle less than 15^{o} are determined as LAGBs. It is apparent that number fraction of LAGBs rises with the increase in temperature. This can be attributed to the recovery of severely deformed microstructure while they are exposed to higher temperatures [105,154]. Previously, it was confirmed that HAGBs can play a significant role in the cyclic stability of UFG materials [191]. This stability stems from the fact that HAGBs are hardly rearranged via interactions with dislocations under cyclic deformations. According to these observations,

cyclic stability due to higher volume fraction of HAGBs and UFG microstructure can be expected to be achieved in UFG Ti under cyclic loading at 400°C with strain amplitude of 0.2%. Detailed microstructural findings verify the mechanical test results that show the CDR of UFG Ti (Fig. 8.2, 8.4 and 8.6).

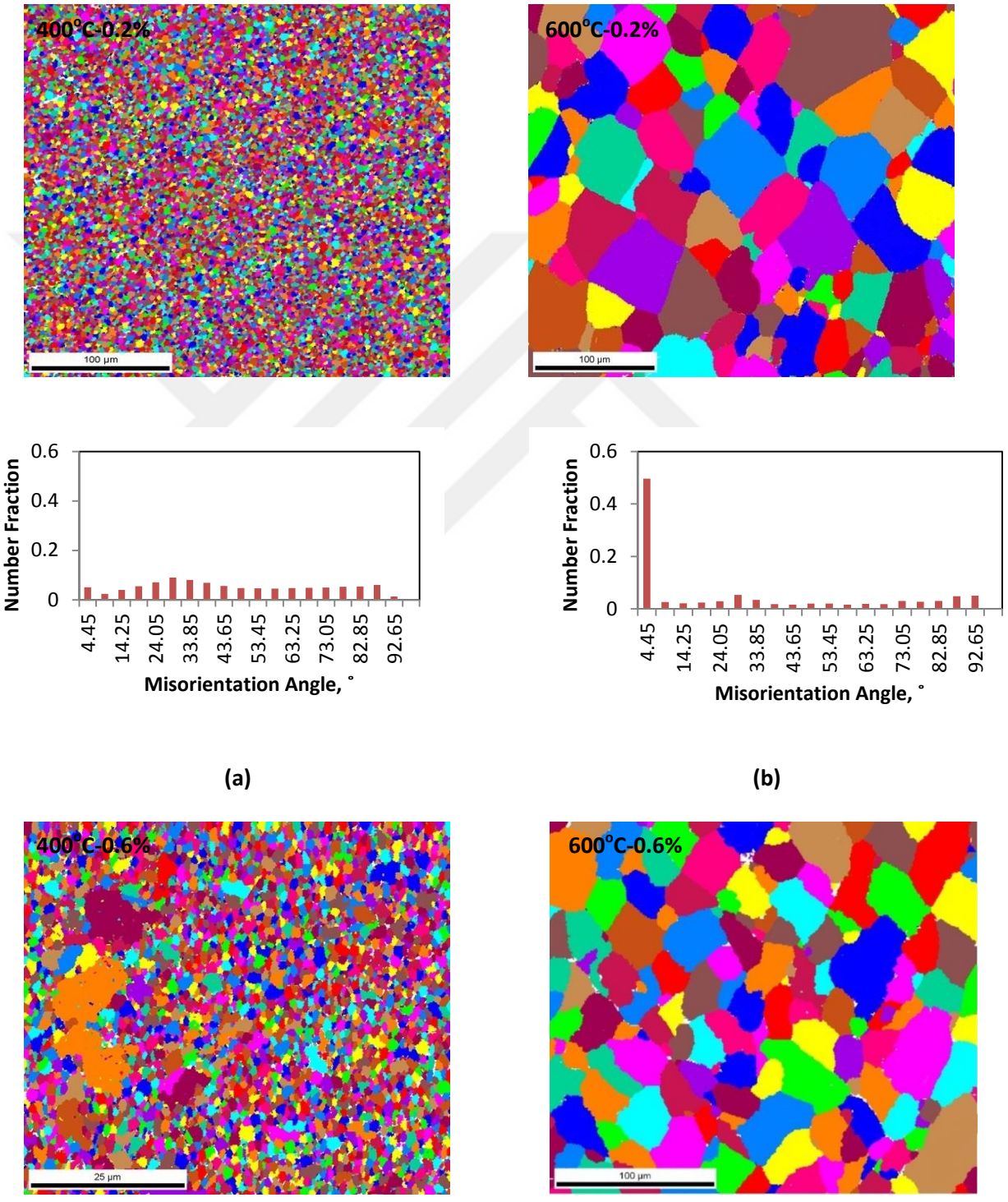

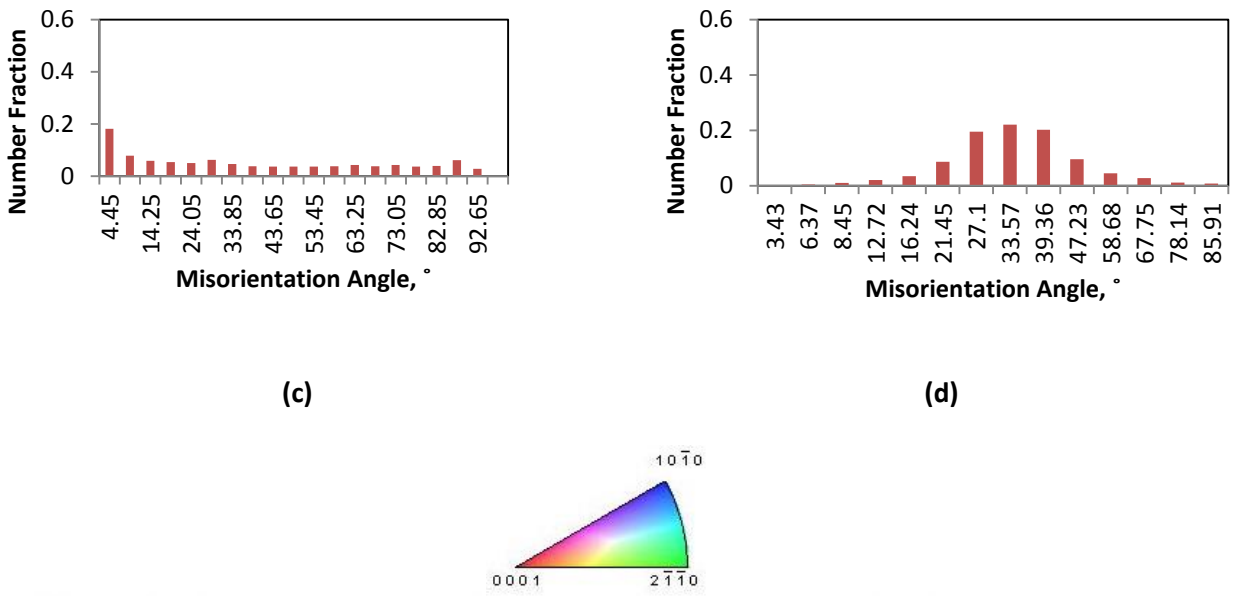

Figure 8.6 EBSD images of UFG Ti following cyclic loading at (a) 400°C with strain amplitude of 0.2% (b) 600°C with strain amplitude of 0.2% (c) 400°C with strain amplitude of 0.6% and (d) 600°C with strain amplitude of 0.6%. The corresponding misorientation distribution histograms and inverse pole figure are also shown

8.5. Effects of ECAE Route on Cyclic Behavior of CP Ti

This section focuses on the effects of two ECAE routes (E and B_c) on the CDR of CP Ti by conducting hardness and LCF experiments at various temperatures. Prior to mechanical loading, thermal stability of route-8E UFG, route-8B_c UFG and CG Ti was determined by micro-hardness measurements after annealing of specimens for 1 hour and at various temperatures (Fig. 8.7). In detail, hardness values are found to be independent of examined ECAE routes. A sharp decrease in the hardness of UFG Ti was obtained at 600°C, attesting the occurrence of recovery and recrystallization of the UFG structure at such a high temperature. Therefore, 500°C has been recognized as a limit for thermal stability of UFG CP grade 4 Ti.

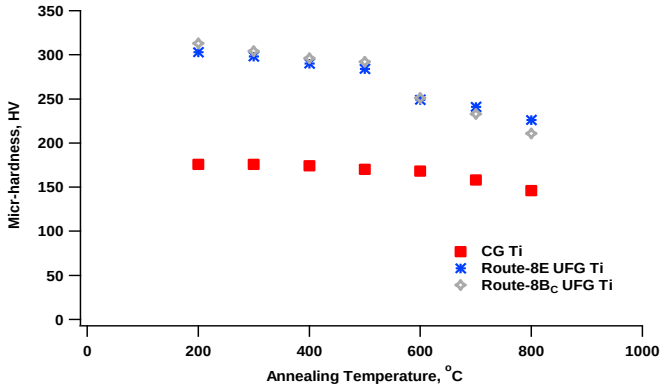

Figure 8.7 Micro-hardness evolution versus annealing temperature

Room temperature cyclic behavior of route-8E UFG, route-8B_c UFG and CG Ti are displayed in Fig. 8.8. It can be seen that the fatigue performance of UFG Ti processed via route-8E and route-8B_c surpassed that of CG Ti. A slight difference in cyclic stability of route-8E and route-8B_c UFG Ti can also be concluded from Fig. 8.8. Particularly, route-8B_c shows higher fatigue life and stress range values. This can be ascribed to the formation of higher fraction of equiaxed fine grains in materials processed via this route (route-B_c) [1].

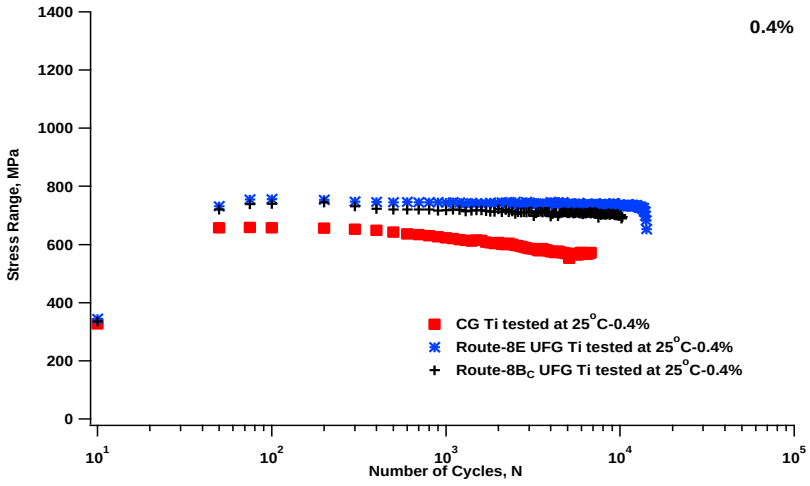

(a)

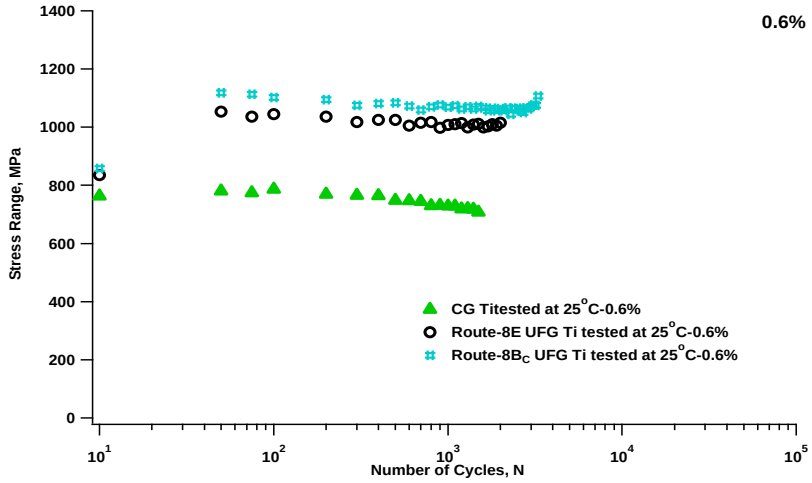

(b)

Figure 8.8 CDR of CG Ti, route-8E and route-8B_C UFG Ti at room temperature with strain amplitude of (a) 0.4% and (b) 0.6%

Shown in Fig. 8.9 are the CDR plots of route-8E UFG, route-8B_c UFG and CG Ti samples at 400°C. Fig. 8.9 demonstrates that cyclic responses of both route-8E and route-8Bc UFG Ti are similar and they exhibit stable fatigue behavior at this temperature in spite of the fact that a slight improvement in both fatigue life and stress range values was observed in route-8B_c UFG Ti at the lowest strain amplitude. During monotonic tests of UFG Ti at room temperature, route B_c also displayed a gradual increase in strength values over route E although route E was found to provide the best combination of ductility and strength [69]. At room temperature, IF steel processed via route E and B_c showed a noticeable cyclic stability despite the inferior response of materials processed via route A and C [192]. This was be attributed to the formation of equiaxed fine grains and the larger volume fraction of HAGBs in materials processed via these efficient routes (route E and B_c) [1,192]. As discussed earlier, HAGBs enhance cyclic stability leading to better fatigue performance.

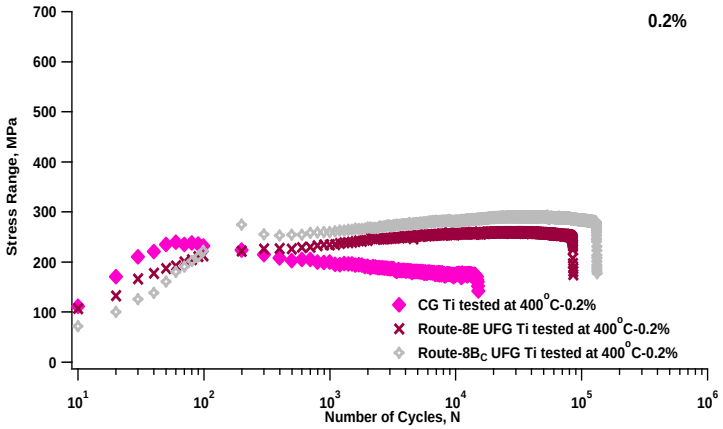

(a)

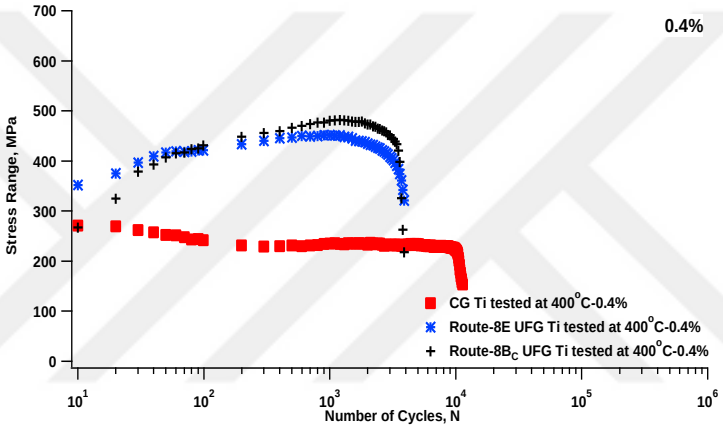

(b)

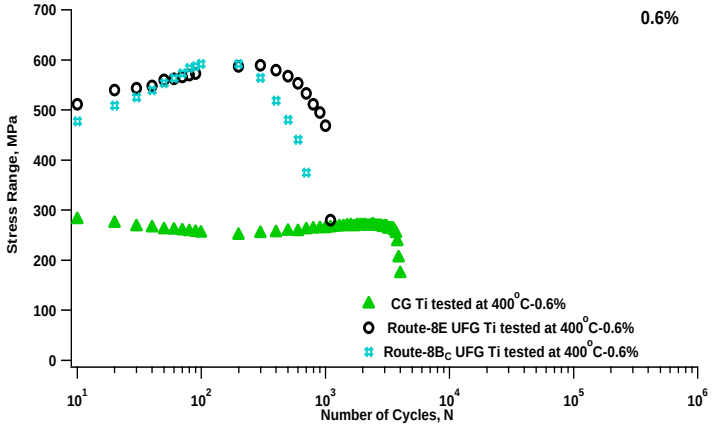

(c)

Figure 8.9 CDR of CG Ti, route-8E and route-8B_C UFG Ti at 400^{o}C with strain amplitude of (a) 0.2% (b) 0.4% and (c) 0.6%

Route-8E and route-8B_c UFG Ti did not show better CDRs over CG Ti at 600^{o}C (Fig. 8.10). Owing to the occurrence of softening mechanisms at such a high temperature, fatigue performance is degraded. Regardless of the strain amplitude, stress range levels of CG Ti are equal or slightly higher than those of route-8B_c and route-8E UFG Ti. In case of fatigue life, UFG Ti processed in both ECAE routes could not also surpass CG Ti. This confirms that the impacts of severe plastic deformation and processing routes on cyclic behavior of Ti are not significant at 600^{o}C.

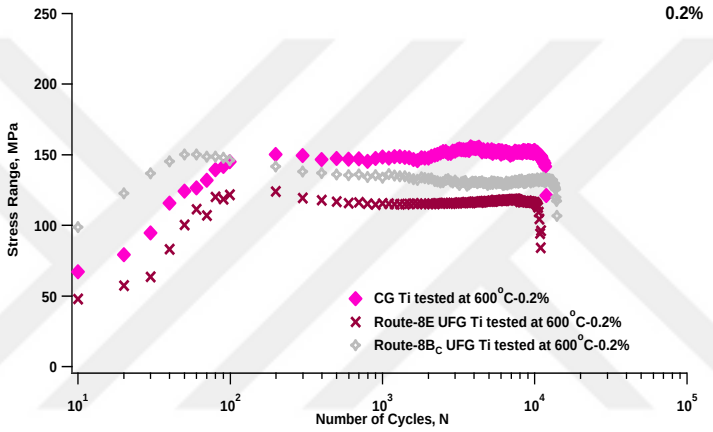

(a)

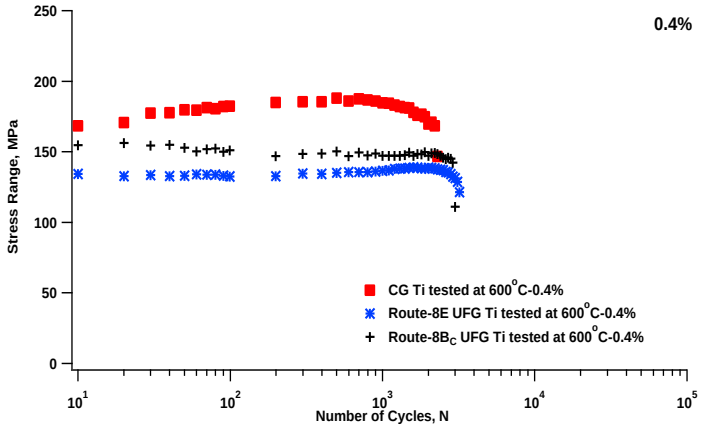

(b)

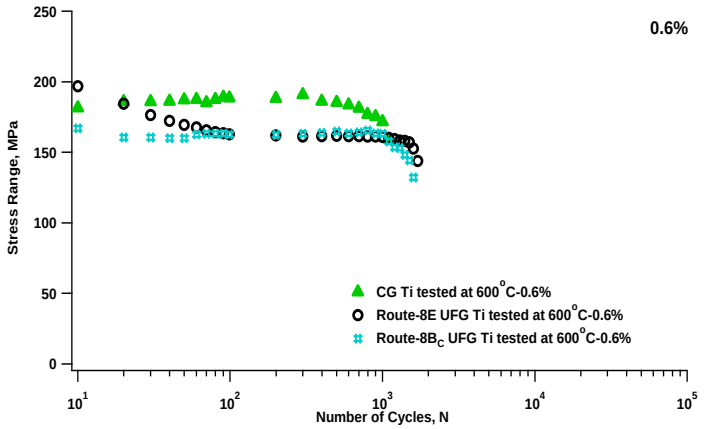

(c)

Figure 8.10 CDR of CG Ti, route-8E and route-8B$_C$ UFG Ti at 600^{o}C with strain amplitude of (a) 0.2% (b) 0.4% and (c) 0.6%

9. Effect of Severe Plastic Deformation on the Damping Properties of CP Titanium

To further investigate thermo-mechanical behavior of UFG Ti, damping capacity was also examined. Since the dislocation density and the existence of GBS are significant factors affecting the damping capacity, the influence of SPD on the damping behavior might be remarkable.

9.1. Flow stress Response

Fig. 9.1 shows the tensile stress-strain curves of CG and UFG Ti at ambient temperature and at an elevated temperature of 600^{o}C and strain rate of 0.01s^{-1}. SPD enables the improvement of the strength of CP titanium at ambient temperature in spite of a substantial loss in hardening capability. Thus, although a two-fold increase in yield strength is recorded, ultimate tensile strength rose about 30%. The increase in flow strength after SPD is attributed to the influence of the dislocation substructure and the high density of grain boundaries [121,122]. At 600^{o}C, the microstructures exhibited similar strength levels. In contrast, severely deformed Ti demonstrated a more ductile behavior than the as-received condition. This behavior could be imputed to the activation of grain boundary mediated mechanisms in addition to enhanced dislocation glide with multiple slip systems [122,172]. Grain boundary diffusion mechanisms such as GBS become operational when deformation occurs at elevated temperatures [122]. Since UFG materials possess a high fraction of boundaries and shorter path ways of diffusion, GBS may be the controlling deformation mechanism [172]. As such, in severely deformed Ti GBS is favored leading to improved ductility at 600^{o}C. In case of ductility, CG Ti showed lower elongation at 600^{o}C which can be connected with the hot embrittlement of coarse

grained structure at elevated temperature [174]. It was found that dynamic recrystallization took place in UFG structure in a higher degree, which inhibits nucleation and propagation of microvoids and cracks.

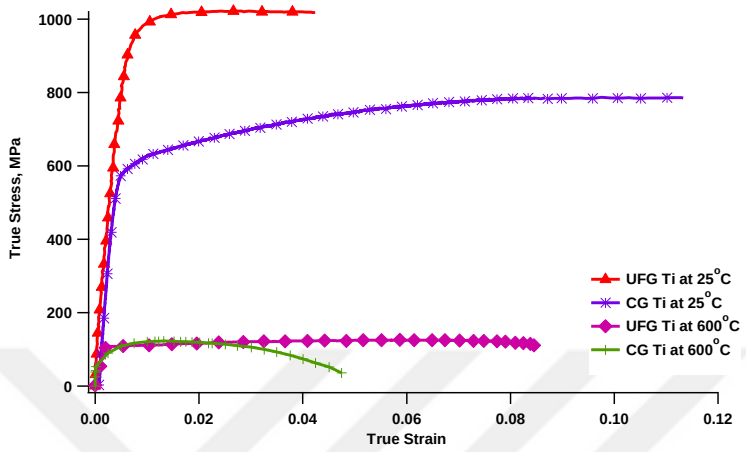

Figure 9.1 True stress–true strain response of CG and UFG Ti with strain rates of $0.01s^{-1}$ at $25^{o}C$ and at $600^{o}C$

9.2. Temperature Sweep

Variation of tan (ϕ) with temperature is an indication of the damping capacity as demonstrated in Fig. 9.2a. At ambient conditions, damping properties of both CG and UFG Ti are almost the same and vary little with increasing temperature up to $300^{o}C$. Damping capacities of both CG and UFG titanium increase drastically at elevated temperatures above $300^{o}C$. It is well documented that the thermal activation leads to a rise in the concentration of both point and line defects enhancing the interaction between dislocations and pinning obstacles [18]. Therefore, internal friction increases at higher temperatures resulting in to elevated damping capacity. It is worth mentioning that the onset of tan (ϕ) rise is observed at a comparably lower temperature for UFG Ti. Improvement in damping capacity with the drop of grain size in A356 alloy was reported by Zhang et al. [18]. This is rationalized in terms of the effects of grain boundaries and dislocations on the dissipation of elastic strain energy. A crucial outcome of SPD is the

formation of substructures with high density of dislocations and grain boundaries both of which can influence damping response as features of microstructural resistance. Moreover, damping capacity can be affected by grain boundary sliding [17]. Viscous behavior of grain boundaries during GBS and diffusion convert mechanical energy into thermal energy causing higher internal friction and consequently higher damping capacity. Therefore, grain boundary sliding can be recognized as the dominant deformation mechanism in UFG titanium at elevated temperatures [199]. These observations are also supported by the similar flow stress responses of severely deformed and CG titanium at 600^{o}C (Fig. 9.1) in contrast to the higher ductility obtained for the former.

Dynamic modulus of CG and UFG Ti as a function of temperature are displayed in Fig. 9.2b Regardless of the grain size, modulus level decreases with increasing temperature. Decrease of stiffness with the rise of temperature was previously reported for titanium and other metallic materials elsewhere [17,200,201]. This reduction in modulus is attributed to the mechanical relaxation affiliated with the atomic motion at elevated temperatures [202]. Another parameter, which requires to be studied, is the effect of grain size on the modulus. It can be seen that the stiffness of UFG Ti is slightly lower than that of CG Ti as can be explained by the fact that higher level of structural relaxation takes place in severely deformed materials [201]. It is well-established that relaxation time is proportional to the grain sizes due to the fact that grain boundary diffusion is enhanced in UFG structures [203].

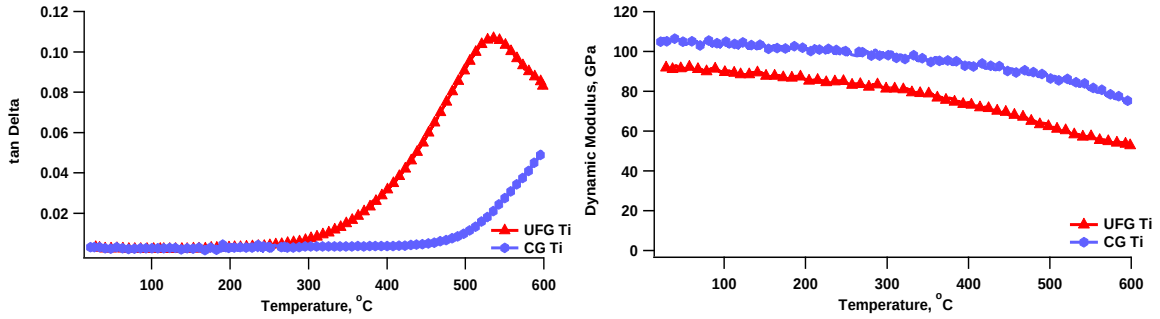

(a) (b)

Figure 9.2 The variation in (a) damping capacity and (b) dynamic modulus of CG and UFG titanium as a function of temperature at frequency of 1 Hz with strain of 0.01%

9.3. Time Sweep

For an extensive investigation on the effects of ECAE processing on damping characteristics, DMA experiments were also conducted as a function of time at ambient temperature and at 600°C in Fig. 9.3 and Fig. 9.4, respectively. The damping capacity as indicated by tan (ϕ) decreases with time and levels off to a steady value. It can be seen that the damping capacity of UFG Ti is slightly higher than that of CG Ti at a strain amplitude of 0.01%. Since high dislocation density is a common feature for severely deformed materials, higher internal friction would be expected [1]. The damping capacity of both CG and UFG Ti rose at the higher strain amplitude as linked to increased dislocation density [200]. The trend is similar at 0.05%, with a larger gap between the two microstructural states. This can be due to the higher dislocation density and high angle grain boundary fraction in severely deformed materials as compared to coarse microstructures.

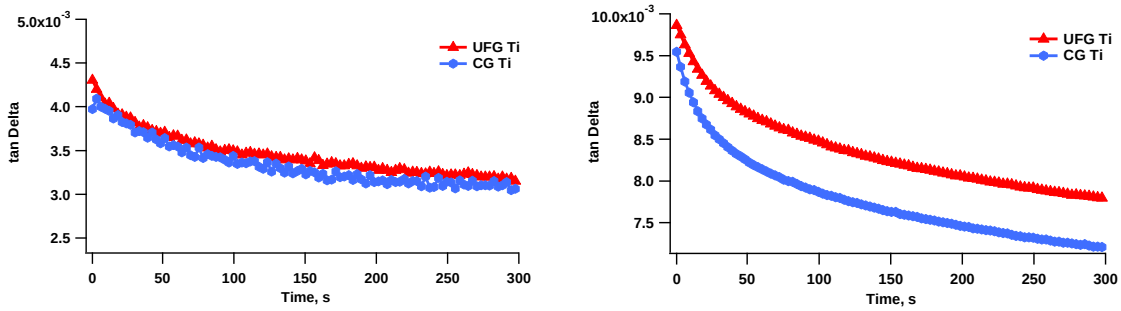

(a) (b)

Figure 9.3 Damping capacity of CG and UFG Ti as a function of time at room temperature with strain amplitude of (a) 0.01% and (b) 0.05%

Enhancement of damping capacity after SPD is also clear for 600^{o}C as displayed in Fig. 9.4. As opposed to observations at ambient temperature (Fig. 9.3), damping capacity of both CG and UFG Ti are almost time independent. Time independency of damping capacity can be related to the dislocation annihilations at such a high temperature (600^{o}C) [201,204].

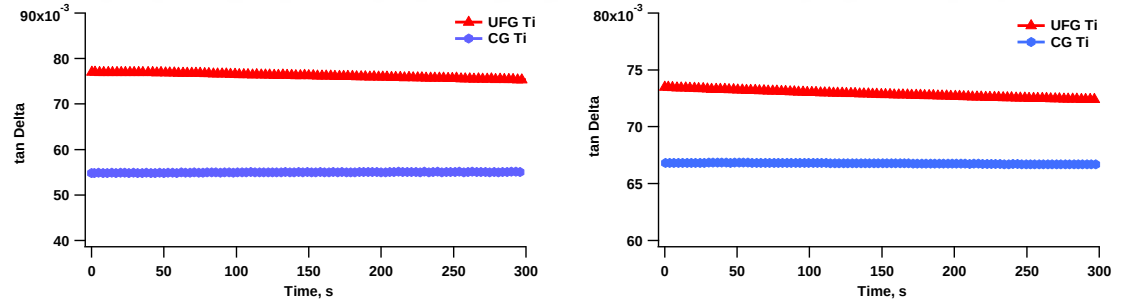

(a) (b)

Figure 9.4 Damping capacity of CG and UFG Ti as a function of time at 600oC with strain amplitude of (a) 0.01% and (b) 0.05%

10. Summary and Conclusions

In the current investigation, it was seen that SPD processing could enhance the mechanical properties of titanium at elevated temperatures. The deformation and workability characteristics, high temperature mechanical behavior, flow response modeling, effect of purity levels on the high-temperature deformation characteristics and damping capacity of severely deformed pure Ti were studied at various deformation conditions in the warm to hot working regime. The following conclusions can be drawn.

Before and during elevated temperature testing, grain growth occurred in the UFG microstructure obtained after ECAE. The mechanical properties of ECAE processed CP titanium at elevated temperatures depend on both deformation temperature and strain rate. Higher flow stress levels are demonstrated with the increase in strain rate and the decrease in deformation temperature. Comparison of severely deformed and annealed grade 2 Ti samples demonstrated that ECAE could enhance the hot strength of CP titanium with close to 50% increase in steady flow stress levels at temperatures as high as 600^{o}C. Moreover, the severely deformed microstructure is altered with the post-ECAE deformation temperature leading to significant grain coarsening, especially at or above 700^{o}C. The high temperature strain rate sensitivity of severely deformed pure Ti was seen to be strongly temperature dependent. The tendency for localized flow was probed by determining the flow localization parameter for all testing conditions. Accordingly, the workability at elevated temperatures is satisfactory at 800^{o}C and above. From a metal forming perspective in the high temperature regime, deformation over 700^{o}C could be preferred due to comparably lower amount of flow localization.

Three modeling approaches used in the current research work demonstrated stress-strain curves with reasonable agreement in the examined strain rate and temperature range. In this range, the error levels on stress predictions remained less than 10%. For temperatures above 600^{o}C, the dislocation density based model should be preferred; whereas below 600^{o}C, the model based on the Arrhenius formulation revealed a better agreement. The modified Johnson Cook model was also utilized to predict the flow behavior of ECAE processed pure Ti. For this model, the highest error level to remain less than 5%, pointing to the probable use of the presented model in predicting the compressive response of ECAE processed Ti at elevated temperatures.

High-temperature flow characteristics of ECAE processed titanium with varying purity levels by underlining the similar and contrasting features was investigated. While higher flow stress levels were obtained for grade 2 at the lower end of the deformation temperature range; grade 4 exhibited higher strength at higher temperatures. These tendencies were supported by microstructural observations since grain growth rate was seen to be higher in grade 4 titanium at lower deformation temperatures below 700^{o}C. Before and during elevated temperature testing, grain growth occurred in the severely deformed UFG microstructures of both grades. While grade 2 was more stable at lower deformation temperatures up to 700^{o}C, grade 4 showed higher stability at higher deformation temperatures over 700^{o}C. Grain boundary bulging was asserted as a possible mechanism for dDRX during hot deformation. After SPD, flow stress levels of both CP grades in the UFG state were higher than those of CG counterparts at 600^{o}C strained at a rate of 0.1s^{-1}. The difference between the flow stress levels of severely deformed samples and their CG counterparts was seen to be higher for grade 2 which could be attributed to its lower processing temperature.

By performing hot compression tests on grade 2 and grade 4 Ti after SPD, it was uncovered that severely deformed grade 4 Ti was less stable at examined temperatures. Thus, the warm deformation behavior and microstructure evolution of severely deformed grade 4 titanium were studied at temperatures of 300-600^{o}C and at strain rates of 0.001-0.1s^{-1}. Mechanical properties and microstructural observations showed high thermal stability against coarsening up to 500^{o}C (T_h=0.40). In contrast, grain growth stemmed from grain boundary migration occurs at or above 500^{o}C. At the highest deformation temperature (600^{o}C), thermal stability of severely deformed titanium was also sensitive to the rate of deformation. Studies on fracture surfaces revealed that ductile fracture took place at the examined strain rate and temperature range. Higher deformation temperature and lower strain rate led to high tendency of void growth and coalescence.

CDRs and cyclic stability of severely deformed pure Ti were studied at room and elevated temperatures (up to 600^{o}C) and at various strain amplitudes. Influences of route-8E and route-8Bc on the fatigue behavior of CP Ti were explored. LCF responses imply that ECAE processing is capable of improving the fatigue performance of CP Ti up to 400^{o}C (T_h=0.35). For temperatures above 400^{o}C, cyclic stability of severely deformed Ti is replaced with shorter fatigue lives and lower stress range levels. This behavior is associated with annihilation and grain growth of the UFG microstructure. Symmetric hysteresis loops were achieved for LCF experiments of UFG and CG Ti. The amount of energy dissipation of UFG Ti was lower than that of CG Ti at or below 400^{o}C, attesting better fatigue performance of UFG materials at these temperatures. Volume fraction of LAGBs was seen to increase with the rise of temperature. LAGBs are prone to rearrangement when dislocations interact with them under cyclic deformations, which adversely affect the cyclic stability. Fatigue behavior of route-8E and route-8Bc UFG Ti

appeared to be similar although materials processed via route B_c showed higher fatigue life and stress range values at 400^{o}C with a strain amplitude of 0.2%.

Regarding the damping behavior, damping capacity of titanium rose noticeably at elevated temperatures up to 600^{o}C irrespective to the grain size. This could be attributed to the increase in concentration of both point and line defects. Damping capacity of UFG titanium was seen to be greater than its CG counterpart. Grain boundary damping was asserted as the main reason for this difference. Damping properties of UFG Ti as a function of time also surpassed its CG counterpart. Damping capacity of both CG and UFG Ti tended to decrease with increase of time at room temperature while it remained constant with time at 600^{o}C.

11. Recommendations for Future Work

Although some efforts were made to study thermo-mechanical processing of CP Ti in the present work, these methods are not limited to the performed experiments and achieved findings. Therefore, there are few suggestions for upcoming research projects.

Severely deformed CP Ti was investigated by the use of monotonic and cyclic experiments at various temperatures. LCF tests were utilized to monitor cyclic behavior of this material. However, high cycle fatigue (HCF) experiments were not conducted on this material. Previously, researchers probed HCF response of both CG and UFG Ti at ambient temperature. Lack of discussion on HCF response of severely deformed Ti at elevated temperature may motivate researchers to consider this topic of interest.

Other SPD techniques such as ARB, HPT can also be applied on CP Ti. There are some studies reporting microstructure evolution and changes in the mechanical properties of CP Ti at room temperature. Among those research efforts, there is no report on the elevated temperature behavior of severely deformed Ti fabricated by aforementioned SPD techniques.

Another investigation may focus on the changes in the mechanical properties of titanium alloys after ECAE process. Elevated temperature characteristics of severely deformed Ti alloys can be another topic of interest to complete this field of study.

References

[1] V. V Stolyarov, Y.T. Zhu, I. V Alexandrov, T.C. Lowe, R.Z. Valiev, Influence of ECAP routes on the microstructure and properties of pure Ti, Mater. Sci. Eng. A. 299 (2001) 59–67. doi:10.1016/S0921-5093(00)01411-8.

[2] Z. Fan, H. Jiang, X. Sun, J. Song, X. Zhang, C. Xie, Microstructures and mechanical deformation behaviors of ultrafine-grained commercial pure (grade 3) Ti processed by two-step severe plastic deformation, Mater. Sci. Eng. A. 527 (2009) 45–51. doi:10.1016/j.msea.2009.07.030.

[3] G.G. Yapici, I. Karaman, H.J. Maier, Mechanical flow anisotropy in severely deformed pure titanium, Mater. Sci. Eng. A. 434 (2006) 294–302. doi:10.1016/j.msea.2006.06.082.

[4] S. Faghihi, F. Azari, A.P. Zhilyaev, J.A. Szpunar, H. Vali, M. Tabrizian, Cellular and molecular interactions between MC3T3-E1 pre-osteoblasts and nanostructured titanium produced by high-pressure torsion, Biomaterials. 28 (2007) 3887–3895. doi:10.1016/j.biomaterials.2007.05.010.

[5] J.C. Fonseca, G.E.P. Henriques, L.C. Sobrinho, M.F. de Góes, Stress-relieving and porcelain firing cycle influence on marginal fit of commercially pure titanium and titanium-aluminum-vanadium copings., Dent. Mater. 19 (2003) 686–91. http://www.ncbi.nlm.nih.gov/pubmed/12901996 (accessed January 19, 2017).

[6] C.N. Elias, M.A. Meyers, R.Z. Valiev, S.N. Monteiro, Ultrafine grained titanium for biomedical applications: An overview of performance, J. Mater. Res. Technol. 2 (2013) 340–350. doi:10.1016/j.jmrt.2013.07.003.

[7] A. V Polyakov, I.P. Semenova, R.Z. Valiev, High fatigue strength and enhanced biocompatibility of UFG CP Ti for medical innovative applications, IOP Conf. Ser. Mater. Sci. Eng. 63 (2014) 12113. doi:10.1088/1757-899X/63/1/012113.

[8] Z.J. Zhang, I.H. Son, Y.T. Im, J.K. Park, Finite element analysis of plastic deformation of CP-Ti by multi-pass equal channel angular extrusion at medium hot-working temperature, Mater. Sci. Eng. A. 447 (2007) 134–141. doi:10.1016/j.msea.2006.10.068.

[9] E.I. Poliak, J.J. Jonas, A one-parameter approach to determining the critical conditions for the initiation of dynamic recrystallization, Acta Mater. 44 (1996) 127–136. doi:10.1016/1359-6454(95)00146-7.

[10] H.J. McQueen, Development of dynamic recrystallization theory, Mater. Sci. Eng. A. 387 (2004) 203–208. doi:10.1016/j.msea.2004.01.064.

[11] Z. Zeng, Y. Zhang, S. Jonsson, Deformation behaviour of commercially pure titanium during simple hot compression, Mater. Des. 30 (2009) 3105–3111. doi:10.1016/j.matdes.2008.12.002.

[12] C. XU, W. ZHU, Transformation mechanism and mechanical properties of commercially pure titanium, Trans. Nonferrous Met. Soc. China. 20 (2010) 2162–2167. doi:10.1016/S1003-6326(09)60436-2.

[13] M.J. Tan, X.J. Zhu, Dynamic recrystallization in commercially pure titanium, J. Achiev. Mater. Manuf. Eng. . 18 (2006) 183–186.

[14] M.J. Tan, X.J. Zhu, Microstructure evolution of CP titanium during high temperature deformation, Arch. Mater. Sci. Eng. 28 (2007) 5–11.

[15] Z. Zeng, S. Jonsson, Y. Zhang, Constitutive equations for pure titanium at elevated temperatures, Mater. Sci. Eng. A. 505 (2009) 116–119. doi:10.1016/j.msea.2008.11.017.

[16] L.C. Tsao, H.Y. Wu, J.C. Leong, C.J. Fang, Flow stress behavior of commercial pure titanium sheet during warm tensile deformation, Mater. Des. 34 (2012) 179–184. doi:10.1016/j.matdes.2011.07.060.

[17] H. Watanabe, T. Mukai, M. Sugioka, K. Ishikawa, Elastic and damping properties from room temperature to 673 K in an AZ31 magnesium alloy, Scr. Mater. 51 (2004) 291–295. doi:10.1016/j.scriptamat.2004.04.032.

[18] Y. Zhang, N. Ma, Y. Le, S. Li, H. Wang, Mechanical properties and damping capacity after grain refinement in A356 alloy, 2005. doi:10.1016/j.matlet.2005.02.058.

[19] B. Altan, Severe plastic deformation : toward bulk production of nanostructured materials, Nova Science, 2006.

[20] R.Z. Valiev, Recent Developments of SPD Processing for Fabrication of Bulk Nanostructured Materials, Mater. Sci. Forum. 426–432 (2003) 237–244. doi:10.4028/www.scientific.net/MSF.426-432.237.

[21] R.. Valiev, R.. Islamgaliev, I.. Alexandrov, Bulk nanostructured materials from severe plastic deformation, Prog. Mater. Sci. 45 (2000) 103–189. doi:10.1016/S0079-6425(99)00007-9.

[22] U. Erb, Electrodeposited nanocrystals: Synthesis, properties and industrial applications, Nanostructured Mater. 6 (1995) 533–538. doi:10.1016/0965-9773(95)00114-X.

[23] F. Ebrahimi, Q. Zhai, D. Kong, Deformation and fracture of electrodeposited copper, Scr. Mater. 39 (1998) 315–321. doi:10.1016/S1359-6462(98)00164-X.

[24] M. Haouaoui, I. Karaman, K.T. Harwig, H.J. Maier, Microstructure evolution and mechanical behavior of bulk copper obtained by consolidation of micro- and nanopowders using equal-channel angular extrusion, Metall. Mater. Trans. A. 35 (2004) 2935–2949. doi:10.1007/s11661-004-0241-2.

[25] I. V. Alexandrov, R.K. Islamgaliev, R.Z. Valiev, Y.T. Zhu, T.C. Lowe, Microstructures and properties of nanocomposites obtained through SPTS consolidation of powders, Metall. Mater. Trans. A. 29 (1998) 2253–2260. doi:10.1007/s11661-998-0103-4.

[26] G.W. Nieman, J.R. Weertman, R.W. Siegel, Microhardness of nanocrystalline palladium and copper produced by inert-gas condensation, Scr. Metall. 23 (1989) 2013–2018. doi:10.1016/0036-9748(89)90223-8.

[27] P.G. Sanders, G.E. Fougere, L.J. Thompson, J.A. Eastman, J.R. Weertman, Improvements in the synthesis and compaction of nanocrystalline materials, Nanostructured Mater. 8 (1997) 243–252. doi:10.1016/S0965-9773(97)00167-0.

[28] H.J. Fecht, Nanophase Materials by Mechanical Attrition: Synthesis and Characterization, in: Nanophase Mater., Springer Netherlands, Dordrecht, 1994: pp. 125–144. doi:10.1007/978-94-011-1076-1_18.

[29] H.J. Fecht, E. Hellstern, Z. Fu, W.L. Johnson, Nanocrystalline metals prepared by high-energy ball milling, Metall. Trans. A. 21 (1990) 2333–2337. doi:10.1007/BF02646980.

[30] C.C. Koch, Synthesis of nanostructured materials by mechanical milling: problems and opportunities, Nanostructured Mater. 9 (1997) 13–22. doi:10.1016/S0965-9773(97)00014-7.

[31] G. Purcek, I. Karaman, G.G. Yapici, M. Al-Maharbi, T. Kuçukomeroglu, O. Saray, Enhancement in mechanical behavior and wear resistance of severe plastically deformed two-phase Zn–Al alloys, Int. J. Mater. Res. 98 (2007) 332–338. doi:10.3139/146.101470.

[32] M. Aliofkhazraei, Handbook of mechanical nanostructuring, n.d.

[33] C.T. Wang, N. Gao, M.G. Gee, R.J.K. Wood, T.G. Langdon, Effect of grain size on the micro-tribological behavior of pure titanium processed by high-pressure torsion, Wear. 280 (2012) 28–35. doi:10.1016/j.wear.2012.01.012.

[34] R.Z. Valiev, T.G. Langdon, Principles of equal-channel angular pressing as a processing tool for grain refinement, Prog. Mater. Sci. 51 (2006) 881–981. doi:10.1016/j.pmatsci.2006.02.003.

[35] V.M. Segal, Materials processing by simple shear, Mater. Sci. Eng. A. 197 (1995) 157–164. doi:10.1016/0921-5093(95)09705-8.

[36] V.M. Segal, Equal channel angular extrusion: from macromechanics to structure formation, Mater. Sci. Eng. A. 271 (1999) 322–333. doi:10.1016/S0921-5093(99)00248-8.

[37] R.E. Barber, T. Dudo, P.B. Yasskin, K.T. Hartwig, Product yield for ECAE processing, Scr. Mater. 51 (2004) 373–377. doi:10.1016/j.scriptamat.2004.05.022.

[38] L.R. Cornwall, K.T. Hartwig, R.E. Goforth, S.L. Semiatin, The equal channel angular

extrusion process for materials processing, Mater. Charact. 37 (1996) 295–300. doi:10.1016/S1044-5803(97)80018-6.

[39] P.B. Berbon, M. Furukawa, Z. Horita, M. Nemoto, T.G. Langdon, Influence of pressing speed on microstructural development in equal-channel angular pressing, Metall. Mater. Trans. A. 30 (1999) 1989–1997. doi:10.1007/s11661-999-0009-9.

[40] G.G. Yapici, Investigation and modeling of processing-microstructure-property relations in ultra-fine grained hexagonal close packed materials under strain path changes, 2007.

[41] D.S. Landes, The unbound Prometheus: technological change and industrial development in Western Europe from 1750 to the present, 1969.

[42] J.M. Swank, History of the Manufacture of Iron in All Ages : And Particularly in the United States from Colonial Time to 1891, Cambridge University Press, 2011.

[43] S.L. Semiatin, ASM Handbook Committee., Forming and forging, ASM International, 1993.

[44] S. Kalpakjian, S. Schmid, Manufacturing engineering and technology, Addison-Wesley, 1989.

[45] M.A. Meyers, K.K. Chawla, Mechanical behavior of materials, Cambridge University Press, 2009.

[46] E. Orowan, Symposium on Internal Stresses in Metals and Alloys, in: Institute of Metals, London, 1948: pp. 451–453. https://books.google.com.tr/books/about/Symposium_on_Internal_Stresses_in_Metals.html?id=_Jr1DerDuY0C&redir_esc=y (accessed January 27, 2017).

[47] C. Leyens, M. Peters, Titanium and Titanium Alloys, Wiley-VCH, Koln, 2003.

[48] C.J. (Colin J. Smithells, E.A. (Eric A. Brandes, G.B. Brook, Smithells light metals handbook, Butterworth-Heinemann, 1998.

[49] K.L. Luthra, Stability of protective oxide films on Ti-base alloys, Oxid. Met. 36 (1991) 475–490. doi:10.1007/BF01151593.

[50] J.R. Nicholls, J. Leggett, P. Andrews, Hot Salt Corrosion of titanium aluminides, Mater. Corros. Und Korrosion. 48 (1997) 56–64. doi:10.1002/maco.19970480110.

[51] C.N. Elias, J.H.C. Lima, R. Valiev, M.A. Meyers, Biomedical applications of titanium and its alloys, JOM. 60 (2008) 46–49. doi:10.1007/s11837-008-0031-1.

[52] L.C. Campanelli, L.T. Duarte, P.S.C.P. da Silva, C. Bolfarini, Fatigue behavior of modified surface of Ti–6Al–7Nb and CP-Ti by micro-arc oxidation, 2014. doi:10.1016/j.matdes.2014.07.074.

[53] J. Peng, C.-Y. Zhou, Q. Dai, X.-H. He, Dwell fatigue and cycle deformation of CP-Ti at ambient temperature, Mater. Des. 71 (2015) 1–16. doi:10.1016/j.matdes.2015.01.007.

[54] W. Chen, C.J. Boehlert, The elevated-temperature fatigue behavior of boron-modified Ti–6Al–4V(wt.%) castings, Mater. Sci. Eng. A. 494 (2008) 132–138. doi:10.1016/j.msea.2008.04.004.

[55] A. Cremasco, E.S.N. Lopes, F.F. Cardoso, R.J. Contieri, I. Ferreira, R. Caram, Effects of the microstructural characteristics of a metastable β Ti alloy on its corrosion fatigue properties, Int. J. Fatigue. 54 (2013) 32–37. doi:10.1016/j.ijfatigue.2013.04.010.

[56] M.R. Bache, W.J. Evans, B. Suddell, F.R.M. Herrouin, The effects of texture in titanium alloys for engineering components under fatigue, Int. J. Fatigue. 23 (2001) 153–159. doi:10.1016/S0142-1123(01)00124-4.

[57] G.E. Dieter, Mechanical metallurgy, McGraw-Hill, 1986.

[58] E.O. Hall, The Deformation and Ageing of Mild Steel: III Discussion of Results, Proc. Phys. Soc. Sect. B. 64 (1951) 747–753. doi:10.1088/0370-1301/64/9/303.

[59] N. J. Petch, The Cleavage Strength of Polycrystals, J. Iron Steel Inst. 174 (1953) 25–28.

[60] G. Purcek, O. Saray, M.I. Nagimov, A.A. Nazarov, I.M. Safarov, V.N. Danilenko, O.R. Valiakhmetov, R.R. Mulyukov, Microstructure and mechanical behavior of UFG copper processed by ECAP following different processing regimes, Philos. Mag. 92 (2012) 690–704. doi:10.1080/14786435.2011.634842.

[61] F. Kümmel, T. Hausöl, H.W. Höppel, M. Göken, Enhanced fatigue lives in AA1050A/AA5005 laminated metal composites produced by accumulative roll bonding, Acta Mater. 120 (2016) 150–158. doi:10.1016/j.actamat.2016.08.039.

[62] P. Behjati, A. Kermanpur, A. Najafizadeh, H. Samaei Baghbadorani, J.-G. Jung, Y.-K. Lee, Enhanced mechanical properties in a high-manganese austenitic steel through formation of nano grains, nanotwinned austenite grains, nano carbides and TRIP, Mater. Sci. Eng. A. 610 (2014) 273–278. doi:10.1016/j.msea.2014.05.015.

[63] M. Eizadjou, H.D. Manesh, K. Janghorban, Microstructure and mechanical properties of ultra-fine grains (UFGs) aluminum strips produced by ARB process, J. Alloys Compd. 474 (2009) 406–415. doi:10.1016/j.jallcom.2008.06.161.

[64] C.T. Wang, N. Gao, M.G. Gee, R.J.K. Wood, T.G. Langdon, Processing of an ultrafine-grained titanium by high-pressure torsion: An evaluation of the wear properties with and without a TiN coating, J. Mech. Behav. Biomed. Mater. 17 (2013) 166–175. doi:10.1016/j.jmbbm.2012.08.018.

[65] J.L. Milner, F. Abu-Farha, C. Bunget, T. Kurfess, V.H. Hammond, Grain refinement and mechanical properties of CP-Ti processed by warm accumulative roll bonding, Mater. Sci. Eng. A. 561 (2013) 109–117. doi:10.1016/j.msea.2012.10.081.

[66] I. Sabirov, R.Z. Valiev, I.P. Semenova, R. Pippan, Effect of Equal Channel Angular Pressing on the Fracture Behavior of Commercially Pure Titanium, Metall. Mater. Trans. A. 41 (2010) 727–733. doi:10.1007/s11661-009-0111-z.

[67] V.L. Sordi, M. Ferrante, M. Kawasaki, T.G. Langdon, Microstructure and tensile strength of grade 2 titanium processed by equal-channel angular pressing and by rolling, J. Mater. Sci. 47 (2012) 7870–7876. doi:10.1007/s10853-012-6593-x.

[68] A. Chlupová, J. Man, I. Kuběna, J. Polák, L.P. Karjalainen, LCF Behaviour of Ultrafine Grained 301LN Stainless Steel, Procedia Eng. 74 (2014) 147–150. doi:10.1016/j.proeng.2014.06.239.

[69] T. Niendorf, D. Canadinc, H.J. Maier, I. Karaman, G.G. Yapici, Microstructure–mechanical property relationships in ultrafine-grained NbZr, Acta Mater. 55 (2007) 6596–6605. doi:10.1016/j.actamat.2007.08.015.

[70] S. Malekjani, P.D. Hodgson, P. Cizek, I. Sabirov, T.B. Hilditch, Cyclic deformation response of UFG 2024 Al alloy, Int. J. Fatigue. 33 (2011) 700–709. doi:10.1016/j.ijfatigue.2010.11.025.

[71] X.H. An, S.D. Wu, Z.G. Wang, Z.F. Zhang, Enhanced cyclic deformation responses of ultrafine-grained Cu and nanocrystalline Cu–Al alloys, Acta Mater. 74 (2014) 200–214. doi:10.1016/j.actamat.2014.04.053.

[72] H.W. Höppel, M. Göken, 17 – Fatigue behaviour in nanostructured metals, in: Nanostructured Met. Alloy., 2011: pp. 507–541. doi:10.1533/9780857091123.3.507.

[73] T. Niendorf, D. Canadinc, H.J. Maier, I. Karaman, The role of grain size and distribution on the cyclic stability of titanium, Scr. Mater. 60 (2009) 344–347. doi:10.1016/j.scriptamat.2008.10.033.

[74] I.P. Semenova, G.K. Salimgareeva, V.V. Latysh, T. Lowe, Enhanced fatigue strength of commercially pure Ti processed by severe plastic deformation, Mater. Sci. Eng. A. 503 (2009) 92–95. doi:10.1016/j.msea.2008.07.075.

[75] A.Y. Vinogradov, V.V. Stolyarov, S. Hashimoto, R.Z. Valiev, Cyclic behavior of ultrafine-grain titanium produced by severe plastic deformation, Mater. Sci. Eng. A. 318 (2001) 163–173. doi:10.1016/S0921-5093(01)01262-X.

[76] H. Kitahara, K. Uchikado, J. Makino, N. Iida, M. Tsushida, N. Tsuji, S. Ando, H. Tonda, Fatigue Crack Propagation Behavior in Commercial Purity Ti Severely Deformed by Accumulative Roll Bonding Process, Mater. Trans. 49 (2008) 64–68. doi:10.2320/matertrans.ME200716.

[77] W.-J. Kim, C.-Y. Hyun, H.-K. Kim, Fatigue strength of ultrafine-grained pure Ti after severe plastic deformation, Scr. Mater. 54 (2006) 1745–1750. doi:10.1016/j.scriptamat.2006.01.042.

[78] L. Kunz, P. Lukáš, M. Svoboda, Fatigue strength, microstructural stability and strain localization in ultrafine-grained copper, Mater. Sci. Eng. A. 424 (2006) 97–104. doi:10.1016/j.msea.2006.02.029.

[79] H. Hoppel, M. Kautz, C. Xu, M. Murashkin, T. Langdon, R. Valiev, H. Mughrabi, An overview: Fatigue behaviour of ultrafine-grained metals and alloys, Int. J. Fatigue. 28 (2006) 1001–1010. doi:10.1016/j.ijfatigue.2005.08.014.

[80] H.J. McQueen, W.A. Wong, J.J. Jonas, Deformation of aluminium at high temperatures and strain rates, Can. J. Phys. 45 (1967) 1225–1234. doi:10.1139/p67-091.

[81] McG. Tegart, ed., Deformation under hot working conditions; proceedings of the conference on “Deformation under hot working conditions” held at the Department of Metallurgy, University of Sheffield, on 5 and 6 July 1966;, Iron & Steel Institute, London, 1968.

[82] H.J. McQueen, Deformation mechanisms in hot working, JOM. 20 (1968) 31–38. doi:10.1007/BF03378692.

[83] J.J. Jonas, C.M. Sellars, W.J.M. Tegart, Strength and structure under hot-working conditions, Metall. Rev. 14 (1969) 1–24. doi:10.1179/mtlr.1969.14.1.1.

[84] V.K. Lindroos, H.M. Miekk-oja, Knitting of dislocation networks by means of stress-induced climb in an aluminium-magnesium alloy, Philos. Mag. 17 (1968) 119–133. doi:10.1080/14786436808218185.

[85] M.J. Luton, W.J.M. Tegart, Fracture Behaviour of Nickel and Nickel–Iron Alloys under Hot-Working Conditions, Met. Sci. J. 3 (1969) 142–146.

doi:10.1179/msc.1969.3.1.142.

[86] H.J. McQueen, J.J. Jonas, Hot Workability Testing Techniques, in: Met. Form. Interrelat. Between Theory Pract., Springer US, Boston, MA, 1971: pp. 393–428. doi:10.1007/978-1-4615-1757-3_18.

[87] C.M. Sellars, W.J.M. Tegart, Hot Workability, Int. Metall. Rev. 17 (1972) 1–24. doi:10.1179/imtlr.1972.17.1.1.

[88] H.J. McQueen, The production and utility of recovered dislocation substructures, Metall. Trans. A. 8 (1977) 807–824. doi:10.1007/BF02661562.

[89] C.M. Sellars, Recrystallization of Metals during Hot Deformation, Philos. Trans. R. Soc. London A Math. Phys. Eng. Sci. 288 (1978).

[90] H.J. Mcqueen, J.J. Jonas, Recent advances in hot working: Fundamental dynamic softening mechanisms, J. Appl. Metalwork. 3 (1984) 233–241. doi:10.1007/BF02833651.

[91] D. Banabic, H.-J. Bunge, K. Pöhlandt, A.E. Tekkaya, Formability of Metallic Materials, Springer Berlin Heidelberg, Berlin, Heidelberg, 2000. doi:10.1007/978-3-662-04013-3.

[92] F. Pan, B. Zeng, B. Jiang, A. Atrens, H. Dong, Deformation mechanism and microstructure evolution during on-line heating rolling of AZ31B Mg thin sheets, Mater. Charact. 124 (2017) 266–275. doi:10.1016/j.matchar.2017.01.007.

[93] N. Dudova, A. Belyakov, T. Sakai, R. Kaibyshev, Dynamic recrystallization mechanisms operating in a Ni–20%Cr alloy under hot-to-warm working, Acta Mater. 58 (2010) 3624–3632. doi:10.1016/j.actamat.2010.02.032.

[94] M. Shaban, B. Eghbali, Characterization of Austenite Dynamic Recrystallization under Different Z Parameters in a Microalloyed Steel, J. Mater. Sci. Technol. 27 (2011) 359–363. doi:10.1016/S1005-0302(11)60074-1.

[95] H.J. McQueen, Elevated-temperature deformation at forming rates of 10−2 to 102 s−1, Metall. Mater. Trans. A. 33 (2002) 345–362. doi:10.1007/s11661-002-0096-3.

[96] M. Winning, Strain-induced migration of tilt grain boundaries, Scr. Mater. 58 (2008) 85–88. doi:10.1016/j.scriptamat.2007.09.034.

[97] Z. Zeng, Y. Zhang, S. Jonsson, Microstructure and texture evolution of commercial pure titanium deformed at elevated temperatures, Mater. Sci. Eng. A. 513 (2009) 83–90. doi:10.1016/j.msea.2009.01.065.

[98] Y.G. Ko, C.S. Lee, D.H. Shin, S.L. Semiatin, Low-temperature superplasticity of ultra-fine-grained Ti-6Al-4V processed by equal-channel angular pressing, Metall. Mater. Trans. A. 37 (2006) 381–391. doi:10.1007/s11661-006-0008-z.

[99] M.J. Tan, X.J. Zhu, S. Thiruvarudchelvan, K.M. Liew, Superplasticity studies in a beta titanium alloy, (2007).

[100] K.-T. Park, H.-J. Lee, C.S. Lee, B. Du Ahn, H.S. Cho, D.H. Shin, Effect of ECAP Strain on Deformation Behavior at Low Temperature Superplastic Regime of Ultrafine Grained 5083 Al Alloy Fabricated by ECAP, Mater. Trans. 45 (2004) 958–963. https://www.jim.or.jp/journal/e/pdf3/45/03/958.pdf (accessed June 3, 2017).

[101] H. Asgharzadeh, H.S. Kim, A. Simchi, Microstructure, strengthening mechanisms and hot deformation behavior of an oxide-dispersion strengthened UFG Al6063 alloy, Mater. Charact. 75 (2013) 108–114. doi:10.1016/j.matchar.2012.10.007.

[102] G. Khalaj, M.J. Khalaj, A. Nazari, Microstructure and hot deformation behavior of AlMg6 alloy produced by equal-channel angular pressing, Mater. Sci. Eng. A. 542 (2012) 15–20. doi:10.1016/j.msea.2012.02.015.

[103] J. Feng, H.F. Sun, J.C. Li, X.W. Li, J. Zhang, W. Fang, W.B. Fang, Tensile flow and work hardening behaviors of ultrafine-grained Mg-3Al-Zn alloy at elevated temperatures, Mater. Sci. Eng. A. 667 (2016) 97–105. doi:10.1016/j.msea.2016.05.005.

[104] M.D. Callaghan, S.R. Humphries, M. Law, M. Ho, P. Bendeich, H. Li, W.Y. Yeung, Energy-based approach for the evaluation of low cycle fatigue behaviour of 2.25Cr–1Mo steel at elevated temperature, Mater. Sci. Eng. A. 527 (2010) 5619–5623. doi:10.1016/j.msea.2010.05.011.

[105] T. Niendorf, H.J. Maier, D. Canadinc, I. Karaman, Cyclic stability of ultrafine-grained interstitial-free steel at elevated temperatures, Mater. Sci. Eng. A. 503 (2009) 160–162. doi:10.1016/j.msea.2008.03.054.

[106] D. Canadinc, H.J. Maier, P. Gabor, J. May, On the cyclic deformation response of ultrafine-grained Al–Mg alloys at elevated temperatures, Mater. Sci. Eng. A. 496 (2008) 114–120. doi:10.1016/j.msea.2008.04.071.

[107] F. Rubitschek, T. Niendorf, I. Karaman, H.J. Maier, Microstructural stability of ultrafine-grained niobium–zirconium alloy at elevated temperatures, J. Alloys Compd. 517 (2012) 61–68. doi:10.1016/j.jallcom.2011.11.150.

[108] V.M. Segal, Engineering and commercialization of equal channel angular extrusion (ECAE), Mater. Sci. Eng. A. 386 (2004) 269–276. doi:10.1016/j.msea.2004.07.023.

[109] J.J. Jonas, R.A. Holt, C.E. Coleman, Plastic stability in tension and compression, Acta Metall. 24 (1976) 911–918. doi:10.1016/0001-6160(76)90039-0.

[110] I.A. Maksoud, H. Ahmed, J. Rödel, Investigation of the effect of strain rate and temperature on the deformability and microstructure evolution of AZ31 magnesium alloy, Mater. Sci. Eng. A. 504 (2009) 40–48. doi:10.1016/j.msea.2008.10.033.

[111] S. V. Sajadifar, M. Ketabchi, M. Nourani, Modeling of mechanical characteristics in hot deformation of 4130 steel, Steel Res. Int. 82 (2011) 934–939. doi:10.1002/srin.201100024.

[112] Y.Y. Zong, D.B. Shan, M. Xu, Y. Lv, Flow softening and microstructural evolution of TC11 titanium alloy during hot deformation, J. Mater. Process. Technol. 209 (2009) 1988–1994. doi:10.1016/j.jmatprotec.2008.04.063.

[113] Y. Estrin, H. Mecking, A unified phenomenological description of work hardening and creep based on one-parameter models, Acta Metall. 32 (1984) 57–70. doi:10.1016/0001-6160(84)90202-5.

[114] T. Furuhara, B. Poorganji, H. Abe, T. Maki, Dynamic recovery and recrystallization in titanium alloys by hot deformation, JOM. 59 (2007) 64–67. doi:10.1007/s11837-007-0013-8.

[115] Y.V.R.K. Prasad, N. Ravichandran, Effect of stacking fault energy on the dynamic recrystallization during hot working of FCC metals: A study using processing maps, Bull. Mater. Sci. 14 (1991) 1241–1248. doi:10.1007/BF02744618.

[116] P. Kwasniak, M. Muzyk, H. Garbacz, K.J. Kurzydlowski, Influence of C, H, N, and O

interstitial atoms on deformation mechanism in titanium—First principles calculations of generalized stacking fault energy, 2013. doi:10.1016/j.matlet.2012.12.002.

[117] T. Sakai, J.J. Jonas, Overview no. 35 Dynamic recrystallization: Mechanical and microstructural considerations, Acta Metall. 32 (1984) 189–209. doi:10.1016/0001-6160(84)90049-X.

[118] T. Sakai, Dynamic recrystallization microstructures under hot working conditions, J. Mater. Process. Technol. 53 (1995) 349–361. doi:10.1016/0924-0136(95)01992-N.

[119] M. Nourani, S. V. Sajadifar, M. Ketabchi, A.S. Milani, S. Yannacopoulos, On the microstructural evolution of 4130 steel during hot compression, Recent Patents Mater. Sci. 5 (2012) 74–83.

[120] S. Suwas, B. Beausir, L.S. Tóth, J.-J. Fundenberger, G. Gottstein, Texture evolution in commercially pure titanium after warm equal channel angular extrusion, Acta Mater. 59 (2011) 1121–1133. doi:10.1016/j.actamat.2010.10.045.

[121] H. Asgharzadeh, A. Simchi, Hot Deformation Behavior of P/M Al6061-20% SiC Composite, Mater. Sci. Forum. 534–536 (2007) 897–900. doi:10.4028/www.scientific.net/MSF.534-536.897.

[122] R.S. Mishra, V.V. Stolyarov, C. Echer, R.Z. Valiev, A.K. Mukherjee, Mechanical behavior and superplasticity of a severe plastic deformation processed nanocrystalline Ti–6Al–4V alloy, Mater. Sci. Eng. A. 298 (2001) 44–50. doi:10.1016/S0921-5093(00)01338-1.

[123] J.J. Jonas, F. Montheillet, Temperature Dependence of the Rate Sensitivity and Its

Effect on the Activation Energy for High-Temperature Flow, Met. Mater. Trans. A. 27 (1996) 3343–46.

[124] B. Paul, A. Sarkar, J.K. Chakravartty, A. Verma, R. Kapoor, A.C. Bidaye, I.G. Sharma, A.K. Suri, Dynamic Recrystallization in Sintered Cobalt during High-Temperature Deformation, Metall. Mater. Trans. A. 41 (2010) 1474–1482. doi:10.1007/s11661-010-0181-y.

[125] S.L. Semiatin, G.D. Lahoti, Deformation and unstable flow in hot forging of Ti-6Ai-2Sn-4Zr-2Mo-0.1Si, Metall. Trans. A. 12 (1981) 1705–1717. doi:10.1007/BF02643753.

[126] A.R. Salehi, S. Serajzadeh, N. Yazdipour, A study on flow behavior of A-286 superalloy during hot deformation, Mater. Chem. Phys. 101 (2007) 153–157. doi:10.1016/j.matchemphys.2006.03.012.

[127] M. Belbasi, M.T. Salehi, S.A.A.A. Mousavi, S.M. Ebrahimi, A study on the mechanical behavior and microstructure of NiTiHf shape memory alloy under hot deformation, Mater. Sci. Eng. A. 560 (2013) 96–102. doi:10.1016/j.msea.2012.09.039.

[128] F.J. Humphreys, M. Hatherly, F.J. Humphreys, M. Hatherly, Chapter 13 – Hot Deformation and Dynamic Restoration, in: Recryst. Relat. Annealing Phenom., 2004: p. 415–V. doi:10.1016/B978-008044164-1/50017-7.

[129] C.M. Sellars, G.J. Davies, Sheffield Metallurgical and Engineering Association., University of Sheffield. Department of Metallurgy., Metals Society., Hot working and forming processes : proceedings of an International Conference on Hot Working and Forming Processes, The Society, 1980.

[130] C.M. Sellars, The kinetics of softening processes during hot working of austenite, Czechoslov. J. Phys. 35 (1985) 239–248. doi:10.1007/BF01605090.

[131] S. V. Sajadifar, G.G. Yapici, M. Ketabchi, B. Bemanizadeh, High temperature deformation behavior of 4340 steel: Activation energy calculation and modeling of flow response, J. Iron Steel Res. Int. 20 (2013) 133–139. doi:10.1016/S1006-706X(13)60226-5.

[132] N.G. Jones, R.J. Dashwood, D. Dye, M. Jackson, Thermomechanical processing of Ti–5Al–5Mo–5V–3Cr, Mater. Sci. Eng. A. 490 (2008) 369–377. doi:10.1016/j.msea.2008.01.055.

[133] J. Zhang, H. Di, H. Wang, K. Mao, T. Ma, Y. Cao, Hot deformation behavior of Ti-15-3 titanium alloy: A study using processing maps, activation energy map, and Zener-Hollomon parameter map, J. Mater. Sci. 47 (2012) 4000–4011. doi:10.1007/s10853-012-6253-1.

[134] D.G. Robertson, H.B. McShane, Analysis of high temperature flow stress of titanium alloys IMI 550 and Ti-10V-2Fe-3Al during isothermal forging, Mater. Sci. Technol. 14 (1998) 339–345. doi:10.1179/mst.1998.14.4.339.

[135] A. Laasraoui, J.J. Jonas, Prediction of steel flow stresses at high temperatures and strain rates, Metall. Trans. A. 22 (1991) 1545–1558. doi:10.1007/BF02667368.

[136] H. Asgharzadeh, A. Simchi, H.S. Kim, High-temperature deformation and structural restoration of a nanostructured Al alloy, Scr. Mater. 66 (2012) 911–914. doi:10.1016/j.scriptamat.2012.02.026.

[137] Y.C. Lin, M.-S. Chen, J. Zhong, Prediction of 42CrMo steel flow stress at high

temperature and strain rate, Mech. Res. Commun. 35 (2008) 142–150. doi:10.1016/j.mechrescom.2007.10.002.

[138] R.E. Smallman, R.J. (Ray J.. Bishop, Modern physical metallurgy and materials engineering : science, process, applications., Butterworth Heinemann, 1999.

[139] C.M. Sellars, W.J. McTegart, On the mechanism of hot deformation, Acta Metall. 14 (1966) 1136–1138. doi:10.1016/0001-6160(66)90207-0.

[140] M. El Wahabi, J.M. Cabrera, J.M. Prado, Hot working of two AISI 304 steels: a comparative study, Mater. Sci. Eng. A. 343 (2003) 116–125. doi:10.1016/S0921-5093(02)00357-X.

[141] H.K.D.H. (Harshad K.D.H. Bhadeshia, R.W.K. (Robert W.K. Honeycombe, Steels : microstructure and properties, Elsevier, Butterworth-Heinemann, 2006.

[142] L.. Kong, P.. Hodgson, B. Wang, Development of constitutive models for metal forming with cyclic strain softening, J. Mater. Process. Technol. 89 (1999) 44–50. doi:10.1016/S0924-0136(99)00015-1.

[143] S. V. Sajadifar, G.G. Yapici, Hot Deformation Behavior of Ultra-Fine Grained Pure Ti, Adv. Mater. Res. 829 (2013) 10–14. doi:10.4028/www.scientific.net/AMR.829.10.

[144] J.J. Jonas, X. Quelennec, L. Jiang, É. Martin, The Avrami kinetics of dynamic recrystallization, Acta Mater. 57 (2009) 2748–2756. doi:10.1016/j.actamat.2009.02.033.

[145] F.J. Humphreys, M. Hatherly, Recrystallization and related annealing phenomena, Elsevier, 2004.

[146] G.R. Johnson, W.H. Cook, A constitutive model and data for metals subjected to large strains, in: Proc. 7th Int. Symp. Ballist., The Netherlands, 1983: pp. 541–547.

[147] Y.C. Lin, Q.-F. Li, Y.-C. Xia, L.-T. Li, A phenomenological constitutive model for high temperature flow stress prediction of Al–Cu–Mg alloy, Mater. Sci. Eng. A. 534 (2012) 654–662. doi:http://dx.doi.org/10.1016/j.msea.2011.12.023.

[148] S. V. Sajadifar, G.G. Yapici, High Temperature Flow Response Modeling of Ultra-Fine Grained Titanium, Metals (Basel). 5 (2015) 1315–1327. doi:10.3390/met5031315.

[149] M. Hoseini, M. Hamid Pourian, F. Bridier, H. Vali, J.A. Szpunar, P. Bocher, Thermal stability and annealing behaviour of ultrafine grained commercially pure titanium, Mater. Sci. Eng. A. 532 (2012) 58–63. doi:10.1016/j.msea.2011.10.062.

[150] É. Martin, J.J. Jonas, Evolution of microstructure and microtexture during the hot deformation of Mg–3% Al, Acta Mater. 58 (2010) 4253–4266. doi:10.1016/j.actamat.2010.04.017.

[151] S. V. Sajadifar, G.G. Yapici, Elevated temperature mechanical behavior of severely deformed titanium, J. Mater. Eng. Perform. 23 (2014) 1834–1844. doi:10.1007/s11665-014-0947-2.

[152] R.D. Doherty, D.A. Hughes, F.J. Humphreys, J.J. Jonas, D. Juul Jensen, M.E. Kassner, W.E. King, T.R. McNelley, H.J. McQueen, A.D. Rollett, Current issues in recrystallization: A review, Mater. Today. 1 (1998) 14–15. doi:10.1016/S1369-7021(98)80046-1.

[153] S. V. Sajadifar, G.G. Yapici, Effect of Purity Levels on the High-Temperature

Deformation Characteristics of Severely Deformed Titanium, Metall. Mater. Trans. A. (2017) 1–14. doi:10.1007/s11661-016-3929-1.

[154] S. V. Sajadifar, G.G. Yapici, Workability characteristics and mechanical behavior modeling of severely deformed pure titanium at high temperatures, Mater. Des. 53 (2014) 749–757. doi:10.1016/j.matdes.2013.07.057.

[155] J. Gubicza, N.H. Nam, L. Balogh, R.J. Hellmig, V.V. Stolyarov, Y. Estrin, T. Ungár, Microstructure of severely deformed metals determined by X-ray peak profile analysis, J. Alloys Compd. 378 (2004) 248–252. doi:10.1016/j.jallcom.2003.11.162.

[156] G. Purcek, G.G. Yapici, I. Karaman, H.J. Maier, Effect of commercial purity levels on the mechanical properties of ultrafine-grained titanium, Mater. Sci. Eng. A. 528 (2011) 2303–2308. doi:10.1016/j.msea.2010.11.021.

[157] A. V. Podolskiy, H.P. Ng, I.A. Psaruk, E.D. Tabachnikova, R. Lapovok, Cryogenic equal channel angular pressing of commercially pure titanium: microstructure and properties, J. Mater. Sci. 49 (2014) 6803–6812. doi:10.1007/s10853-014-8382-1.

[158] O. Sitdikov, E. Avtokratova, T. Sakai, K. Tsuzaki, R. Kaibyshev, Y. Watanabe, Effect of Processing Temperature on Microstructure Development during ECAP of Al-Mg-Sc Alloy, Mater. Sci. Forum. 584–586 (2008) 481–486. doi:10.4028/www.scientific.net/MSF.584-586.481.

[159] E.J. Kwak, C.H. Bok, M.H. Seo, T.-S. Kim, H.S. Kim, Processing and Mechanical Properties of Fine Grained Magnesium by Equal Channel Angular Pressing, Mater. Trans. 49 (2008) 1006–1010. doi:10.2320/matertrans.MC200725.

[160] F.J. Gil, C. Aparicio, J.A. Planell, Effect of Oxygen Content on Grain Growth Kinetics

of Titanium, J. Mater. Synth. Process. 10 (2002) 263–266. doi:10.1023/A:1023094126132.

[161] A. Khamei, K. Dehghani, Microstructural Evolution During the Hot Deformation of Ti-55Ni (at. pct) Intermetallic Alloy, Metall. Mater. Trans. A. 41 (2010) 2595–2605. doi:10.1007/s11661-010-0338-8.

[162] X.J. Zhu, M.J. Tan, W. Zhou, Enhanced superplasticity in commercially pure titanium alloy, Scr. Mater. 52 (2005) 651–655. doi:10.1016/j.scriptamat.2004.11.017.

[163] X.-M. Chen, Y.C. Lin, M.-S. Chen, H.-B. Li, D.-X. Wen, J.-L. Zhang, M. He, Microstructural evolution of a nickel-based superalloy during hot deformation, Mater. Des. 77 (2015) 41–49. doi:10.1016/j.matdes.2015.04.004.

[164] Y.C. Lin, X.-Y. Wu, X.-M. Chen, J. Chen, D.-X. Wen, J.-L. Zhang, L.-T. Li, EBSD study of a hot deformed nickel-based superalloy, J. Alloys Compd. 640 (2015) 101–113. doi:10.1016/j.jallcom.2015.04.008.

[165] M. Winning, D. Raabe, in Ceramic Transactions, 15th International Conference on Textures of Materials, in: Pittsburgh, 2008.

[166] I. Sabirov, M.R. Barnett, Y. Estrin, P.D. Hodgson, The effect of strain rate on the deformation mechanisms and the strain rate sensitivity of an ultra-fine-grained Al alloy, Scr. Mater. 61 (2009) 181–184. doi:10.1016/j.scriptamat.2009.03.032.

[167] K. Shojaei, S. V. Sajadifar, G.G. Yapici, On the mechanical behavior of cold deformed aluminum 7075 alloy at elevated temperatures, Mater. Sci. Eng. A. 670 (2016) 81–89. doi:10.1016/j.msea.2016.05.113.

[168] I.P. Semenova, A.I. Korshunov, G.K. Salimgareeva, V. V. Latysh, E.B. Yakushina, R.Z.

Valiev, Mechanical behavior of ultrafine-grained titanium rods obtained using severe plastic deformation, Phys. Met. Metallogr. 106 (2008) 211–218. doi:10.1134/S0031918X08080140.

[169] Y. Nan, Y. Ning, H. Liang, H. Guo, Z. Yao, M.W. Fu, Work-hardening effect and strain-rate sensitivity behavior during hot deformation of Ti–5Al–5Mo–5V–1Cr–1Fe alloy, Mater. Des. 82 (2015) 84–90. doi:10.1016/j.matdes.2015.05.060.

[170] S. Zhang, Y.C. Wang, A.P. Zhilyaev, D. V. Gunderov, S. Li, G.I. Raab, E. Korznikova, T.G. Langdon, Effect of temperature on microstructural stabilization and mechanical properties in the dynamic testing of nanocrystalline pure Ti, Mater. Sci. Eng. A. 634 (2015) 64–70. doi:10.1016/j.msea.2015.03.032.

[171] M. Zhou, Y.C. Lin, J. Deng, Y.-Q. Jiang, Hot tensile deformation behaviors and constitutive model of an Al–Zn–Mg–Cu alloy, Mater. Des. 59 (2014) 141–150. doi:10.1016/j.matdes.2014.02.052.

[172] A.A. Khamei, K. Dehghani, R. Mahmudi, Modeling the Hot Ductility of AA6061 Aluminum Alloy After Severe Plastic Deformation, JOM. 67 (2015) 966–972. doi:10.1007/s11837-015-1354-3.

[173] L. Li, W. Wei, Y. Lin, C. Lijia, L. Zheng, Grain boundary sliding and accommodation mechanisms during superplastic deformation of ZK40 alloy processed by ECAP, J. Mater. Sci. 41 (2006) 409–415. doi:10.1007/s10853-005-2163-9.

[174] J. Li, B. Jiang, C. Zhang, L. Zhou, Y. Liu, Hot embrittlement and effect of grain size on hot ductility of martensitic heat-resistant steels, Mater. Sci. Eng. A. 677 (2016) 274–280. doi:10.1016/j.msea.2016.09.072.

[175] F.-W. Long, Q.-W. Jiang, L. Xiao, X.-W. Li, Compressive Deformation Behaviors of Coarse- and Ultrafine-Grained Pure Titanium at Different Temperatures: A Comparative Study, Mater. Trans. 52 (2011) 1617–1622. doi:10.2320/matertrans.M2011041.

[176] J. Deng, Y.C. Lin, S.-S. Li, J. Chen, Y. Ding, Hot tensile deformation and fracture behaviors of AZ31 magnesium alloy, Mater. Des. 49 (2013) 209–219. doi:10.1016/j.matdes.2013.01.023.

[177] M. Greger, M. Widomska, L. Kander, Mechanical properties of ultra-fine grain titanium, J. Achiev. Mater. Manuf. Eng. Vol. 40 (2010) 33–40.

[178] K. Madou, J.-B. Leblond, L. Morin, Numerical studies of porous ductile materials containing arbitrary ellipsoidal voids – II: Evolution of the length and orientation of the void axes, Eur. J. Mech. - A/Solids. 42 (2013) 490–507. doi:10.1016/j.euromechsol.2013.06.005.

[179] L. Morin, J.-B. Leblond, A.A. Benzerga, Coalescence of voids by internal necking: Theoretical estimates and numerical results, J. Mech. Phys. Solids. 75 (2015) 140–158. doi:10.1016/j.jmps.2014.11.009.

[180] O. Renk, P. Ghosh, R. Pippan, Generation of extreme grain aspect ratios in severely deformed tantalum at elevated temperatures, Scr. Mater. 137 (2017) 60–63. doi:10.1016/j.scriptamat.2017.04.024.

[181] V. Maier, A. Leitner, R. Pippan, D. Kiener, Thermally Activated Deformation Behavior of ufg-Au: Environmental Issues During Long-Term and High-Temperature Nanoindentation Testing, JOM. 67 (2015) 2934–2944. doi:10.1007/s11837-015-

1638-7.

[182] T. Suo, Y. Li, K. Xie, F. Zhao, K.-S. Zhang, Q. Deng, Experimental investigation on strain rate sensitivity of ultra-fine grained copper at elevated temperatures, Mech. Mater. 43 (2011) 111–118. doi:10.1016/j.mechmat.2011.02.002.

[183] D.G. Tari, M.J. Worswick, Elevated temperature constitutive behavior and simulation of warm forming of AZ31B, J. Mater. Process. Technol. 221 (2015) 40–55. doi:10.1016/j.jmatprotec.2014.12.014.

[184] G.G. Yapici, I. Karaman, H.J. Maier, Y.I. Chumlyakov, Microstructural refinement and deformation twinning during severe plastic deformation of 316L stainless steel at high temperatures, J. Mater. Res. 19 (2004) 2268–2278. doi:https://doi.org/10.1557/JMR.2004.0289.

[185] Q. Li, Q. Yu, J. Zhang, Y. Jiang, Effect of strain amplitude on tension–compression fatigue behavior of extruded Mg6Al1ZnA magnesium alloy, Scr. Mater. 62 (2010) 778–781. doi:10.1016/j.scriptamat.2010.01.052.

[186] A. Kumar, N. Singh, V. Singh, Influence of stabilization treatment on low cycle fatigue behavior of Ti alloy IMI 834, Mater. Charact. 51 (2003) 225–233. doi:10.1016/j.matchar.2003.11.004.

[187] H.-G. Lambers, C.J. Rüsing, T. Niendorf, D. Geissler, J. Freudenberger, H.J. Maier, On the low-cycle fatigue response of pre-strained austenitic Fe61Mn24Ni6.5Cr8.5 alloy showing TWIP effect, Int. J. Fatigue. 40 (2012) 51–60. doi:10.1016/j.ijfatigue.2012.01.002.

[188] T. Niendorf, D. Canadinc, H.J. Maier, I. Karaman, The role of heat treatment on the

cyclic stress–strain response of ultrafine-grained interstitial-free steel, Int. J. Fatigue. 30 (2008) 426–436. doi:10.1016/j.ijfatigue.2007.04.015.

[189] H. Mughrabi, H.W. Höppel, M. Kautz, R.Z. Valiev, Annealing treatments to enhance thermal and mechanical stability of ultrafine-grained metals produced by severe plastic deformation, Zeitschrift Für Met. 94 (2003) 1079–1083. doi:10.3139/146.031079.

[190] T. Niendorf, C. Lotze, D. Canadinc, A. Frehn, H.J. Maier, The role of monotonic pre-deformation on the fatigue performance of a high-manganese austenitic TWIP steel, Mater. Sci. Eng. A. 499 (2009) 518–524. doi:10.1016/j.msea.2008.09.033.

[191] T. Niendorf, D. Canadinc, H.J. Maier, I. Karaman, On the Microstructural Stability of Ultrafine-Grained Interstitial-Free Steel under Cyclic Loading, Metall. Mater. Trans. A. 38 (2007) 1946–1955. doi:10.1007/s11661-007-9154-1.

[192] T. Niendorf, D. Canadinc, H.J. Maier, I. Karaman, S.G. Sutter, On the fatigue behavior of ultrafine-grained interstitial-free steel, Int. J. Mater. Res. 97 (2006) 1328–1336. doi:10.3139/146.101377.

[193] H. Mughrabi, H.W. Höppel, Cyclic Deformation and Fatigue Properties of Ultrafine Grain Size Materials: Current Status and Some Criteria for Improvement of the Fatigue Resistance, MRS Proc. 634 (2000) B2.1.1. doi:10.1557/PROC-634-B2.1.1.

[194] S.J. Li, T.C. Cui, Y.L. Hao, R. Yang, Fatigue properties of a metastable β-type titanium alloy with reversible phase transformation, Acta Biomater. 4 (2008) 305–317. doi:10.1016/j.actbio.2007.09.009.

[195] Y.-H. Lin, K.-H. Hu, F.-H. Kao, S.-H. Wang, J.-R. Yang, C.-K. Lin, Dynamic strain aging

in low cycle fatigue of duplex titanium alloys, Mater. Sci. Eng. A. 528 (2011) 4381–4389. doi:10.1016/j.msea.2011.02.013.

[196] W. Blum, Y.J. Li, K. Durst, Stability of ultrafine-grained Cu to subgrain coarsening and recrystallization in annealing and deformation at elevated temperatures, Acta Mater. 57 (2009) 5207–5217. doi:10.1016/j.actamat.2009.07.030.

[197] S.Q. Wang, J.H. Liu, D.L. Chen, Strain-controlled fatigue properties of dissimilar welded joints between Ti–6Al–4V and Ti17 alloys, Mater. Des. 49 (2013) 716–727. doi:10.1016/j.matdes.2013.02.034.

[198] B. Mirzakhani, M.T. Salehi, S. Khoddam, S.H. Seyedein, M.R. Aboutalebi, Investigation of Dynamic and Static Recrystallization Behavior During Thermomechanical Processing in a API-X70 Microalloyed Steel, J. Mater. Eng. Perform. 18 (2009) 1029–1034. doi:10.1007/s11665-008-9338-x.

[199] I. Semenova, G. Salimgareeva, G. Da Costa, W. Lefebvre, R. Valiev, Enhanced Strength and Ductility of Ultrafine-Grained Ti Processed by Severe Plastic Deformation, Adv. Eng. Mater. 12 (2010) 803–807. doi:10.1002/adem.201000059.

[200] H. SONG, Z. WANG, Effect of electropulsing on dislocation mobility of titanium sheet, Trans. Nonferrous Met. Soc. China. 22 (2012) 1599–1605. doi:10.1016/S1003-6326(11)61362-9.

[201] A.R. Anilchandra, M.K. Surappa, Microstructure and damping behaviour of consolidated magnesium chips, Mater. Sci. Eng. A. 542 (2012) 94–103. doi:10.1016/j.msea.2012.02.038.

[202] S.G. Ma, P.K. Liaw, M.C. Gao, J.W. Qiao, Z.H. Wang, Y. Zhang, Damping behavior of

AlxCoCrFeNi high-entropy alloys by a dynamic mechanical analyzer, J. Alloys Compd. 604 (2014) 331–339. doi:10.1016/j.jallcom.2014.03.050.

[203] P.C. Millett, T. Desai, V. Yamakov, D. Wolf, Atomistic simulations of diffusional creep in a nanocrystalline body-centered cubic material, Acta Mater. 56 (2008) 3688–3698. doi:10.1016/j.actamat.2008.04.004.

[204] S.V. Sajadifar, G.G. Yapici, Effect of Purity Levels on the High-Temperature Deformation Characteristics of Severely Deformed Titanium, Metall. Mater. Trans. A. 48 (2017) 999–1012. doi:10.1007/s11661-016-3929-1.

VITA

Seyedvahid Sajjadifar was born in Tehran, Iran in 1985. In July 2007, he received his B.Sc. degree in Metallurgical and Materials Engineering from Islamic Azad University, Saveh, Iran. In January 2010, he completed his M.S. studies while publishing six peer-reviewed journal articles. In September 2012, he started working towards his Ph.D. He received his Ph.D. in May 2017 after publishing eight peer-reviewed journal articles (3 in preparation). These publications can be seen as follows:

1. S.V. Sajadifar, P. Krooß, T. Wegener, E. Demler, T. Niendorf, H.J. Maier, G.G. Yapici, “Cyclic Deformation Response of Ultrafine-grained Ti at Elevated Temperatures”, In preparation.
2. S.V. Sajadifar, K.C. Atli, G.G. Yapici, “Effect of Severe Plastic Deformation on the Damping Properties of CP Titanium”, In preparation.
3. S.V. Sajadifar, H.J. Maier, G.G. Yapici, “Warm Tensile Deformation and Fracture Behavior of Ultrafine-Grained Titanium”, In preparation.
4. S.V. Sajadifar, G.G. Yapici, “Effect of Purity Levels on the High Temperature Deformation Characteristics of Severely Deformed Titanium”, Metallurgical and Materials Transactions A, 2017, 48, 999-1012.
5. S.V. Sajadifar, G.G. Yapici, “High Temperature Flow Response Modeling of Ultra-fine Grained Titanium” Metals, 2015, 5, 1315-1327.
6. S.V. Sajadifar, G.G. Yapici, “Elevated Temperature Mechanical Behavior of Severely Deformed Titanium” Journal of Materials Engineering and Performance, 2014, 23, 1834-1844.
7. S.V. Sajadifar, G.G. Yapici, “Workability characteristics and mechanical behavior modeling of severely deformed pure titanium at high temperatures”, Materials and Design, 2014, 53, 749-757.
8. S.V. Sajadifar, G.G. Yapici, “Hot Deformation Behavior of Ultra-Fine Grained Pure Ti” Advanced Materials Research, 2014, 829, 10-14.